FLUX PINNING
IN
TYPE-II SUPERCONDUCTORS

C. A. M. VAN DER KLEIN

FLUX PINNING
IN
TYPE-II SUPERCONDUCTORS

PROEFSCHRIFT

TER VERKRIJGING VAN DE GRAAD VAN DOCTOR IN DE WISKUNDE EN NATUURWETENSCHAPPEN AAN DE RIJKSUNIVERSITEIT TE LEIDEN, OP GEZAG VAN DE RECTOR MAGNIFICUS DR. A.E. COHEN, HOOGLERAAR IN DE FACULTEIT DER LETTEREN, VOLGENS BESLUIT VAN HET COLLEGE VAN DEKANEN TE VERDEDIGEN OP DINSDAG 11 JUNI 1974 TE KLOKKE 15.15 UUR

door

CORNELIS ANTOON MARIA VAN DER KLEIN
geboren te Rotterdam in 1946

Krips Repro - Meppel

PROMOTOR: DR. D. DE KLERK

Ter herinnering aan mijn vader

Aan mijn moeder
Aan Erna

S T E L L I N G E N

1. De vraag of het permeabiliteitsgedrag van een type-II supergeleider met een model voor de kritische toestand kan worden beschreven, is direkt te beantwoorden aan de hand van een diagram van μ'' tegen μ'.
Het gedrag van de verliezen als funktie van de amplitude van het wisselveld geeft hierover geen uitsluitsel.

   S.L. Wipf, Proceedings 1968 Summer Study en Superconducting Devices and Accelerators; Brookhaven National Laboratory Report 50155 (c - 55), 1968.

   Dit proefschrift, hoofdstukken 5 en 6.

2. De onomkeerbaarheid van de magnetisatiekromme, zoals Brown, Blewitt en Scott en ook Kernohan en Sekula die hebben gemeten, wordt zowel veroorzaakt door een oppervlaktebarrière als door fluxverankering in het kristalrooster. Hun experimenten geven dan ook geen goed beeld van het effekt van roosterdefekten, veroorzaakt door neutronen bestraling, op de magnetische eigenschappen van supergeleidend niobium.

   B.S. Brown, T.H. Blewitt en T. Scott, Phys.Stat.Sol.(a) 16, 105 (1973).

   R.H. Kernohan en S.T. Sekula, J. of appl. Phys. 38, 4904 (1967).

3. Voor het interpreteren van de kritische-stroommetingen aan type-II supergeleiders zijn gegevens over het magnetisch gedrag onmisbaar.

4. Teneinde een beter inzicht te krijgen in de fluxverankering door puntdefekten, zouden metingen moeten worden uitgevoerd aan type-II supergeleiders die bij zodanig hoge temperatuur met neutronen zijn bestraald, dat "voids" in het kristalrooster zijn gevormd.

5. De metingen van Dubeck en Setty aan NbTi zijn niet representatief voor het warmtegeleidingsgedrag van het materiaal dat veelvuldig wordt toegepast voor het konstrueren van supergeleidende spoelen. De konklusie die men uit hun resultaten zou kunnen trekken, dat dit materiaal niet geschikt is als thermisch isolator met elektrische weerstand nul, is onjuist.

   L. Dubeck en K.S.L. Setty, Phys. Letters 27A, 334 (1968).

6. De bewering van Marchand en Stapleton, dat voor de beschrijving van de spin-rooster relaxatietijden van neodyniumionen in yttriumethylsulfaat een H^2T^7-Raman proces in rekening moet worden genomen, wordt onvoldoende door hun experimentele gegevens bevestigd, en is in strijd met de resultaten van Van den Broek en Van der Marel.

   R.L. Marchand en H.J. Stapleton, Phys. Rev. B9, 14 (1974).

   J. van den Broek en L.C. van der Marel, Physica 29 948 (1963).

7. Uit oogpunt van de met rotatiekoeling te bereiken protonpolarisatie biedt het gebruik van ytterbiumionen in yttriumhydroxyde geen voordelen boven het tot nu toe gebruikelijke systeem van ytterbiumionen in yttriumethylsulfaat.

   R.L. Lichti en H.J. Stapleton, Phys. Rev. B8, 4134 (1973).

   K.H. Langly en C.D. Jeffries, Phys. Rev. 152, 358 (1966).

8. De voordelen van het gebruik van de ^3He smeltkurve als primaire thermometer in het temperatuurgebied tussen 20 en 2 mK zijn door Scribner en Adams overschat.

   R.A. Scribner en E.D. Adams, Temperature 4, 37 (1971).

9. Het biedt grote voordelen de supergeleidende magneten die in een fusie-reactor nodig zijn voor het toroidale veld en voor de zogenaamde axiaal-symmetrische "divertor", te konstrueren met holle geleiders, waardoor boven-kritische helium stroomt. Men dient hiermee bij ontwerpstudies ernstig rekening te houden.

10. De gemiddelde promotieduur kan worden verkort door het "promoveren op artikelen" sterker te stimuleren.

11. Het inleveren van niet-gebruikte medicijnen bij een speciale, met vernietiging van schadelijke stoffen belaste, instantie dient van overheidswege te worden georganiseerd en gestimuleerd.

12. Gezien het bedrag dat bij afkoop van levensverzekeringen wordt gerestitueerd, is men licht geneigd te concluderen, dat verzekeringsmaatschappijen slechte beleggers zijn.

C.A.M. van der Klein 11 juni 1974

CONTENTS

LIST OF SYMBOLS 7

CHAPTER 1 GENERAL INTRODUCTION 11

CHAPTER 2 THE EFFECT OF COLD ROLLING AND HEAT TREATMENT ON THE MAGNETIC BEHAVIOUR IN STATIONARY AND ALTERNATING FIELDS

2.1 Introduction 16
2.2 Experimental details 17
2.3 The magnetization curves 22
2.4 The susceptibility measurements 27
2.5 The resistive transitions 35
2.6 Discussion 37
References 41

CHAPTER 3 THE EFFECT OF NEUTRON IRRADIATION DAMAGE ON THE MAGNETIC BEHAVIOUR IN STATIONARY FIELDS

3.1 Introduction 43
3.2 The samples 43
3.3 The experimental results 46
3.3.1 The unirradiated samples 46
3.3.2 The irradiated samples 49
3.4 Discussion 55
3.4.1 The unirradiated samples 55
3.4.2 The irradiated samples 58
References 68

CHAPTER 4 THE PEAK-EFFECT DUE TO IRRADIATION DAMAGE

4.1 Introduction 69
4.2 Experimental results 69
4.3 Discussion 74
References 80

CHAPTER 5 CALCULATIONS ON THE PERMEABILITY BASED ON THE LONDON-BEAN MODEL

5.1 Introduction 81

5.2 The theoretical models 82

5.2.1 The influence of surface screening above H_{c_2} 82

5.2.2 The London-Bean model in the region below H_{c_2} 84

5.2.3 The extension of the London-Bean model with an irreversible surface jump 87

5.2.4 The extension of the London-Bean model with a surface layer without pinning 89

5.3 Derivation of the formulae 91

5.3.1 Introduction 91

5.3.2 The influence of surface screening on the permeability 92

5.3.3 The London-Bean model 97

5.3.4 The London-Bean model with an irreversible surface jump 102

5.3.5 The London-Bean model extended with a surface layer without pinning 108

5.4 Discussion of the models 112

5.4.1 The permeability diagram 112

5.4.2 The results obtained with the sample P1600. 116

5.4.3 Other models 118

References 120

CHAPTER 6 THE EFFECT OF NEUTRON IRRADIATION DAMAGE ON THE MAGNETIC BEHAVIOUR IN ALTERNATING FIELDS

6.1 Introduction 122

6.2 Theoretical considerations 122

6.3 Experimental details 133

6.4 The experimental results 135

6.5 Discussion 143

References 150

SAMENVATTING 151

ZUSAMMENFASSUNG 153

STUDIEOVERZICHT 156

LIST OF SYMBOLS

a_0	:	flux lattice spacing (= 1.07 $(\phi_0/B)^{\frac{1}{2}}$)
B	:	local magnetic induction
$\overline{B}$	:	average magnetic induction in the sample
B_s	:	magnetic induction at the surface of the sample
B_p	:	maximum average induction due to the peak effect
ΔB	:	extra induction due to the peak effect
ΔB_s	:	extra induction due to the surface pinning
b	:	reduced magnetic induction (= B/H_{c2})
b_p	:	B_p/H_{c2}
C_{ii}	:	elastic moduli of the flux lattice
d	:	half-thickness of the samples
F_d	:	driving force
$F(B)$	:	a dimensionless function, determined by a flux distribution model
$f(b)$	:	the same, but using reduced quantities
H	:	magnetic field strength
H_a	:	value of the applied field
H_a^*	:	applied field at which the induction reaches the axis of the sample
H_A	:	Abrikosov field, in reversible equilibrium with the local induction inside the sample
H_{c1}	:	lower critical field
H_{c2}	:	upper critical field
H_{c3}	:	surface critical field
H_n	:	field of first nucleation
H_c	:	thermodynamic critical field
H_0	:	amplitude of the alternating field
H_p	:	magnetic field at which the peak effect is at its maximum value
ΔH	:	surface barrier

$\Delta' H_{c2}$: shift of the upper critical field due to neutron irradiation

h : $(H - H_{c1})/H_{c2}$

h_a : $(H_a - H_{c1})/H_{c2}$

h_0 : H_0/H_{c2}

h_1 : H_{c1}/H_{c2}

h_2 : $(H_{c2} - H_{c1})/H_{c2}$

J_c : critical current

J_{c_s} : surface contribution to the critical current

$J_{c_s}^+$: surface contribution to the critical current when the flux is entering the sample

$J_{c_s}^-$: surface contribution to the critical current when the flux leaves the sample

J_{c_p} : extra critical current at $H = H_p$

k : proportionality factor giving the flux lattice spacing at $H = H_p$; $u_0 = ka_0$

l^* : $(C_{44}\phi_0/C_{66}B)^{\frac{1}{2}}$; criterium for line pinning or point pinning

M : average magnetization of the sample

M_0 : magnetization for $H_{c2} < H < H_{c3}$ due to surface superconductivity

N : defect density

P_v : total pinning force per unit volume

p_m : maximum pinning force between one vortex and one pinning centre

p_m^p : the pinning force in the case that the pinning centre is a point defect

p_m^ℓ : the pinning force in the case that the pinning centre is a line defect

q : pinning parameter times the half-thickness of the sample

R : resistance

R_{300} : resistance at room temperature

r : cut-off length

T_c : critical temperature

T : temperature

u_0 : distortion of a flux vortex due to a pinning centre

W : losses due to an alternating field

x : distance from the axis of the sample

α : $1 - 2(4\pi M_0/H_0)$

α_1 : slope of the reversible magnetization curve near H_{c2}

α_2 : width of the peak near H_{c2}: $(H_{c2} - H_p)/H_{c2}$

β : parameter in the equation giving the reversible magnetization curve: $\alpha_1[(H_{c2} - H_{c1})/H_{c1}]$

γ : pinning parameter: q/d

γ : electron specific heat coefficient of normal metals

δ : thickness of the pinningless surface layer, divided by the half-thickness d

ζ : $(d/\mu_A H_0)(\partial B/\partial x)$

η : $\Delta H/H_0$

κ_1 : Landau-Ginzburg parameter: $H_{c2}/(\sqrt{2}\cdot H_c)$

κ_2 : Landau-Ginzburg parameter: $\alpha_1 = [1.16(2\kappa_2^2 - 1)]^{-1}$

κ_3 : Landau-Ginzburg parameter: $(H_c/H_{c1})^2/\sqrt{2}$

λ : London penetration depth

μ_A : slope of the Abrikosov curve: $(\partial B/\partial H)_{rev}$

μ_{c_2} : slope of the Abrikosov curve near $H_{c_2}(= 1 + \alpha_1)$

μ' : in-phase component of the permeability

μ'' : in-quadrature component of the permeability

ξ : coherence length

ξ : the reduced distance from the axis of the sample: (x/d)

ρ : residual resistance

ϕ_0 : flux quantum: 2×10^{-7} gauss cm^2

ϕ_p : extra angle between a flux line and the surface of the sample due to surface pinning

χ' : in-phase component of the susceptibility ($\mu' = 1 + 4\pi\chi'$)

χ'' : in-quadrature component of the susceptibility ($\mu'' = 4\pi\chi''$)

$4\pi\chi_{c_2}$: slope of the reversible magnetization curve near $H_{c_2}(4\pi\chi_{c_2} = \alpha_1)$

CHAPTER 1

GENERAL INTRODUCTION

A type-II superconductor, unlike a type-I superconductor, is characterized by two bulk critical fields: the lower one H_{c_1} and the upper one H_{c_2}. For magnetic fields smaller than H_{c_1} a complete Meissner state is observed, which means that all magnetic flux is excluded and so B = 0 inside the sample. Above H_{c_2} bulk superconductivity is destroyed; only a thin surface layer remains superconducting up to the surface-critical field H_{c_3}. At field values between H_{c_1} and H_{c_2} magnetic flux quanta (the so-called flux vortices) can penetrate the sample, forming "normal" regions of cylindrical shape with a radius of the order of the coherence length ξ. They are embedded in a purely superconducting matrix. This configuration is called the mixed state. In this thesis most attention is devoted to magnetic phenomena in this field region.

Under the influence of their mutual interaction the vortices form a triangular lattice, which is homogeneous throughout the sample in the ideal case, in the absence of crystal lattice defects. The magnetization curve in this situation is reversible; it is called the Abrikosov curve [1].

Due to the interaction with lattice defects the vortex lattice is pinned to the crystal lattice and it is no longer homogeneous. This feature is called flux pinning. The flux-density gradient that results, leads to a driving force on the vortex lattice. According to Friedel et al. [2] this driving force per unit volume, in the case of a flat sample parallel to the field is given by:

$$F_d = - \frac{B}{4\pi} \left(\frac{\partial H}{\partial B}\right)_{rev} \left(\frac{\partial B}{\partial x}\right) \qquad (1.1)$$

in which $\left(\frac{\partial H}{\partial B}\right)^{-1}_{rev}$ stands for the slope of the reversible Abrikosov induction curve and $\left(\frac{\partial B}{\partial x}\right)$ for the actual induction gradient. This relation is a special case of a more general expression, derived by Evetts et al. [3]:

$$\underline{F}_d = - \frac{\underline{B}(r)}{4\pi} \times \underline{\nabla} \times \underline{H}(\underline{r}) \quad . \qquad (1.2)$$

If the driving force is in equilibrium with the total pinning force per unit volume P_v, $F_d + P_v = 0$, a stable situation is obtained: the critical state.

Several expressions for the pinning force have been proposed in order to describe the critical state. Some of them, in fact, are purely phenomenological expressions for $\partial B/\partial x$, or are based on simple assumptions about the interaction between one vortex and one "pinning centre" [4-12]), but only the more recent ones, following the ideas of Fietz and Webb [13]), take into account the influence of the mutual interaction of the vortex lines on the efficiency of the pinning. Labusch [14,15]) demonstrated that the summation can be performed statistically, and that the mutual interactions between the vortices can be taken into account by introducing the elastic moduli of the vortex lattice. These elastic moduli can be expressed as functions of B and H:

$$C_{11} = C_{66} + \left(\frac{B^2}{4\pi}\right)\left(\frac{\partial H}{\partial B}\right)_{rev} \tag{1.3}$$

$$C_{44} = \frac{B}{4\pi} H_{rev}(B) \tag{1.4}$$

$$C_{66} = \left(\frac{B^2}{8\pi}\right)\left(\frac{\partial H}{\partial B}\right)_{rev} - \frac{1}{4\pi}\int_{H_{c_1}}^{H} B(H')dH' \quad \text{for } B \ll H_{c_2} \tag{1.5}$$

$$C_{66} = \frac{0.475}{8\pi}\,\frac{2\kappa^2 - 1}{(1 + 1.16(2\kappa^2 - 1))^2}\,(H_{c_2} - B)^2 \quad \text{for } B \lesssim H_{c_2} \tag{1.6}$$

in which κ is the Ginzburg-Landau parameter. $C_{11} - C_{66}$ is the compression modulus of the vortex lattice, C_{44} is a measure of the bending of a flux line out of its equilibrium position and C_{66} is the shear modulus.

Using these moduli Labusch [14]) considered a dilute system of point defects and derived:

$$P_v = \frac{N p_m^2}{8\sqrt{\pi}}\left(\frac{B}{\phi_0}\right)^{3/2}\left\{\frac{1}{\sqrt{C_{66}C_{44}}} + \frac{1}{\sqrt{C_{44}C_{11}}}\right\} \tag{1.7}$$

in which p_m is the local interaction between one pinning centre and one flux line and N is the dislocation density. Good and Kramer [16]) considering the case of line defects, found:

$$P_v = \frac{0.1 N p_m^2}{L^2}\left(\frac{B}{\phi_0}\right)^{\frac{1}{2}}\frac{1}{C_{66}}\ln\left\{\frac{r}{2}\left(\frac{B}{\phi_0}\right)^{\frac{1}{2}}\right\} \tag{1.8}$$

in which L is the length over which a vortex is effectively pinned and r is the cut-off distance, related to an interaction radius of a defect. A thorough

review of bulk pinning in type-II superconductors has been given by Campbell and Evetts [17].

The investigations on the influence of flux pinning on the magnetic behaviour of type-II superconductors at Leiden were started by Goedemoed [11]. In the present thesis the influence of the physical lattice imperfections on the pinning phenomenon is discussed. We cut rectangular samples from thin niobium foil (typically 20 x 3 x 0.2 mm), in which the formation of the defect structure was accomplished by cold rolling and successive annealing at several different temperatures up to 1600°C or by neutron irradiation at reactor ambient temperature with doses up to 1.5×10^{20} n/cm^2. The structure of these lattice imperfections were studied by means of electron microscopy. We investigated the irreversible superconducting properties of the niobium samples by studying the magnetic behaviour in stationary magnetic fields as well as in alternating field superimposed on a stationary field, both fields being parallel to the longest axis of the sample.

With the dc magnetization curves we could test the critical state models and correlate them to the actual defect structures. From the ac permeability curves we obtained, in the first place, a possibility to study the surface effects between H_{c_2} and H_{c_3}. Our expectation to obtain also a much more sensitive test of the critical state models in the mixed state was not fulfilled, since we found that the alternating field introduced some additional effects, which, thus far, are not understood, but which make an explanation of the permeability behaviour in terms of the critical state equation impossible.

The calculation of the magnetization and the permeability curves from the theoretical pinning formulae can only be performed if the reversible relation between applied magnetic field and the induction is known. For high-κ superconductors one can easily approximate this relation by setting H = B, but for our niobium samples ($\kappa \simeq 1.2$) this approximation is too crude. For this reason we adopted the phenomenological reversible state model introduced by Kes et al. [18]. They proposed the following analytic expression for the reversible magnetization curve:

$$-4\pi M_{rev}(H) = H_{c_1}\{1 - (\frac{H - H_{c_1}}{H_{c_2} - H_{c_1}})^{\beta}\} \qquad (1.9)$$

in which $\beta = 4\pi\chi_{c_2}(H_{c_2} - H_{c_1})/H_{c_1}$ with $4\pi\chi_{c_2}$ the slope of the reversible magnetization curve near H_{c_2}. The applicability of (1.9) to our samples has been discussed already by Kes [19].

This thesis is a composition of five separate papers, written in a period of several years. Therefore each chapter has been written in a self-consisting form, with its own introduction, description and discussion. A disadvantage of this method is that sometimes repetitions are inevitable and that the fundamental discussion of the pinning phenomenon in general is spread out over five chapters. On the other hand each chapter can be studied independently without any knwoledge of the other chapters. Another consequence of the present way of presentation is that the results and conclusions obtained in one chapter may not be taken into account in any of the foregoing ones, illustrating the progress of our understanding of the pinning phenomenon.

In chapter 2 [20]) we described the influence of physical lattice imperfections due to cold rolling and successive annealing on the dc magnetization, on the resistive transition and on the ac susceptibility.

Chapter 3 [21]) deals with the influence of lattice defects introduced by neutron irradiation on the dc magnetization curve. A comparison of the results with several pinning models is made, leading to a discussion of the character of the pinning centres.

In chapter 4 [22]) we give a discussion of the peak effect as observed in the dc magnetization curve. This is one of the most pronounced effects induced by neutron irradiation. The peak effect as observed in the ac permeability curves is discussed in chapter 6.

In chapter 5 [23]) the permeability is calculated for four simple pinning models. First the case of surface pinning only, then bulk pinning with constant $\partial B/\partial x$ (the so-called London-Bean model), subsequently the London-Bean model extended with extra surface pinning and finally the London-Bean model extended with a surface layer without pinning. The susceptibility results of chapter 2 are discussed in view of these models.

In chapter 6 [24]) we describe the ac permeability behaviour of the neutron irradiated samples. It is demonstrated that an explanation in terms of any critical state model is impossible so that apparently under ac conditions the flux lattice cannot be considered as being in the critical state.

References

1. A.A. Abrikosov, Zh Eksperim. i Teor. Fiz. 32, 1442 (1957); [JETP 5, 1174 (1957)].
2. J. Friedel, P.G. de Gennes and J. Matricon, Appl. Phys. Letters 2, 119 (1963).
3. J.E. Evetts, A.M. Campbell and D. Dew-Hughes, J. Phys. C 1, 715 (1968).
4. H. London, Phys. Letters 6, 162 (1963).
5. C.P. Bean, Rev. Mod. Phys. 36, 31 (1964).
6. Y.B. Kim, C.F. Hempstead and A.R. Strnad, Phys. Rev. 129, 528 (1963).
7. P.W. Anderson, Phys. Rev. Letters 9, 309 (1962).
8. J. Silcox and R.W. Rollins, Appl. Phys. Letters 2, 231 (1963).
9. F. Irie and K. Yamafuji, J. Phys. Soc. Japan 23, 255 (1967).
10. W.A. Fietz, M.R. Beasley, J. Silcox and W.W. Webb, Phys. Rev. 136, A335 (1964).
11. S.H. Goedemoed, thesis, Leiden (1967).
12. A.M. Campbell, J.E. Evetts and D. Dew-Hughes, Phil. Mag. 18, 313 (1968).
13. W.A. Fietz and W.W. Webb, Phys. Rev. 178, 657 (1969).
14. R. Labusch, Crystal Lattice Defects 1, 1 (1969).
15. R. Labusch, Phys. Stat. Sol. 19, 715 (1967); 36, 439 (1969).
16. J.A. Good and E.J. Kramer, Phil. Mag. 22, 329 (1970).
17. A.M. Campbell and J.E. Evetts, Adv. in Phys. 21, 199 (1972).
18. P.H. Kes, C.A.M. van der Klein and D. de Klerk, J. of Low Temp. Phys. 10, 759 (1973).
19. P.H. Kes, thesis, Leiden (1974).
20. C.A.M. van der Klein, J.D. Elen, R. Wolf and D. de Klerk, Physica 49, 98 (1970).
21. C.A.M. van der Klein, P.H. Kes, H. van Beelen and D. de Klerk, J. of Low Temp. Phys. 16, 169 (1974).
22. C.A.M. van der Klein, P.H. Kes and D. de Klerk, Phil. Mag. 29, 559 (1974).
23. D. de Klerk and C.A.M. van der Klein, J. of Low Temp. Phys. 6, 1 (1972)
24. C.A.M. van der Klein, P.H. Kes, H. van Beelen and D. de Klerk, J. of Low Temp. Phys. (in the press).

CHAPTER 2

THE EFFECT OF COLD ROLLING AND HEAT TREATMENT ON THE MAGNETIC BEHAVIOUR IN STATIONARY AND ALTERNATING FIELDS

§2.1 *Introduction*

In a series of previous articles [1-4]) Goedemoed et al. described the penetration of magnetic flux into a very impure superconducting niobium sample. In the experiments reported in this chapter we investigated the influence of the physical lattice imperfections caused by cold rolling and successive annealing.

It is well known that physical and chemical imperfections influence type II superconductors in different ways. De Sorbo [5]) demonstrated that chemical impurities (especially oxygen) decrease the transition temperature T_c, they increase the normal state resistivity ρ_n, they decrease the thermodynamic critical field H_c and the field H_{c1} where the magnetic flux begins to penetrate the sample and they increase the field H_{c2} where the bulk of the material becomes normal. Further the reversibility of the magnetization curves is decreased and the remanent moment is increased.

Narlikar and Dew-Hughes [6]) investigated the influence of plastic deformation caused by cold rolling. It followed that H_{c2} is not influenced. The irreversibility of the magnetization curves and the size of the remanent moment are increased. They reported that an inhomogeneous dislocation distribution causes much stronger pinning than a homogeneous one. Haasen [7]) showed that torsion of a sample increases the irreversibility of the magnetization curve and the remanent moment.

In our present investigations a number of niobium samples, cut from the same cold-rolled foil, were heat treated at different temperatures. So they all had the same chemical purity, but different amounts of physical imperfections. It followed that H_{c1}, H_{c2} and ρ_n at 4.2 K were not much influenced, but the shapes of the magnetization and susceptibility curves and of the resistive transitions were noticeably altered by the temperature of the heat treatment.

§2.2 *Experimental details*

a. Preparation and condition of the samples. We obtained some high-purity niobium from Semi Elements Inc., Saxonburg (Pa), U.S.A. According to the manufacturer it contained, as typical analysis of interstitial and metallic impurities: 2.0 ppm oxygen, 0.3 ppm hydrogen, 4.0 ppm carbon, 5.0 ppm nitrogen, 0 ppm iron and 3 ppm molybdenum.

Some impurities are of special relevance. Oxygen, as stated above, influences the critical quantities, iron interferes by its magnetic orientation [8], and tantalum is typical for the efficiency of the refining process. For this reason these elements were checked. Tantalum and iron were measured after thermal neutron activation in the High Flux Reactor at Petten and oxygen was determined by chemical analysis at the Philips Research Laboratories, Eindhoven. The results were: 140 ± 30 ppm oxygen, 225 ± 5 ppm tantalum and 2.5 ± 1 ppm iron.

A series of samples of gradually increasing physical perfection was prepared by deformation and subsequent heat treatment in the recrystallization region. A crystal with a diameter of 6 mm was cold rolled into foil of 0.15 mm thickness. The surface layer was removed by chemical polishing in a mixture of one part of concentrated HF and three parts of concentrated HNO_3. Rectangular samples of 3 x 30 mm were cut in the rolling direction. A number of them were investigated in this condition, they will be referred to as the P_0 samples. The others were heat treated during one hour in a vacuum better than 2×10^{-7} mm Hg using titanium as a getter. The heat treatment took place at the following temperatures: 1000 ± 5°C, 1180 ± 5°C, 1410 ± 20°C and 1600 ± 30°C. The samples will be indicated respectively by P_{1000}, P_{1200}, P_{1400} and P_{1600}. It was found by chemical analysis that the oxygen content was not significantly altered by the heat treatment.

Grain sizes after recrystallization were determined by light microscopy; 30μ was found for P_{1200}, 90μ for P_{1400} and 350μ for P_{1600}.

More important are the dislocations which were observed by transmission electron microscopy. The unannealed P_0 samples show a dense and hardly resolvable dislocation structure. The P_{1000} samples show nucleation of grains. Low angle grain boundaries, arranged in the rolling direction are predominant, next to a random population of dislocations. After one hour at 1180°C (P_{1200}) the niobium is completely recrystallized, the dislocations in the grains are arranged in networks. In the P_{1400} samples a low dislocation density still persists. In the P_{1600} samples only a few isolated dislocations are observed. A series of

P_0

P_{1000}

P_{1200}

P_{1400}

P_{1600}

1μ

Fig. 2.1 *Transmission electron micrographs of the five niobium samples, all on the same scale, as indicated on the figure.*

P_0

P_{1000}

P_{1200}

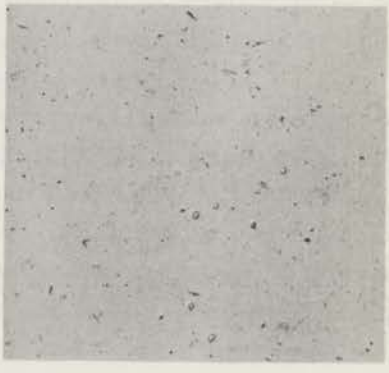

P_{1400}

P_{1600}

10μ

Fig. 2.2 *Surface replicas of the five niobium samples, all on the same scale, as indicated on the figure.*

representative transmission electron micrograph is given in fig. 2.1. They show $12\mu^2$ large areas of specimen, which have been thinned down by chemical polishing to about 0.2μ.

The dislocated densities were counted. The results have been collected in table 2.1.

Table 2.1

Metallographic observations

	Heat treatment (one hour)	Grain size	Dislocation density
P_0	none	-	$> 10^{11}\,cm^{-2}$
P_{1000}	1000 ± 5^oC	nucleation	$(4 \pm 2) \times 10^{10}\,cm^{-2}$
P_{1200}	1180 ± 5^oC	30μ	$(2 \pm 1) \times 10^{9}\,cm^{-2}$
P_{1400}	1410 ± 20^oC	90μ	$(6 \pm 3) \times 10^{8}\,cm^{-2}$
P_{1600}	1600 ± 30^oC	350μ	$< 5 \times 10^{7}\,cm^{-2}$

Also the surface conditions of the samples were inspected using replica electron microscopy. The results are shown in fig. 2.2. Some scratches, about $\frac{1}{4}\mu$ wide, were observed in the case of P_0. They become less pronounced for the other samples and in general the smoothness becomes better the higher the temperature of the heat treatment.

b. Magnetic investigations and resistive transitions. The following quantities were determined in the experiments:

1. The magnetization M as a function of the magnetic field and the temperature.
2. The real and imaginary parts of the ac susceptibility, χ' and χ'', as functions of the magnetic dc field, the amplitude and frequency of the ac field and the temperature ($\chi = \chi' - i\chi''$).
3. The resistance R at 4.2 K as a function of the magnetic dc field and the current through the sample.

The magnetic dc fields were generated by means of a home-made superconducting coil. For the magnetic investigations two samples were glued together with

cellulose laquer, with a constantan wire in between. In some cases a carbon thermometer was painted on the outer surface. The combination as a whole was mounted in a narrow glass tube which was sealed off after a few millimeters of helium gas had been admitted at room temperature [2].

After each experiment in a magnetic field a current of 0.1 A was switched on through the constantan wire for a moment, so that the niobium was heated well above T_c and all the residual flux was expelled. Experiments between 4.2 K and T_c could be performed by continuously passing a much smaller current.

The sample was mounted in a system of coils as shown in fig. 2.3. For the magnetization measurements only the secondary coils were used. They were connected to the input of an integrating circuit, the output being connected to the vertical deflection plates of a Tektronix memory oscilloscope.

The horizontal deflection plates of the oscilloscope were connected through another integrator (a Newport Instruments gaussmeter type J), to the coil on the tail of the inner dewar, the "field measuring coil".

The magnetization curve was displayed on the oscilloscope screen by varying the field of the superconducting coil magnet from zero to above H_{c_2} (or *vice versa*).

Immediately after each magnetization curve the experiment was repeated with the sample heated well above T_c. The "zero curves" obtained in this way were never straight horizontal lines because, due to flux expulsion from the winding space of a superconducting magnet coil, the flux pattern varies with the field strength [9]. This correction proved to be the most serious source of inaccuracies in our magnetization experiments. It is of particular importance at temperatures near T_c.

The susceptibility measurements were performed by connecting both the primary and the secondary coils to a Hartshorn mutual inductance bridge [10] with a phase-sensitive detector at its output. The amplitudes of the alternating magnetic field that we used in the primary coils were 0.72 Oe, 2.41 Oe, 4.81 Oe and 9.52 Oe. The frequency values were 39 Hz, 95 Hz, 216 Hz and 479 Hz.

For the measurements of the resistive transitions two current leads and two potential leads were spot-welded to the sample which, in this case, was mounted directly in the liquid helium. A constant current (1 to 10 A) was passed through the sample and the potential leads were connected to the vertical deflection plates of the memory oscilloscope with a dc amplifier in between. The horizontal deflection plates were connected again to the field measuring coil with the Newport integrator in between.

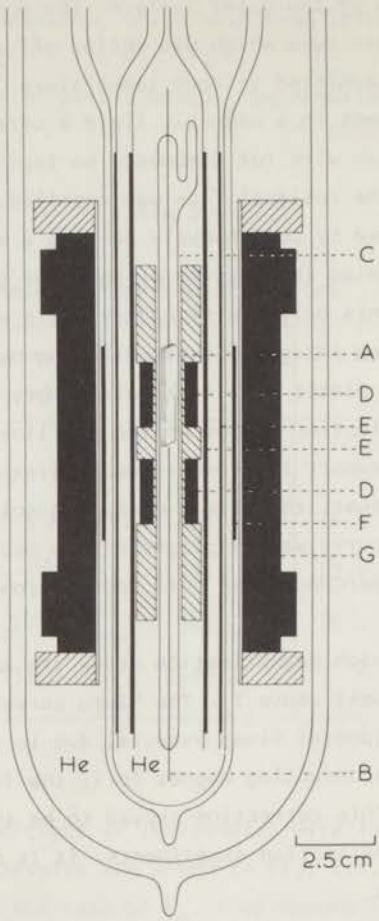

Fig. 2.3 *The cryostat for the magnetic investigations. A samples, B constantan wire, C sample tube, D secondary coils, E primary coils, F field-measuring coil, G superconducting coil magnet. Both dewars contain liquid helium; the surrounding liquid nitrogen vessel has been omitted from the drawing.*

§2.3 *The magnetization curves*

The left-hand half of fig. 2.4 shows the magnetization curves of all five samples at the boiling point of liquid helium. They have been corrected for the zero lines as mentioned in the foregoing section.

The magnetization curve of the unannealed sample P_0 is strongly irrever-

sible. An enormous flux jump is observed in increasing field and the slope in decreasing field almost obeys $-\partial 4\pi M/\partial H = 1$, which means that hardly any of the flux leaves the sample. This indicates strong pinning forces.

The irreversibility of P_{1000} is much less, but still appreciable. There are no flux jumps; also the remanent moment is smaller. There is a region in decreasing field where the magnetization curve is horizontal, which means that the decrease of flux density inside the sample is the same as outside.

In the recrystallized samples P_{1200}, P_{1400} and P_{1600} the maximum near H_{c_1} becomes sharper, the reversibility is improved. No remanent moment is observed any more for P_{1400} and P_{1600}.

The right-hand half of fig. 2.4 shows the magnetization curves at our lowest temperature, 1.05 K. Here the results are similar to those at 4.2 K, but even more pronounced. H_{c_1} and H_{c_2} are larger than at 4.2 K, as should be expected. There is more irreversibility: the number of flux jumps is larger and a remanent moment is observed even for the purest samples.

Fig. 2.5 shows the magnetization curves for P_{1600}, the sample with the smallest amount of dislocations, for a large number of temperatures, varying from just below the transition temperature (T_c = 9.35 K) to the lowest temperature reached in the experiment. The curves are plotted directly ($-4\pi M$ versus H) and on a reduced scale (both quantities divided by H_{c_2}). An almost vertical fall near H_{c_1}, as mentioned by Finnemore, Stromberg and Swenson [11]) and by French [12]) is not observed. This is probably due to the fact that in their experiments moving sample techniques were used by which most of the irreversibility of the magnetization curves is concealed. In our experiments all mechanical shocks and vibrations of the samples were carefully avoided in order to get a clear idea of the irreversibility.

Table 2.2

Critical field values and Landau-Ginzburg parameters at 4.2 K

	H_{c_1} (Oe)	H_{c_2} (Oe)	H_n (Oe)	H_{c_2}/H_{c_1}	H_n/H_{c_2}	H_c (Oe)	κ_3	κ_1	κ_2
P_0	1670	4000	7200	2.4	1.8	2180	1.2	1.3	3.0
P_{1000}	1250	3370	6800	2.7	2.0	1690	1.3	1.4	2.1
P_{1200}	1070	3550	7500	3.3	2.1	1560	1.5	1.6	2.2
P_{1400}	1150	3450	6600	3.0	1.9	1610	1.4	1.5	2.3
P_{1600}	1230	3200	8500	2.6	2.7	1670	1.3	1.4	2.4

In table 2.2 we have collected some data on the magnetization curves at 4.2 K. Here H_{c_1} is defined as the field where the first deviation from linearity is observed; H_{c_2} is the field where the magnetization of the bulk becomes zero, see also the next section.

It turns out that for P_{1000}, P_{1200}, P_{1400} and P_{1600} the positions of H_{c_1} and H_{c_2} are not very much different. This is not surprising since they are much more influenced by chemical than by physical imperfections, as pointed out in section 2.1. Our values of H_{c_1} and H_{c_2} are in good agreement with those of De Sorbo [5]) for the same amount of oxygen (120 ppm). For P_0 the value of H_{c_2} in increasing field is appreciably higher than in decreasing field, which is probably due to the strong pinning forces. For reasons pointed out in section 2.4 we think that the H_{c_2} in decreasing field is the correct one. This value is given in Table 2.2.

The fact that H_{c_1} and H_{c_2} are not much influenced by the defect structure means that the Landau-Ginzburg parameter is not much influenced. Some numbers for 4.2 K are given in table 2.2. Since our values of H_{c_1} and H_{c_2} are not very precise we made use of the simplest relations. First κ_3 was calculated from H_{c_2}/H_{c_1} applying Harden and Arp's graphical solution [13]). Next H_c (the thermodynamic critical field) was calculated [14]) from:

$$\kappa_3 = \tfrac{1}{2}\sqrt{2}\left(\frac{H_c}{H_{c_1}}\right)^2 ,$$

and then κ_1 was derived from:

$$\kappa_1 = \tfrac{1}{2}\sqrt{2}\,\frac{H_{c_2}}{H_c} .$$

The values of κ_2 were obtained from the final slopes $4\pi\chi_{c_2}$ of the magnetization curves, using [15]):

$$4\pi\chi_{c_2} = \frac{1}{1.16(2\kappa_2^2 - 1)} ,$$

but these are less accurate than κ_1 and κ_3 since the final slopes of our magnetization curves are not very well defined.

In increasing field the samples with the lower dislocation densities show a rather steep decrease in the magnetization curves just above H_{c_1}. This takes place at the field where thermal effects on magnetization ($\partial Q/\partial H$) are maximum [4]) and where the magnetic flux reaches the centre of the sample. Furtheron this field will be referred to as H_a^*.

Table 2.3

Occurrence of flux jumps

	Increasing field	Decreasing field
P_0	one at T = 4.25, more for T ≤ 3.05 K	T ≤ 3.50 K
P_{1000}	T ≤ 2.69 K	T ≤ 3.23 K
P_{1200}	T ≤ 1.15 K	T ≤ 2.18 K
P_{1400}	T ≤ 1.15 K	T ≤ 1.67 K
P_{1600}	none for T = 1.05 K	T ≤ 1.67 K

The number of flux jumps that occur at 1.05 K is appreciably larger than at 4.2 K. In fact three different types of jumps are observed at 1.05 K.

a. The sample P_0 shows several large jumps, both in increasing and decreasing fields.

b. In the case of P_{1000} we have regions in which a large number of jumps occur. These jumps are smaller than those of P_0 and the curve between the jumps is more irregular. There is a flux-jump region in increasing field and one in decreasing field. The situation is somewhat analogous to the one we encountered earlier with a sample of much lower purity [2,4]. One or two of such jumps are also observed in decreasing field for P_{1200} and P_{1600}.

c. The samples P_{1200}, P_{1400} and P_{1600} show regions in which large numbers of very tiny flux jumps occur. These regions are indicated in fig. 2.4 by dotted lines since they could hardly be analysed on the oscilloscope pictures.

Some data on the occurrence of flux jumps are collected in table 2.3.

Apart from the flux jumps described above the sample P_{1600} showed, at the lowest temperature, two very peculiar jumps in decreasing fields which even cross the $-4\pi M = H$ (or $B = 0$) line. Until now we have not understood them. The experiment was repeated many times and they were always observed.

Close to H_{c_2} the samples P_{1000} and P_{1200} (and maybe P_0) show a fall in the magnetization curve in increasing field at 1.05 K. This may correspond to the "peak effect" observed in critical current measurements [16,17,18] (see also chapter 4).

From the irreversible magnetization curve we can calculate the induction gradient $(\partial B/\partial x)$ in the samples, using the pinning model of Goedemoed [4]. We made these calculations for the results obtained at T = 4.2 K and it came out that $(\partial B/\partial x)$ is almost independent of x for our samples. The results are

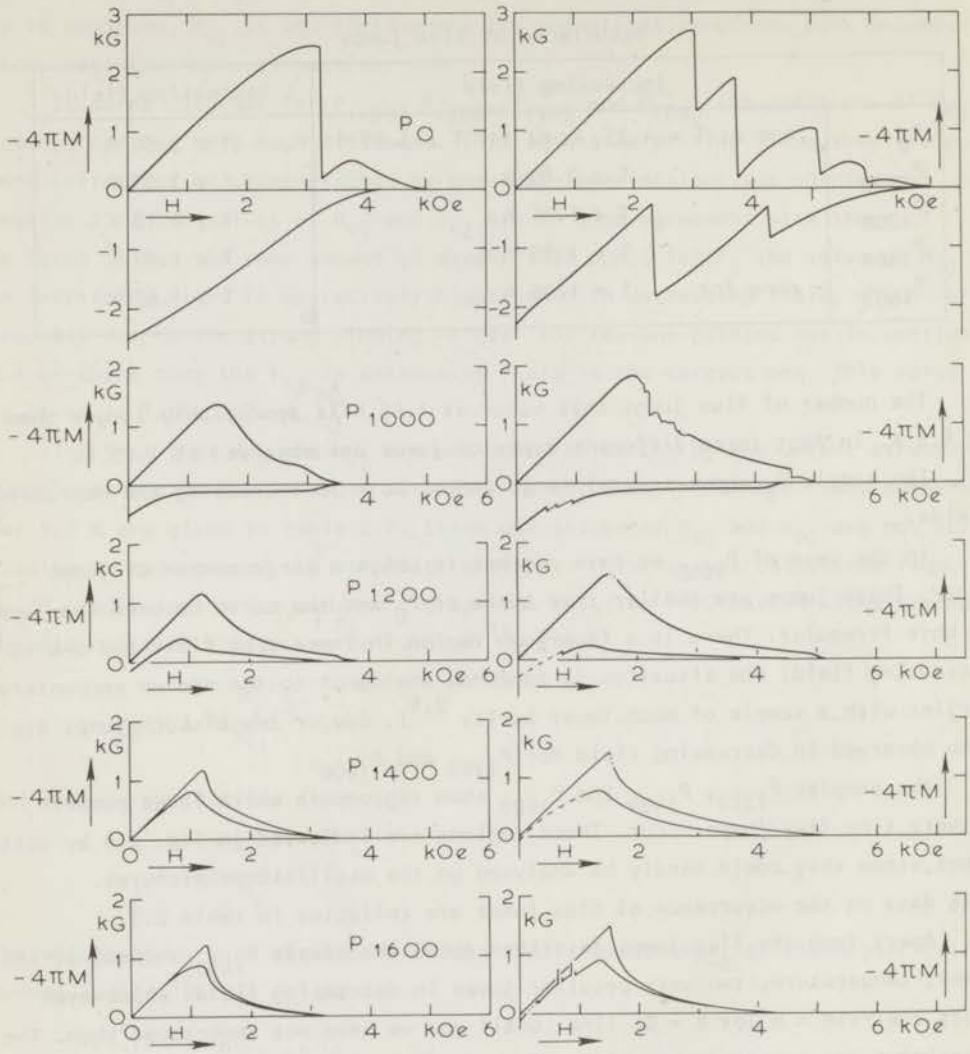

Fig. 2.4 *Magnetization curves of all five samples at T = 4.25 K and T = 1.05 K.*

plotted in fig. 2.6 versus the dislocation density as given in table 2.1 for two different values of the applied field. On a double logarithmic scale the results are two straight lines, with a slope of 2/3.

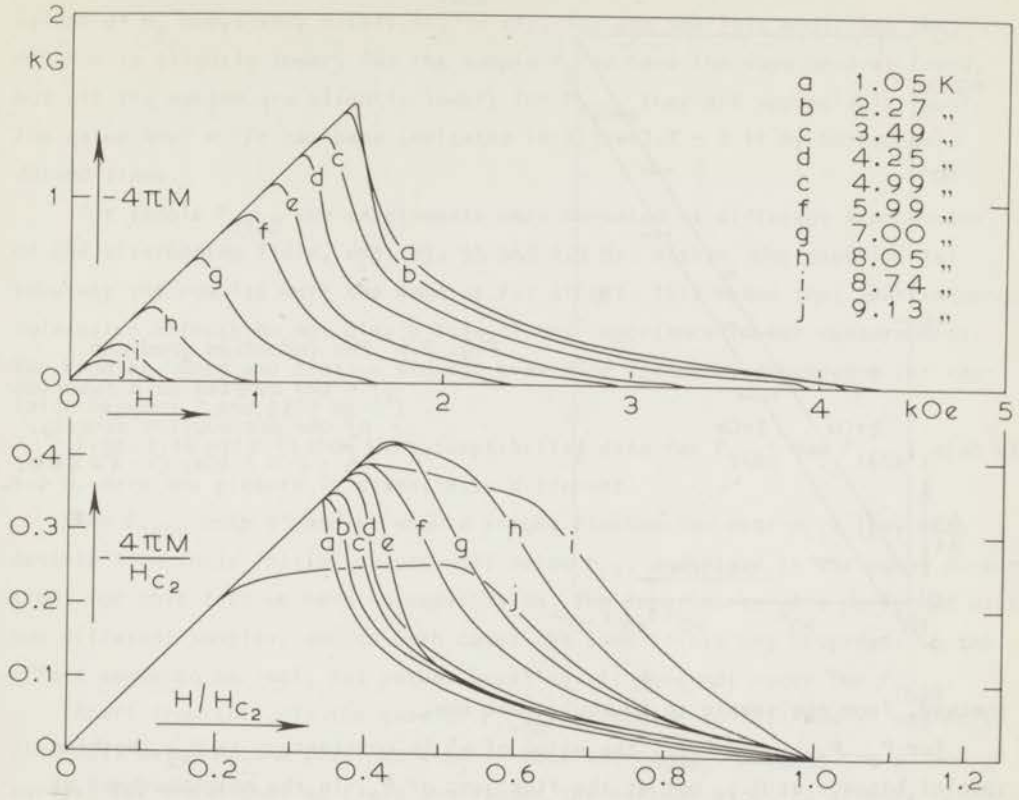

Fig. 2.5 *Magnetization curves of P_{1600} at different temperatures.*

§2.4 *The susceptibility measurements*

The figures 2.7 - 2.11 show the further measurements which we made at 4.2 K with, successively, the samples P_0, P_{1000}, P_{1200}, P_{1400} and P_{1600}. At the top each figure shows the magnetization curve. These curves are identical with those of the left-hand part of fig. 2.4. Below these χ'' and χ' are plotted as functions of the external magnetic field for various values of the amplitude of the alternating field H_0. The frequency was 216 Hz for all these experiments. The vertical scale of χ'' is a factor 2.5 larger than that of χ'. At the bottom we give the resistive transitions for several values of the current through the samples. They will be discussed in section 2.5. Notice that M(H), χ''(H), χ'(H) and R(H) are all on the same horizontal scale. All the curves given here are quite reproducible from one helium run to another and, as far as we have

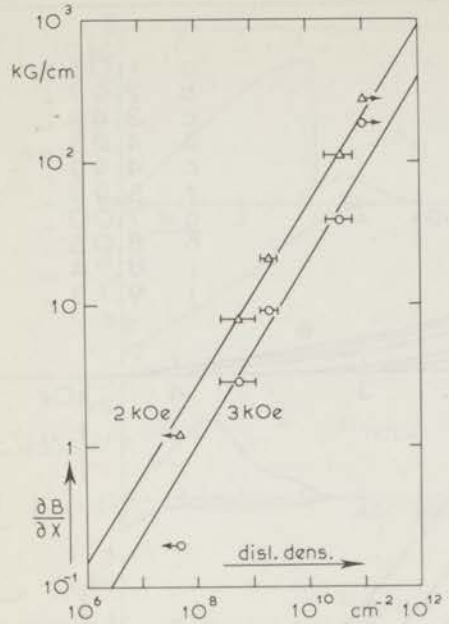

Fig. 2.6 *The induction gradient in the samples as a function of the dislocation density.* Δ : H = 2 kOe; $\circ$: H = 3 kOe.

checked, from one sample to an equivalent one.

For P_0, P_{1000} and P_{1200} the value of χ' is constant up to H_{c2}. Nothing special happens at H_{c1}, nor at the flux jump of P_0. In the neighbourhood of H_{c2} the χ' begins to decrease and this takes place the earlier the larger the amplitude H_0 of the alternating field. χ' goes to zero at a field value which for each sample is approximately independent of the value of H_0. For P_0 the decrease of χ' begins at the H_{c2} value of the magnetization curve in decreasing field and this is the reason why we consider this value as the correct one (see section 2.3).

As long as χ' is constant (below H_{c2}) χ'' is zero for these samples. It starts to increase at the field value where χ' begins to decrease (for each individual value of the amplitude) and, within the precision of the experiments, it becomes zero again when χ' becomes zero. (It can be demonstrated from the data in section 2.5 that the influence of the normal state resistivity on χ'' in high fields is negligible on the scale of our figures.)

The maxima of the χ'' curves for P_0, P_{1000} and P_{1200} coincide very nicely with the corresponding half-values of χ'. We assume that the value of χ' in low fields obeys the relation $4\pi\chi' = -1$. Then the χ'' values can be computed from the calibration of the Hartshorn mutual induction bridge (section 2.2b).

It follows that, in the case of P_{1000}, the maximum of χ'' for the three highest values of H_0 obeys very nicely $4\pi\chi'' = 1/\pi$, for the smallest amplitude the maximum is slightly lower. For the sample P_0 we have the same general trend, but all the maxima are slightly lower; for P_{1200} they are appreciably lower. The value $4\pi\chi'' = 1/\pi$ has been indicated in figs. 2.7 - 2.11 by horizontal dotted lines.

For sample P_{1200} the experiments were repeated at different frequencies of the alternating field, *viz.* 39, 95 and 479 Hz. Within the experimental accuracy the results were the same as for 216 Hz. This means that low-frequency relaxation effects do not play a role of any importance in our measurements. Van Engelen, Bots and Blaisse did not even find frequency dependence for tantalum between 7 and 1200 Hz [19]).

Figs. 2.10 and 2.11 show the susceptibility data for P_{1400} and P_{1600}, also at 4.2 K. Here the picture is essentially different.

For P_{1400} both χ' and χ'' show a slight fluctuation near H_{c_1}. They both deviate from their initial values well below H_{c_2}, and first in the wrong direction! For this fact we have no explanation. The experiments were performed with two different samples, and in both cases the same result was observed. So the effect seems to be real, but rather puzzling. It does not occur for P_{1600}.

Apart from this, in the case of P_{1400}, χ' begins to fall and χ'' begins to rise well below H_{c_2}. A distinct kink is observed at H_{c_2}, both in the χ' and χ'' curves. For the higher ac field amplitudes the maximum of χ'' is already reached before H_{c_2}. The maximum values of $4\pi\chi''$ are well below $1/\pi$ and they deviate markedly from the half-value of χ'.

In the case of P_{1600} a steep deviation from the initial values starts immediately at H_{c_1}. Both χ' and χ'' show a sharp kink a little above H_{c_1}, and the field where it occurs coincides with the steepest point of the magnetization curve, hence with H_a^* (see section 2.3).

Another kink is observed, both in χ' and χ'', at H_{c_2}. The maxima of the χ'' curves are well below the value $4\pi\chi'' = 1/\pi$, the value depends strongly on the amplitude of the alternating field and it does not coincide with the half-value of χ' at all. Very little frequency dependence was found in the experiments again.

We have identified, for each of the samples, the field value where χ' and χ'' become zero, with the nucleation field H_n. The data are given in table 2.2. It turns out that for P_0, P_{1000}, P_{1200} and P_{1400} H_n/H_{c_2} is approximately equal to 2, for P_{1600} it is higher, *viz.* 2.7. One χ'' curve of P_{1600} leads to a still higher value of H_n. Since this is not corroborated by the corresponding χ'

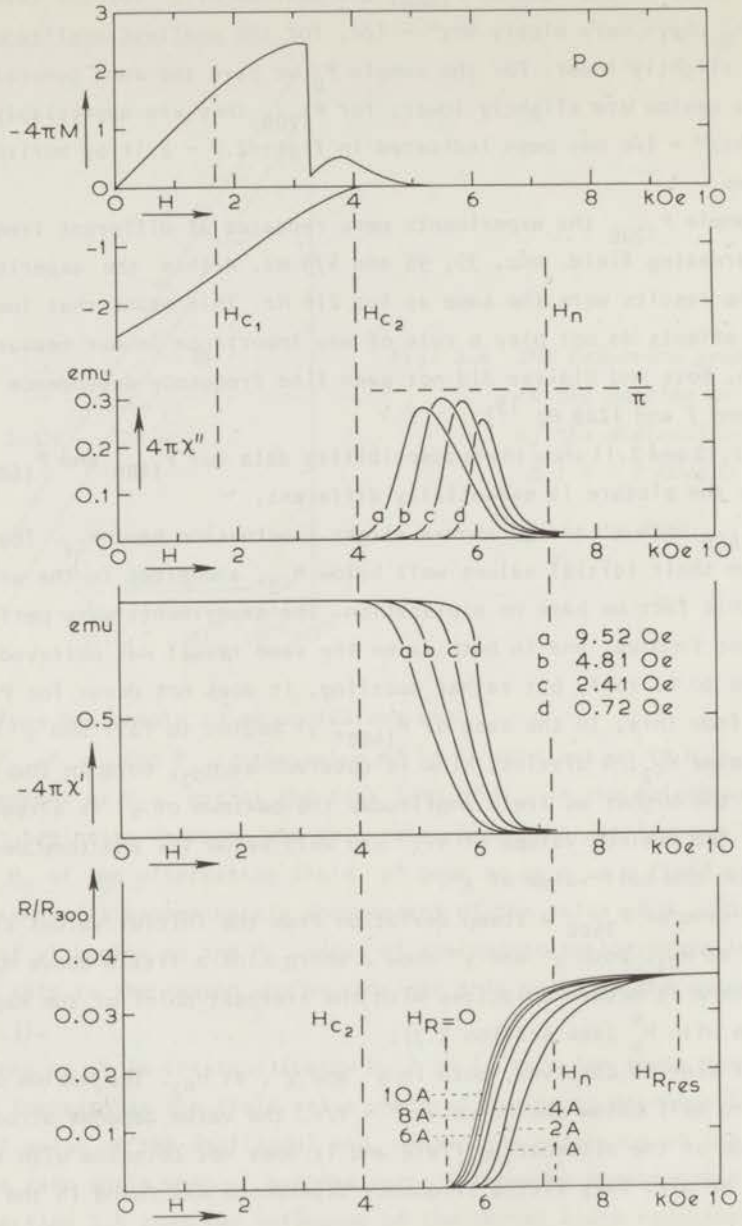

Fig. 2.7 *Magnetization curve, imaginary and real parts of the susceptibility (χ'' and χ') and resistive transition at T = 4.2 K for sample P_0, plotted against the external magnetic field. The amplitudes of the measuring fields and the currents through the sample have been indicated with the curves.*

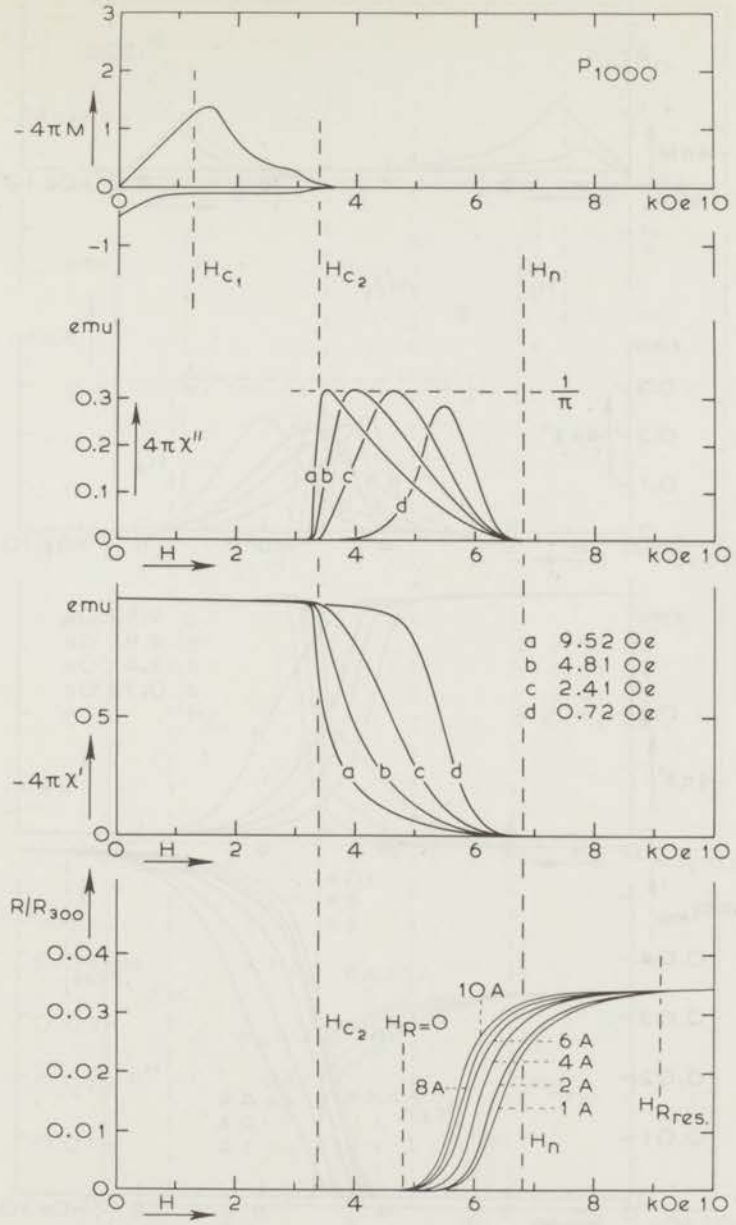

Fig. 2.8 *Magnetization curve, imaginary and real parts of the susceptibility (χ'' and χ') and resistive transition at T = 4.2 K for sample P_{1000}, plotted against the external magnetic field. The amplitudes of the measuring fields and the currents through the sample have been indicated with the curves.*

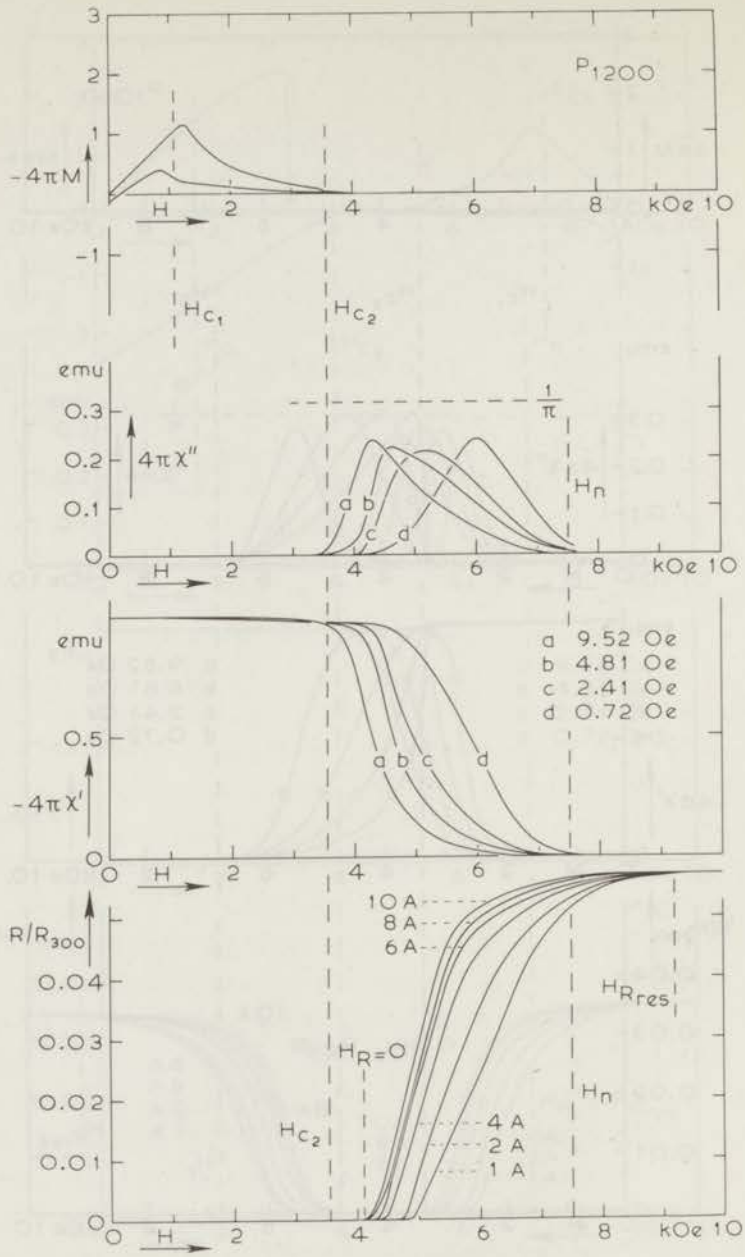

Fig. 2.9 *Magnetization curve, imaginary and real parts of the susceptibility (χ'' and χ') and resistive transition at T = 4.2 K for sample P_{1200}, plotted against the external magnetic field. The amplitudes of the measuring fields and the currents through the sample have been indicated with the curves.*

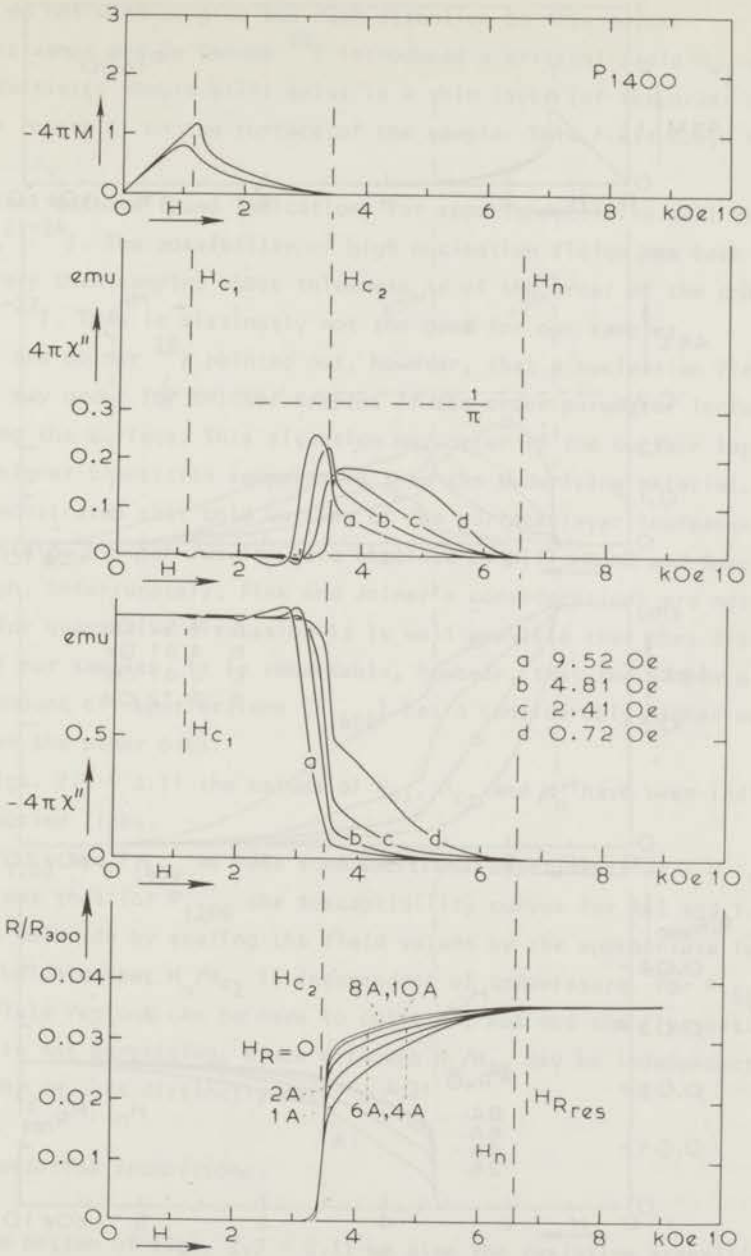

Fig. 2.10 *Magnetization curve, imaginary and real parts of the susceptibility (χ'' and χ') and resistive transition at $T = 4.2$ K for sample P_{1400}, plotted against the external magnetic field. The amplitudes of the measuring fields and the currents through the sample have been indicated with the curves.*

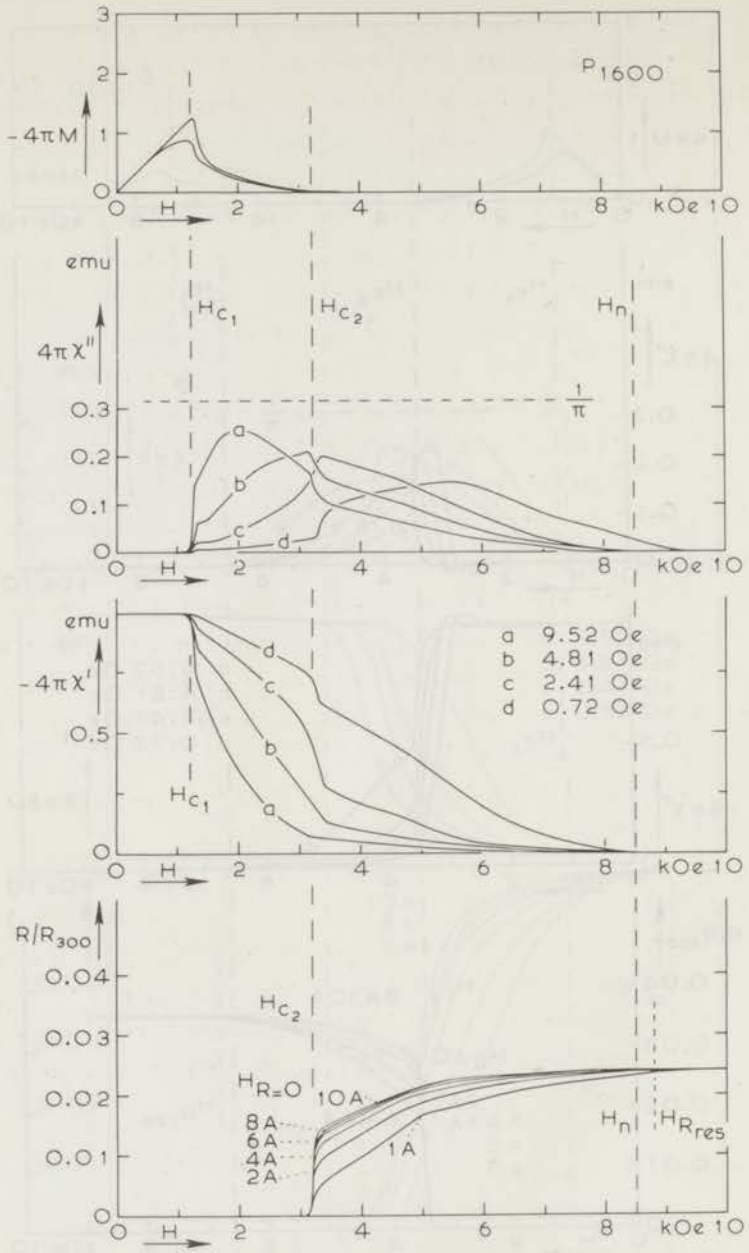

Fig. 2.11 *Magnetization curve, imaginary and real parts of the susceptibility (χ'' and χ') and resistive transition at T = 4.2 K for sample P_{1600}, plotted against the external magnetic field. The amplitudes of the measuring fields and the currents through the sample have been indicated with the curves.*

curve we do not want to give too much attention to this point.

Saint James and De Gennes [20]) introduced a critical field H_{c_3} up to which superconductivity should still exist in a thin layer (of the order of the coherence length ξ) on the surface of the sample. This field obeys $H_{c_3}/H_{c_2} = 1.695$.

Several authors found indications for superconductivity well above $1.695\ H_{c_2}$ [21-24]). The possibility of high nucleation fields has been demonstrated for very thin samples whose thickness is of the order of the coherence length [25-27]). This is distinctly not the case for our samples.

Fink and Joiner [28]) pointed out, however, that a nucleation field well above H_{c_3} may occur for thicker samples if the order parameter increases on approaching the surface. This situation may occur if the surface layer has a slightly higher transition temperature than the underlying material. Fink and Joiner demonstrated that cold working of the surface layer increases the nucleation field. Similar results were obtained by Hill, Kohr and Rose [29]).

Though, unfortunately, Fink and Joiner's considerations are not very accessible for quantative discussion it is well possible that they fit the conditions of our samples. It is remarkable, however, that the sample with the smallest amount of imperfections (P_{1600}) has a considerably higher value of H_n/H_{c_2} than the other ones.

In figs. 2.7 - 2.11 the values of H_{c_1}, H_{c_2} and H_n have been indicated by vertical dotted lines.

For P_{1200} and P_{1400} we made some additional experiments at T = 1.05 K. It turned out that for P_{1200} the susceptibility curves for 4.2 and 1.05 K could be made to coincide by scaling the field values by the appropriate factor. This seems to indicate that H_n/H_{c_2} is independent of temperature. For P_{1400} only the high-field regions can be made to coincide, but not the fluctuations near H_{c_1}. This is not surprising, since although H_n/H_{c_2} may be independent of temperature, H_{c_2}/H_{c_1} is distinctly not.

§2.5 *The resistive transitions*

At the bottom of figs. 2.7 - 2.11 we give the resistive transitions of our samples for various values of the current. A current of 1 A corresponds to a current density of 2.2 A/mm^2.

For P_0, P_{1000} and P_{1200} the resistivity is zero until well above H_{c_2} and the residual resistance is only reached at field values appreciably above the field defined in the foregoing section as H_n. These are the samples for which

$-4\pi\chi' = 1$ and $4\pi\chi'' = 0$ up to H_{c_2}.

For the samples P_{1400} and P_{1600} these effects are not observed. The residual resistance is reached at about H_n (for all the current densities) and the curves show a steep rise at H_{c_2}, which is the larger the higher the current.

The field values where resistance begins to occur ($H_{R=0}$) and where the residual resistance is reached (H_{Rres}) are listed for all our samples in table 2.4. They are indicated in figs. 2.7 - 2.11 by vertical dotted lines.

Table 2.4

Resistive transitions at 4.2 K

	H_{c_2} (Oe)	H_n (Oe)	$H_{R=0}$ (Oe)	$H_{R\,res}$ (Oe)	R_{res}/R_{300}
P_0	4000	7200	5400	9300	0.036
P_{1000}	3370	6800	4800	9100	0.034
P_{1200}	3550	7500	4100	9200	0.057
P_{1400}	3450	6600	3400	6800	0.036
P_{1600}	3200	8500	3200	8800	0.024

It turns out that for samples P_0, P_{1000} and P_{1200} (with dislocation densities above $10^9 cm^{-2}$) there is no correlation between the susceptibility curves and the resistive transitions. For the recrystallized samples P_{1400} and P_{1600}, with lower dislocation densities, there is a very distinct correlation. We come back to this point in section 2.6.

The ratio of the residual resistance and the resistance at room temperature is given for all the samples in table 2.4. It turns out that these ratios are not too much different. For P_0, P_{1000} and P_{1400} they are of the order of 30 (reciprocal of the number in the table). For P_{1600} the ratio is somewhat higher (about 40), which seems plausible; for P_{1200} it is lower, about 17. Since we thought that this sample might have been deformed somewhat during mounting we repeated the experiments with two more samples. The ratios found with these were not much different, about 20.

These resistivity ratios are not particularly high [11]). Our residual resistivity for P_0, P_{1000} and P_{1400} is about 0.55 $\mu\Omega$ cm; this value is in good agreement with De Sorbo's value [5]) for a sample with the same amount of oxygen contamination. So it turns out that our residual resistivities are still

completely determined by the chemical impurities.

It should be realized in general that for a niobium sample with a few hundred ppm of chemical impurities the residual resistance is not a good criterium for the physical lattice imperfection.

§2.6 *Discussion*

Our susceptibility and resistance curves demonstrate that there are two distinctly different types of behaviour, determined by the defect structure. For high dislocation densities (the samples P_0, P_{1000} and P_{1200}) the deviations from $-4\pi\chi' = 1$ and $\chi'' = 0$ do not occur below H_{c_2}. The resistance is zero until well above H_{c_2}, and the residual resistance is reached well above H_n. For the samples with low dislocation density (P_{1400} and P_{1600}) the deviations from $-4\pi\chi' = 1$ and $\chi'' = 0$ begins at lower fields. The fields H_{c_1}, H_a^* and H_{c_2} are clearly observable from the susceptibility curves. Resistance begins to occur at H_{c_2} and the residual resistance is reached at H_n.

The two types of behaviour are not so clear from the magnetization curves. Here the variations are more gradual from one sample to another. The reversibility increases with decreasing amount of imperfections, *i.e.* grain boundaries and dislocations. Beginning with P_{1200} the magnetization curve in decreasing field has a positive part, and beginning with P_{1400} the remanent moment at 4.2 K is zero.

The two types of susceptibility behaviour are most clearly demonstrated in a diagram which is very commonly used in paramagnetic relaxation investigations, but very seldom in superconductivity. It is sometimes called the "Argand diagram" and usually consists of a $\chi''(\chi')$-plot. Fig. 2.12 shows such a diagram for all our samples in a slightly modified form ($4\pi\chi''$ versus $-4\pi\chi'$). For P_0, P_{1000} and P_{1200} the points for different amplitudes of the alternating field are, within reasonable accuracy, on the same curve and the maximum of $4\pi\chi''$ occurs at $-4\pi\chi' = 0.5$. For P_{1400} and P_{1600} there are pronounced systematical differences between the amplitudes, the maxima of $4\pi\chi''$ are in general lower and occur at lower values of $-4\pi\chi'$. So here the curves are strongly asymmetric. The fully drawn curves of fig. 2.12 are based on a theoretical model described in chapter 5, the dotted lines represent a simplified model which was discussed in our original paper (see ref. 21 of chapter 1).

We believe that the susceptibility behaviour of the samples P_0, P_{1000} and P_{1200} is essentially due to surface effects, whereas in P_{1400} and P_{1600} also bulk effects play an essential role. In the case of strong surface pinning the

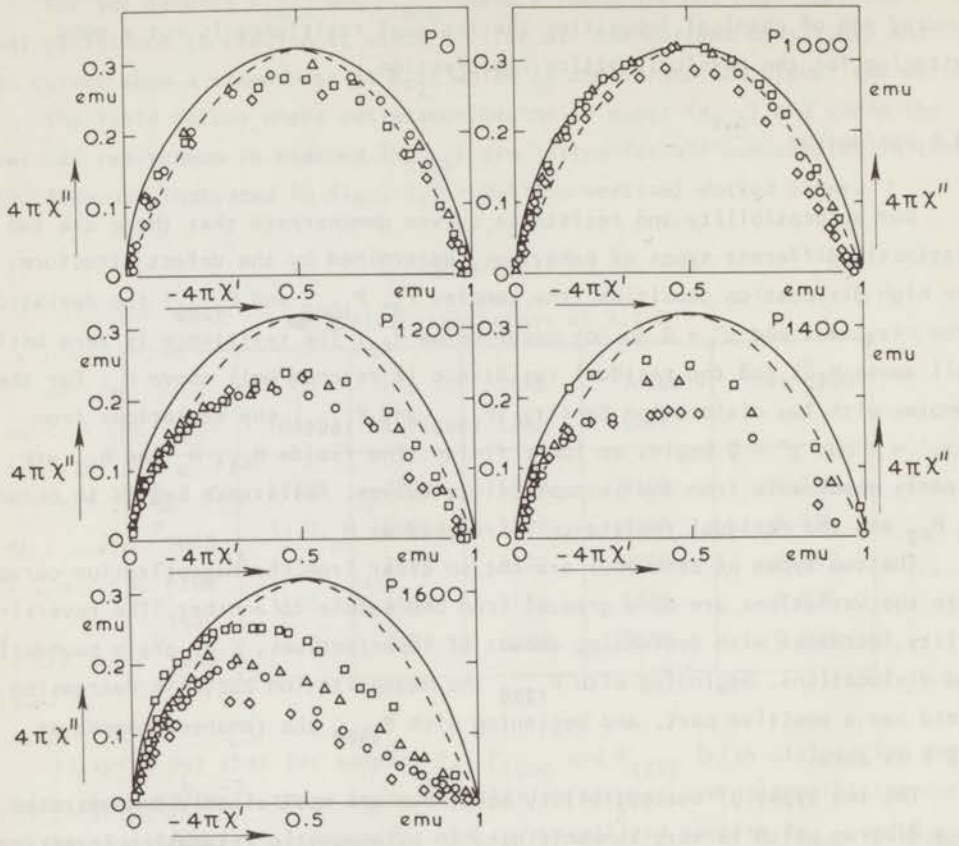

Fig. 2.12 *$4\pi\chi''$ as a function of $-4\pi\chi'$ for the different samples. Theoretical curves and experimental data. Amplitudes of the alternating field:* □ *9.52 Oe,* Δ *4.81 Oe,* ○ *2.41 Oe,* ◇ *0.72 Oe.*

variations of the external field are screened off from the bulk of the sample by surface currents. As long as these currents remain below their upper limit the flux inside the sample remains constant and $\partial M/\partial H$ is equal to $-1/4\pi$. Once the maximum surface current is reached the flux pattern inside the sample varies with the field and the susceptibility deviates from $-1/4\pi$.

For the samples P_{1400} and P_{1600} the surface pinning is relatively weak so that, also below H_{c_2}, the field variations influence the flux pattern, and the more the higher the amplitude. For P_0, P_{1000} and P_{1200} the surface pinning is much stronger so that for the highest amplitude the field variations are

completely screened off, until a field between H_{c_2} and H_n, which is higher the lower the amplitude. The surface pinning of P_{1400} and P_{1600} may be due to an increased smoothness of the surface of the sample, see fig. 2.2.

As was already stated in section 2.5, in the case of the samples P_0, P_{1000} and P_{1200} there is no correlation between the susceptibility curves and the resistive transition. Here the behaviour of the susceptibility is entirely determined by the currents on the surface of the sample and the susceptibility curves give no information about the bulk properties.

We think that for these samples the resistive transition is a bulk effect [30]. The large numbers of dislocations (section 2.2a) give rise to strong local inhomogeneities in the value of the Landau-Ginzburg parameter, so that there are regions in the samples with much harder superconducting properties than the average. At the field H_{c_2} of the sample as a whole they still may form an interconnected structure which can carry an appreciable current. On the other hand these regions are so thin that they do not give rise to an appreciable magnetization. The interconnections begin to break up at $H_{R=0}$ of table 2.4 and the structure eventually becomes completely normal at H_{Rres}, well above H_n, the field where the surface layer vanishes.

For the samples P_{1400} and P_{1600} the situation is different. The number of dislocations is smaller, as can be seen from fig. 2.1, so that there are fewer regions with exceptionally high κ; they are no more strongly interconnected. Here the resistive transition curves are determined by the superconducting surface layer above H_{c_2}. The current-carrying capacity of this layer is rather limited, as follows from the jump in the resistance at H_{c_2}. The residual resistance is reached at H_n, the field where the surface layer vanishes.

Some authors have defined H_n as the field where the sample reaches its residual resistance (see for instance the survey given by Serin [31]). We think that our experiments demonstrate that it is dangerous to draw conclusions about the surface layer from a H_n value obtained in this way. The same conclusion was reached by Smith and Gatos [30].

It should be noticed that the defect structure of P_{1200} takes an intermediate position: it is just completely recrystallized with a very small grain size and a rather high dislocation density persists. This change-over between recovery and recrystallization is reflected in its behaviour. The maximum of $4\pi\chi''$ is distinctly lower than P_0 and P_{1000}, but it does not depend very much on the amplitude of the alternating field. The $\chi''(\chi')$ curve is, at least for the lower amplitudes, somewhat more asymmetric than for P_0 and P_{1000}, but less than for P_{1400} and P_{1600}. Moreover, the distance between $H_{R=0}$ and H_{c_2}, as well

as the distance between H_{Rres} and H_n, is nonzero but noticeably smaller than in the cases of P_0 and P_{1000}. Finally there is a tendency in the 1 A curve of P_{1200} to start rather steeply at 5 kOe, to continue less steeply near 6 kOe and steeper again near 6.5 kOe. This is similar to the behaviour of P_{1600}. So both the resistive transition and the susceptibility give an indication of such an intermediate position. Nevertheless P_{1200} resembles the P_0 and P_{1000} samples more.

References

1. Goedemoed, S.H., Van Kolmeschate, C., De Klerk, D. and Gorter, C.J., Physica 30 (1964) 1225.
2. Goedemoed, S.H., Van Kolmeschate, C., Metselaar, J.W. and De Klerk, D., Physica 31 (1965) 573 (Commun. Kamerlingh Onnes Lab. No. 342b).
3. Goedemoed, S.H., Van Kolmeschate, C., Kes, P.H. and De Klerk, D., Physica 32 (1966) 1183 (Commun. Kamerlingh Onnes Lab. No. 348a).
4. Goedemoed, S.H., Kes, P.H., Jacobs, F.Th.A. and De Klerk, D., Physica 35 (1967) 273 (Commun. Kamerlingh Onnes Lab. No. 356c).
5. De Sorbo, W., Phys. Rev. 132 (1963) 107.
6. Narlikar, A.V. and Dew-Hughes, D., J. mat. Science 1 (1966) 317.
7. Haasen, P., Z. Metallkunde 60 (1969) 149.
8. Alden, T.H. and Livingston, J.D., J. Appl. Phys. 37 (1966) 3551.
9. Graham, C.D. and Hart, R.H., Proc. Int. Cryog. Engng. Conf., Japan, 1967, p. 101.
10. De Klerk, D. and Hudson, R.P., J. Res. Nat. Bur. Standards 53 (1954) 173.
11. Finnemore, D.K., Stromberg, T.F. and Swenson, C.A., Phys. Rev. 149 (1966) 231.
12. French, R.A., Cryogenics 8 (1968) 301.
13. Harden, J.L. and Arp, V., Cryogenics 3 (1963) 105.
14. Maki, K., Physics 1 (1964) 21, 127, 201.
15. Caroli, C., Cyrot, M. and De Gennes, P.G., Solid State Commun. 4 (1966) 17.
16. De Sorbo, W., Phys. Rev. 134 (1964) A1119.
17. Kernohan, R.H. and Sekula, S.T., J. Appl. Phys. 38 (1967) 4904.
18. Pippard, A.B., Phil. Mag. 19 (1969) 217.
19. Van Engelen, P.P.J., Bots, G.J.C. and Blaisse, B.S., Phys. Letters 19 (1965) 465.
20. Saint James, D. and De Gennes, P.G., Phys. Letters 7 (1963) 306.
21. De Sorbo, W., Phys. Rev. 135 (1964) A1190.
22. Gygax, S., Olsen, J.L. and Kropschot, R.H., Phys. Letters 8 (1964) 228.
23. Doidge, P.R., Kwan Sik-Hung and Tilley, D.R., Phil. Mag. 13 (1966) 795.
24. Lowell, J., Phil. Mag. 16 (1967) 581.
25. Tilley, D.R., J. Phys. C1 (1968) 293.
26. Van Gelderen, A.P., Phys. Rev. Letters 20 (1968) 1435.
27. Fink, H.J., Phys. Rev. 177 (1969) 732, 1017.
28. Fink, H.J. and Joiner, W.C.H., Phys. Rev. Letters 23 (1969) 120.

29. Hill, D.C., Kohr, J.G. and Rose, R.M., Phys. Rev. Letters 23 (1969) 764.
30. Smith, F.T.J. and Gatos, H.C., J. Appl. Phys. 39 (1968) 3793.
31. see: Saint James, D., Sarma, G., Thomas, E.J., Type II superconductivity, Pergamon Press (1969) p. 89.

CHAPTER 3

THE EFFECT OF NEUTRON IRRADIATION DAMAGE ON THE MAGNETIC BEHAVIOUR IN STATIONARY FIELDS

§3.1 *Introduction*

Neutron irradiation provides a way to study the interaction between flux vortices and well-defined lattice defects rather systematically, by varying the irradiation dose. The lattice defects can be studied with an electron microscope.

In this chapter we will discuss the d.c. magnetization in longitudinal magnetic fields before and after irradiation. A discussion of the permeability behaviour of the same samples will be given in chapter 6.

Surface effects, which are often the main source of the irreversible magnetic behaviour are removed by oxidation of the samples [1].

§3.2 *The samples*

Rectangular samples of high purity niobium (Material Research Corporation, Marz-grade) with a size of 20 x 3 x 0.2 mm are annealed during one hour at 1600°C in a vacuum better than 10^{-7} torr (see chapter 2). Subsequently they are irradiated at reactor ambient temperatures (40 - 80°C) in the High Flux Reactor of the Reactor Centrum Nederland, Petten. Before irradiation the samples are referred to as N-0, after the irradiation as N-317, N-318, N-319 and N-320 (see table 3.1). The fast neutron doses are defined according to the equivalent fission spectrum. In order to remove the surface effects, some of the samples are heat treated during a few minutes in a pure oxygen atmosphere at 400°C. These samples will be referred to as NO-0 (unirradiated), NO-317, NO-318, NO-319 and NO-320.

Information about the defect structure is obtained from electron microscope pictures as shown in fig. 3.1 (a-f). As is known from the literature [2,3] fast neutron irradiation at room temperature introduces clusters of inter-

Table 3.1

Sample	Average fast flux	Integrated fast flux	Average thermal flux	Integrated thermal flux
N-317	$0.82\times10^{14}\,cm^{-2}s^{-1}$	$3.7\times10^{17}\,cm^{-2}$	$3.1\times10^{14}\,cm^{-2}s^{-1}$	$1.4\times10^{18}\,cm^{-2}$
N-318	$0.83\times10^{14}\,cm^{-2}s^{-1}$	$3.75\times10^{18}\,cm^{-2}$	$3.1\times10^{14}\,cm^{-2}s^{-1}$	$1.4\times10^{19}\,cm^{-2}$
N-319	$0.78\times10^{14}\,cm^{-2}s^{-1}$	$3.65\times10^{19}\,cm^{-2}$	$3.1\times10^{14}\,cm^{-2}s^{-1}$	$1.4\times10^{20}\,cm^{-2}$
N-320	$0.73\times10^{14}\,cm^{-2}s^{-1}$	$1.5\times10^{20}\,cm^{-2}$	$2.5\times10^{14}\,cm^{-2}s^{-1}$	$0.52\times10^{21}\,cm^{-2}$

stitials in the form of loops. It can be seen from fig. 3.1 that the number of clusters increases steeply between a dose of 3.10^{18} and of 3.10^{19} n/cm^2. In sample N-317 (fig. 3.1b) no clusters are found, in N-318 (fig. 3.1c) the first cluster formation can be observed, while in N-319 (fig. 3.1d) the number of clusters is considerable. The average cluster size is about 100 Å, and the spacing between the clusters is of the order of a few hundred angströms. In sample N-320 (fig. 3.1e) a similar spacing is found, but the size of the clusters has increased due to secondary clustering of the loops. It has been pointed out by Brimhall and Mastel [4]) and by Elen et al. [2]) that, in order to minimize the elastic deformation energy, clusters prefer to settle close to each other, forming "rafts". From picture 3.1f it can be seen that the size of these extended defects in N-320 is of the order of 800 Å.

Annealing of the samples at 400°C appears not to affect the cluster pattern, in agreement with earlier investigations, e.g. those on molybdenum reviewed by Eyre [3]).

With the help of the transmission electron microscope and a scanning microscope we made some metallurgical investigations about the surface layer of our oxidized samples. It came out that for oxidation at temperatures below 500°C NbO_2 is formed, above 500°C Nb_2O_5. The oxide layer is extremely thin (about 1 - 0.5 µm), but very well attached to the sample. In the bulk of the sample no effects of the oxidation (such as oxygen clusters, precipitates) could be detected [5]).

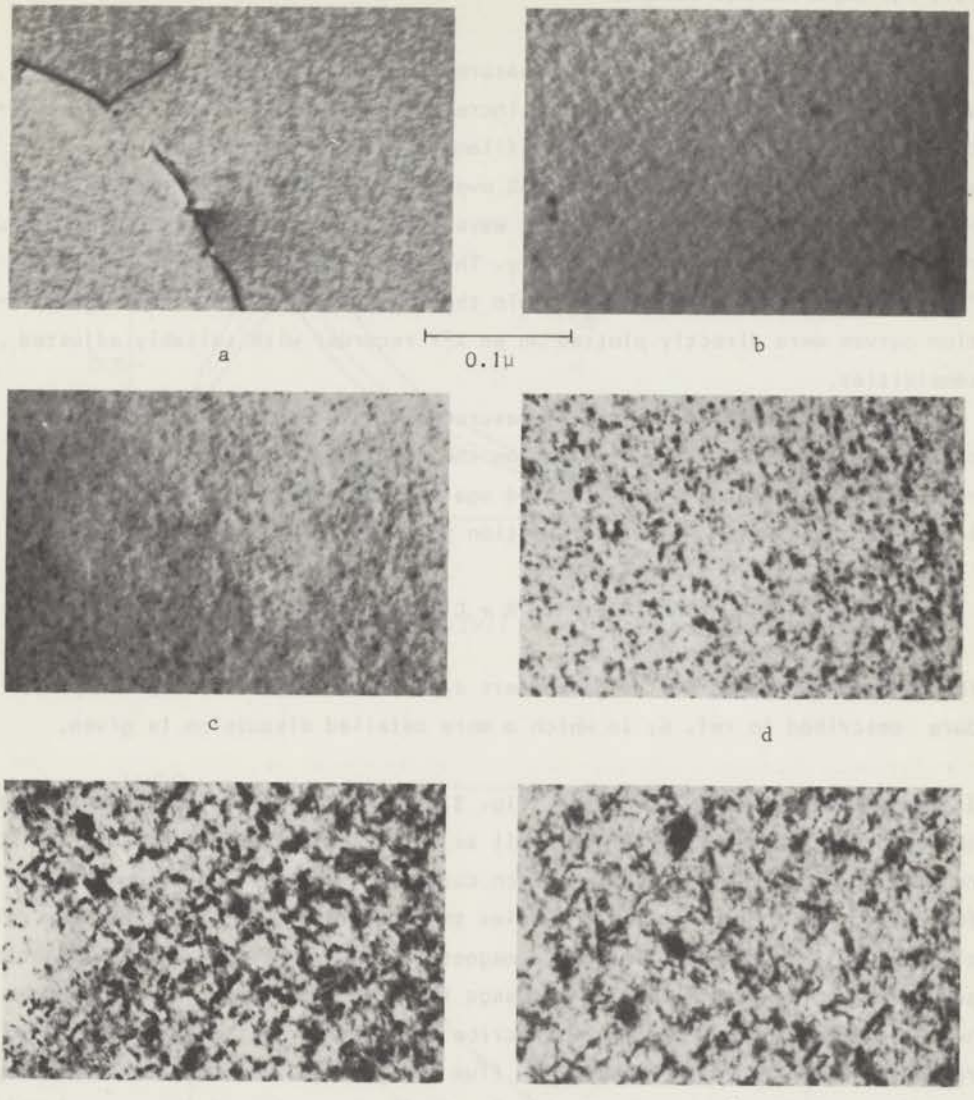

Fig. 3.1 *Electron microscope pictures of the irradiation damage.*

a. unirradiated.

b. after a dose of 3.7 x 10^{17} n/cm^2; no cluster formation.

c. 3.75 x 10^{18} n/cm^2; showing small clusters.

d. 3.65 x 10^{19} n/cm^2; showing increased number and size of the clusters.

e. 1.5 x 10^{20} n/cm^2; showing increased size of the clusters.

f. 1 x 10^{20} n/cm^2; showing rafts.

§3.3 *The experimental results*

The magnetization curves are measured in the way described in chapter 2, but some modifications were made to increase the accuracy. A new superconducting coil was used, wound from multifilament Nb-Ti wire (IMI, A61/33), with a field homogeneity better than 0.05% over a distance of 7 cm. This coil has been calibrated in several different ways with an accuracy of 0.1%. The measuring coils were placed concentrically. These modifications produced straight "zero lines" (see section 2.2b) within the measuring accuracy. The magnetization curves were directly plotted on an X-Y recorder with suitably adjusted sensivities.

Temperatures up to 10 K were measured with a ground-off Allen-Bradley carbon thermometer, which was glued on the sample using "General Electric-varnish". The resistor was calibrated against the vapour pressure of both liquid He and H_2 using the interpolation formula:

$$(\frac{\ln R}{T})^{\alpha} = A(\ln R)^2 + B \ln R + C \qquad \text{with } 0.5 < \alpha < 1.$$

For the determination of the parameters α, A, B and C we followed the procedure described in ref. 6, in which a more detailed discussion is given.

3.3.1 *The unirradiated sample.* Fig. 3.2 shows the magnetization curves of the unirradiated sample before as well as after surface oxidation (N-O and NO-O respectively), at T = 4.2 K. From such curves at various temperatures it is found that for the unirradiated samples the oxidation does not affect the values of H_{c_2}, but it reduces strongly the magnetic irreversibility. As the oxidation process at 400°C is not likely to change the bulk properties (the sample was heat treated at 1600°C before) we ascribe the decrease of irreversibility to a reduction of the surface barrier for flux penetration. This conclusion is supported by the fact that before oxidation (N-O) the maxima of the magnetization ($-4\pi M$) in increasing and decreasing fields are at different field values, H^+_{max} and H^-_{max}, whereas after oxidation (NO-O) these maxima occur at practically the same field. As is shown in fig. 3.3 H_{c_1} (as defined by the field value at the maximum of $-4\pi M$ of sample NO-O) and $\frac{1}{2}(H^+_{max} + H^-_{max})$ of sample N-O are on the same straight line, if plotted versus T^2.

In conclusion we can say that surface effects, which, before irradiation are the main source of the irreversibility, can be removed almost completely by oxidation of the sample. We will discuss the surface effects of these

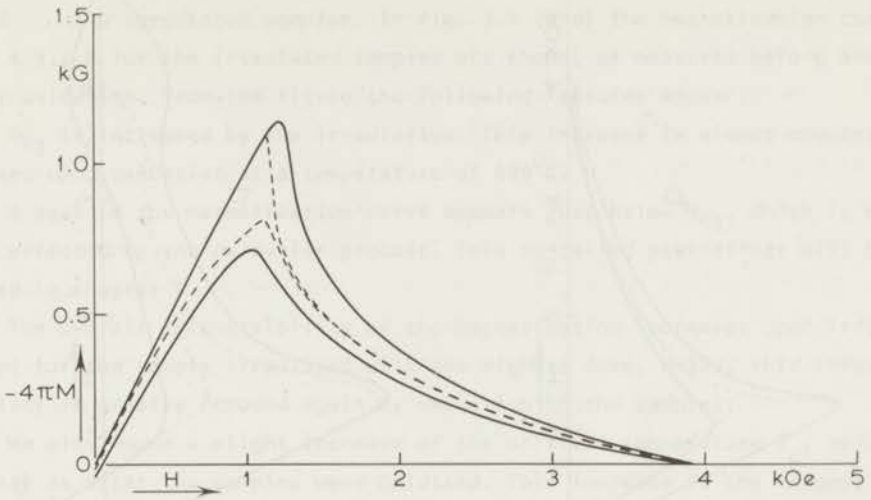

Fig. 3.2 *Magnetization of N-0 (full line) and NO-0 (dotted line) at T = 4.2 K.*

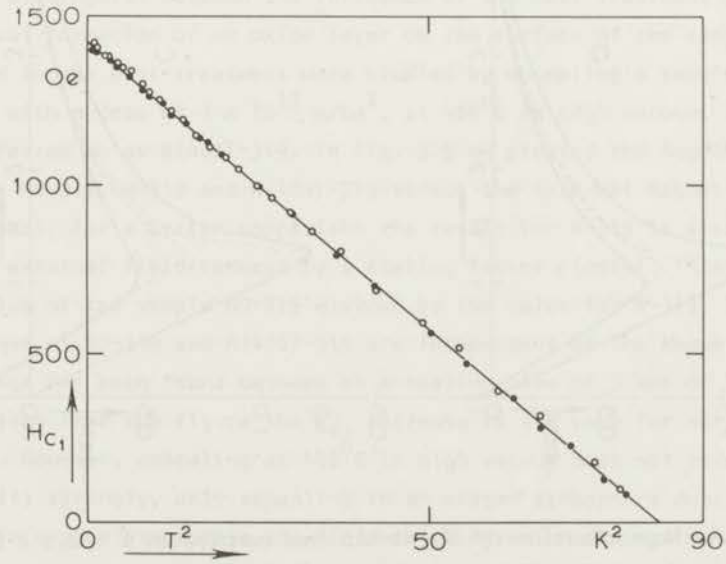

Fig. 3.3 H_{c_1} *versus the square of the temperature for NO-0 (●) and N-0 (○).*

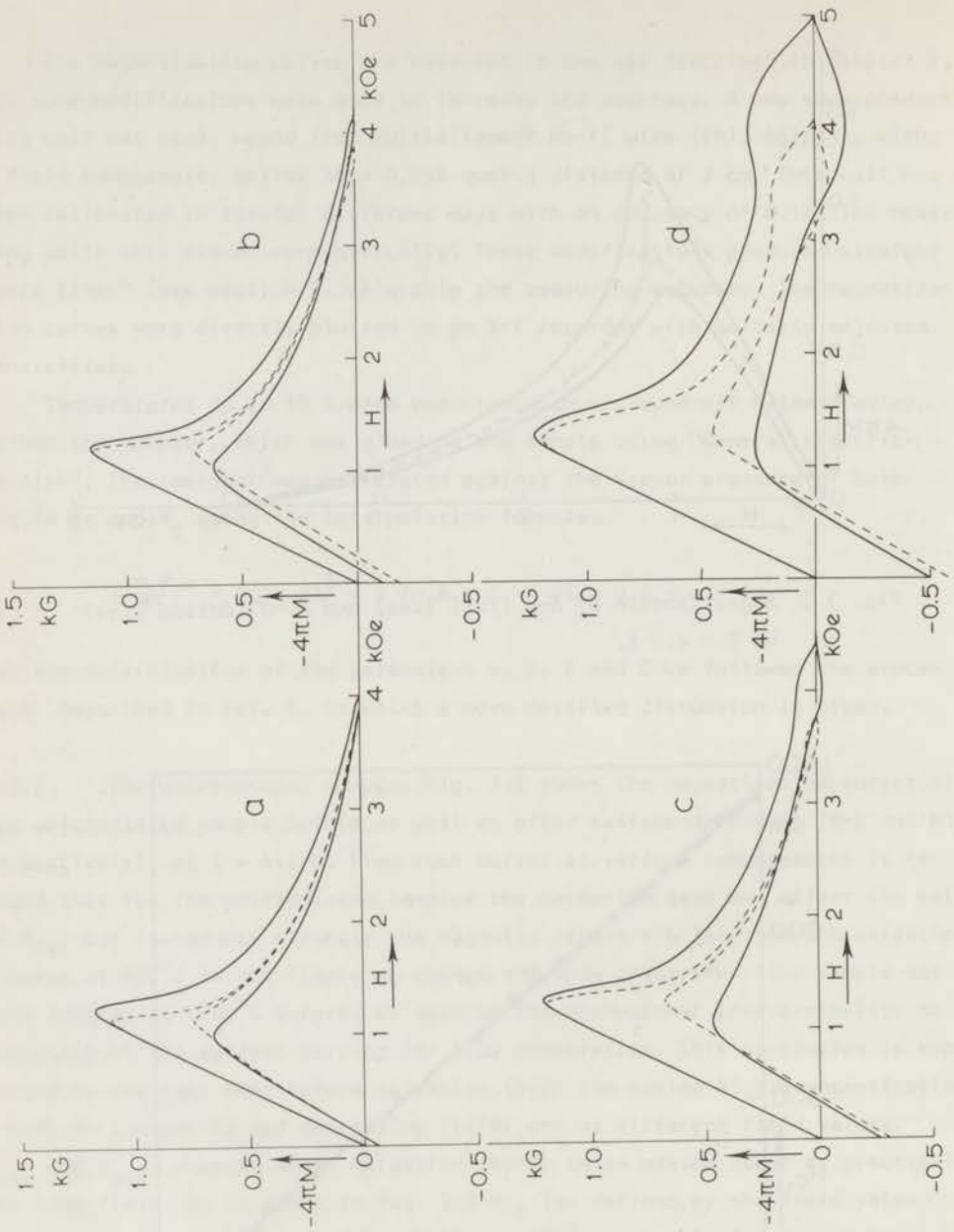

Fig. 3.4 *Magnetization of the irradiated samples at T = 4.2 K before (full lines) and after (dotted lines) oxidation.*
a. after a dose of 3.7 x 10^{17}; b. 3.75 x 10^{18} n/cm^2;
c. 3.65 x 10^{19} n/cm^2; d. 1.5 x 10^{20} n/cm^2.

samples in section 3.4.1.

3.3.2 *The irradiated samples.* In fig. 3.4 (a-d) the magnetization curves at T = 4.2 K for the irradiated samples are shown, as measured before and after oxidation. From the figure the following features appear.

i. H_{c_2} is increased by the irradiation. This increase is almost completely removed upon oxidation at a temperature of 400°C.

ii. A peak in the magnetization curve appears just below H_{c_2}, which is not much affected by the oxidation process. This so-called peak-effect will be discussed in chapter 4.

iii. The overall irreversibility of the magnetization increases upon irradiation. Except for the sample irradiated with the highest dose, N-320, this irreversibility is greatly removed again by oxidation of the samples.

We also found a slight increase of the critical temperature T_c, before as well as after the samples were oxidized. This increase is the largest for the highest dose, for the sample N-320 it is of the order of 100 mK.

In the following sub-sections these features will be treated separately in more detail.

a. The effect of oxidation. In order to investigate the effects of oxidation we have to distinguish between the influence of the heat treatment at 400°C and of the actual formation of an oxide layer on the surface of the sample. The effects due to the heat treatment were studied by annealing a sample, which was irradiated with a dose of 3×10^{19} n/cm^2, at 400°C in high vacuum. This sample will be referred to as N(400)-319. In fig. 3.5 we plotted the magnetization of the samples NO-319, N-319 and N(400)-319 versus the external magnetic field H (full lines). For a better comparison the result for N-319 is also shown versus the external field reduced by a scaling factor α (dots). This factor is the H_{c_2} value of the sample NO-319 divided by the value for N-319. The magnetization curves of NO-319 and N(400)-319 are independent of the annealing time, no difference has been found between an annealing time of 5 and of 30 minutes. As can be seen from the figure the H_{c_2} decrease is the same for NO-319 and N(400)-319. However, annealing at 400°C in high vacuum does not reduce the irreversibility strongly, only annealing in an oxygen atmosphere does. After annealing in oxygen atmosphere the field value at which the maximum of the magnetization occurs is the same in increasing and decreasing field, after annealing in vacuum these fields differ as much as before annealing.

We will discuss these observations in section 3.4.2(a).

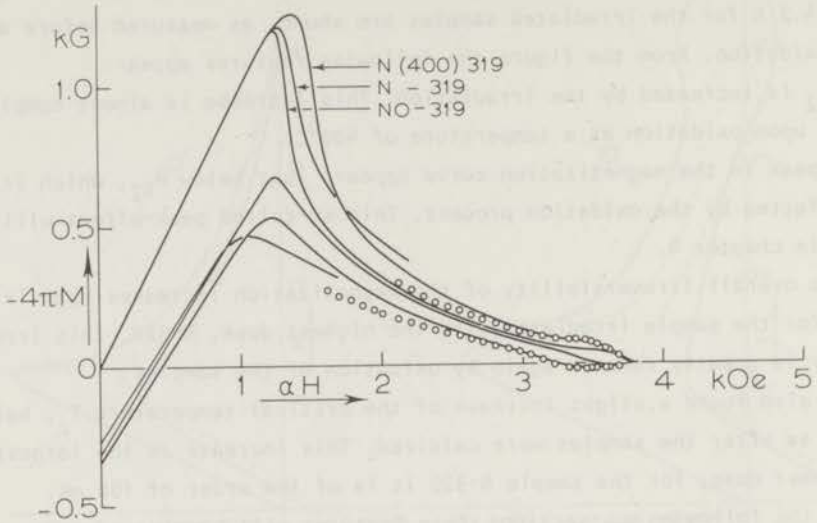

Fig. 3.5 *Magnetization curve of the sample irradiated with a dose of 3.65 x 10^{19} n/cm^2, before and after surface treatments at T = 4.2 K. Full lines; α = 1; O : N-319: α = H_{c_2}(N-319)/ H_{c_2}(NO-319).*

b. The H_{c_2} shift. The increase of H_{c_2} due to the irradiation is shown in fig. 3.6, in which H_{c_2} of the samples before oxidation is plotted as a function of temperature. Also the slight increase of T_c can be seen from the figure.

In fig. 3.7 we show H_{c_2} at T = 4.2 K, before and after oxidation, as a function of the irradiation dose. It appears that heat treatment at 400°C, whether it is carried out in a pure oxygen atmosphere or in high vacuum, removes the shift in H_{c_2} almost completely. The dotted horizontal line represents H_{c_2} for the unirradiated samples. (The rather large deviation from this value for NO-319 and NO-320 proved to be reproducible for all the samples irradiated at these doses.) Similar results were obtained by Brown, Blewitt and Scott [7]), who found that the H_{c_2} increase, induced by low temperature irradiation in some niobium samples, disappeared when the samples were annealed at a temperature of about 300°C. The difference between H_{c_2} before and after treatment, referred to as $\Delta' H_{c_2}$, is plotted against the irradiation dose in fig. 3.8, both on logarithmic scales. The data of Brown et al. [7]) for low temperature irradiation

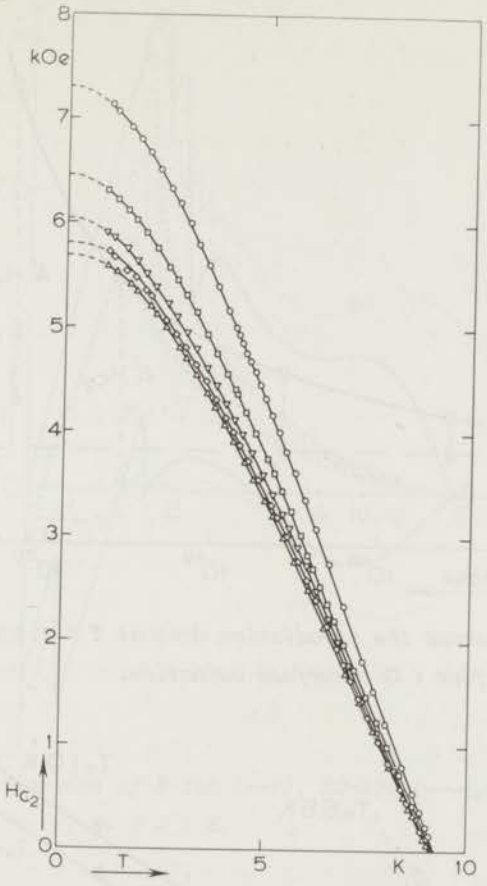

Fig. 3.6 *H_{c_2} versus temperature for N-0 (△), N-317 (◇), N-318 (▽), N-319 (□) and N-320 (○).*

and the results of Kernohan and Sekula [8]) for room temperature irradiations are also given in this figure. As can be seen the increase of H_{c_2} due to low temperature irradiation is much faster than that due to irradiation at room temperature. The slope of the lines, indicating the results of Brown et al., is 1, while for our results the slope is 0.35.

We will discuss these results in section 3.4.2(b).

c. The increased irreversibility. As can be seen from fig. 3.4 most of the irreversibility is due to surface effects. Only for the sample NO-320 a pronounced increase of the irreversibility due to bulk pinning is observed. In fig. 3.9 the magnetization curves at T = 1 K are given for the sample N-320,

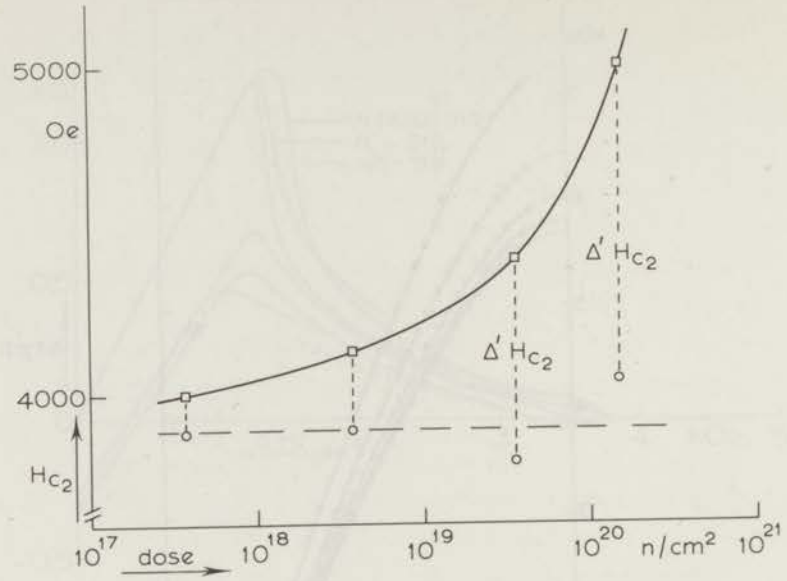

Fig. 3.7 *H_{c_2} versus the irradiation dose at T = 4.2 K, before (□) and after (○) surface oxidation.*

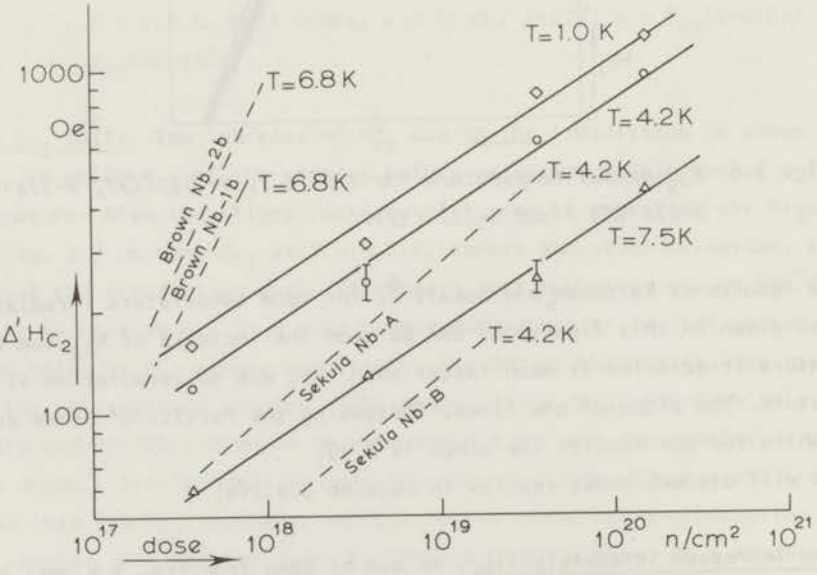

Fig. 3.8 *The increase of H_{c_2} versus the irradiation dose for three different temperatures on log-log scale. Also indicated are other results known from literature.*

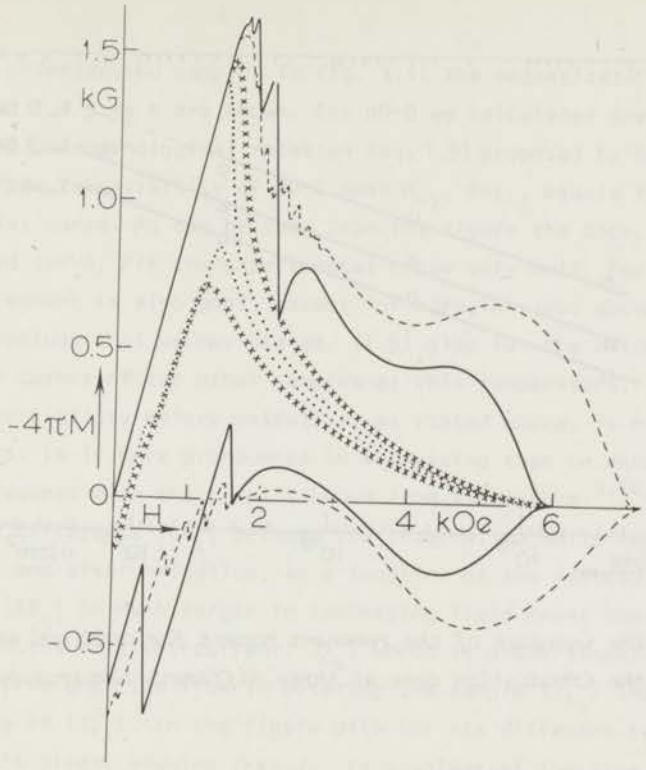

Fig. 3.9 *Magnetization of N-320 (---), NO-320 (——), N-0 (xxx) and NO-0 (····) at T = 1 K.*

NO-320, N-0 and NO-0. Comparison of this figure with figures 3.2 and 3.4d shows that the irreversibility is more pronounced at the lower temperatures, while at these temperatures also a large flux jump region appears.

As a measure of the irreversibility we plotted in fig. 3.10 the remanent moment R at H = 0 of the oxidized samples as a function of the irradiation dose, both on logarithmic scales. Kernohan and Sekula [8]) found also a straight line on a log-log scale, but they observed a much faster increase of R than we did. At a dose of 10^{19} they found a saturation for R = 1300 G at T = 4.2 K. The remanent moment after low temperature irradiation (Brown et al. [7])) saturates already at a dose of 3.10^{17} n/cm^2, but at this dose R is found to be as high as 1600 G at T = 6.8 K.

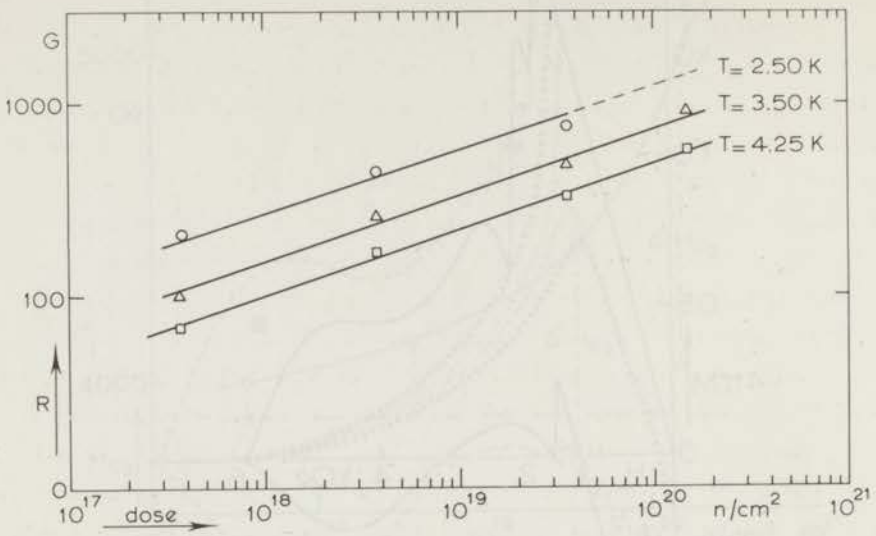

Fig. 3.10 *The increase of the remanent moment for oxidized samples versus the irradiation dose at three different temperatures.*

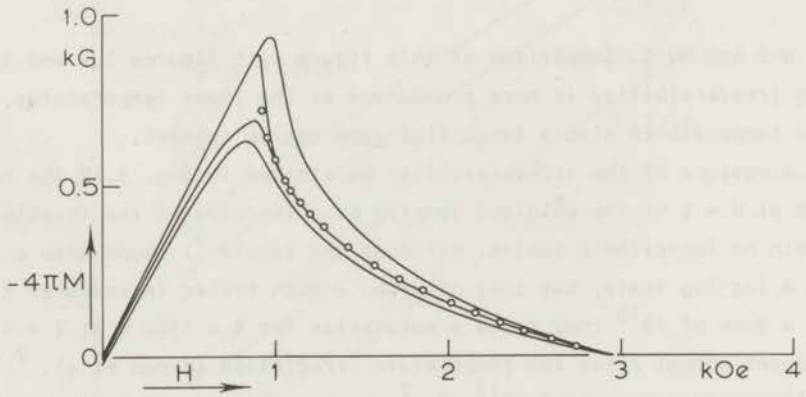

Fig. 3.11 *Magnetization of NO-0 versus H at T = 5.45 K, compared with the theoretical reversible curve (dots).*

§3.4 *Discussion*

3.4.1 *The unirradiated sample.* In fig. 3.11 the magnetization curves for NO-O and N-O at T = 5.45 K are shown. For NO-O we calculated the reversible curve using the phenomenological relation (eq. 1.9) proposed by Kes et al. [1]). On account of the reversibility of NO-O near H_{c_2}, $4\pi\chi_{c_2}$ equals the slope of the experimental curve. As can be seen from the figure the dots, representing this calculated curve, fit the experimental curve very well. For lower temperatures the agreement is also good, except for a region just above H_{c_1}. From this fit we conclude that we may use eq. (1.9) also for the calculation of the reversible curves of the other samples at this temperature.

The irreversibility before oxidation, as stated above, is mainly due to surface effects. It is more pronounced in increasing than in decreasing field. This is in agreement with the results known from literature [9,10]). In fig. 3.12 we plotted the difference $|\Delta B_s|$ between the internal magnetic induction at a given H before and after oxidation, as a function of the reduced field H/H_{c_2}. The fact that $|\Delta B_s|$ is much larger in increasing field means that the surface contribution to the critical current, J_{c_s}, which is proportional to ΔB_s, is far more effective when the flux is entering the sample ($J^i_{c_s}$) than when the flux is leaving it ($J^o_{c_s}$). In the figure data for six different temperatures (2.5 - 6.5 K) is given, showing that J_{c_s} is a universal function of the reduced external field, i.e. $J^{i,o}_{c_s} = f^{i,o}(H/H_{c_2})$. This at first sight rather peculiar property indicates that in our sample, at least in the temperature region considered, the decrease of J_{c_s} due to an increase of the temperature is compensated by the increase of J_{c_s} due to the corresponding decrease of H when H/H_{c_2} is constant.

The asymmetry of the surface contribution to J_c in increasing and decreasing field could be due to the asymmetric Bean-Livingston [11]) barrier. Lowell [9]) calculated for this case that in the low field region:

$$J^i_{c_s} = (H_s - H) + 2B \exp(-\ell/\lambda) ,$$

$$J^o_{c_s} = H - \{8H_s B \exp(-\ell/\lambda)\}^{\frac{1}{2}}$$

in which H_s is the field of the first flux penetration, ℓ is the thickness of the surface layer and λ is the London penetration depth. In spite of the restricted validity of these formulae Lowell found a qualitative agreement with much of the experimental data. Our experimental results, however, cannot be explained

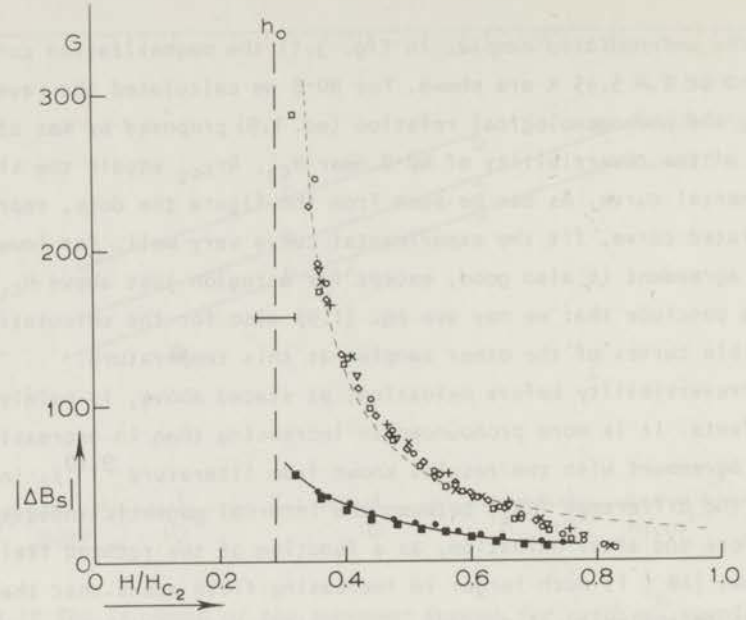

Fig. 3.12 *Surface contribution of the critical current in increasing (open symbols) and decreasing field (black symbols) versus the the reduced magnetic field for some different temperatures. The dotted lines represent a hyperbola and its vertical asymptote.* + : $T = 6.5$ K; , ○: $T = 5.5$ K; ▽: $T = 5.0$ K; ◇: $T = 4.2$ K; x : $T = 3.5$ K and ; □: $T = 2.7$ K.

by this model, not even qualitatively, not only because they do not fit the individual curves for each temperature, but also because they cannot match the temperature dependence we found.

Another explanation of the asymmetry of J_{c_s} was given by Kramer and Das Gupta [12]) who pointed out that enhanced pinning of the flux lines should occur in a surface layer. Due to the fact that in the surface region the shear constant of the flux lattice, C_{66}, (see eqs. 1.5 and 1.6) becomes small, the pinning by the defects becomes more effective. If C_{66} actually vanishes in the surface layer the flux lines become independent of each other in the pinning process. Under these conditions it is possible to calculate an angle γ over which one flux line is tilted out of the field direction. The fact that C_{66} is not really zero can be taken into account by assuming that effectively a number of flux lines n, surrounding the pinned one, is bent over the same angle ϕ_p.

In this way Kramer and Das Gupta obtained the relation:

$$J_{c_s}^{i,o} = \frac{x_s N p_m^2}{n C_{44} \phi_0} \left(\frac{B}{\phi_0}\right)^{\frac{1}{2}} \frac{t}{|\sin(\phi \mp \phi_p)|} \qquad (3.1)$$

in which x_s is the volume fraction of the sample covered by the surface region, N is the defect density, p_m is the maximum pinning force of one defect on one vortex, C_{44} is the elastic modulus for tilting of a flux line out of the field direction, t is an average distance between the pinning centres and the surface, ϕ is the angle between the surface of the sample and the magnetic field and the $\mp$ sign in the argument of the sine refers to the case of flux entering and leaving the sample respectively. In view of this formula no difference should be expected between $J_{c_s}^{i}$ and $J_{c_s}^{o}$ in our experiments, where the field was parallel to the surface of the sample ($\phi = 0$).

In a second paper [10]) Das Gupta and Kramer added an extra angle ζ to the argument of the sine, in order to explain their experimental results on the ϕ dependence of $J_{c_s}^{i,o}$, which they thought could be due to a refraction of the unpinned flux line at the surface of the samples by the Bean-Livingston barrier [11]). In our opinion ζ can also be related to the roughness of the surface. Due to this roughness the angle between a flux line and some part of the surface may not be zero, in spite of the fact that the field is parallel. So the average value of ϕ equals zero, whereas the average of $\sin(\phi \mp \phi_p) \neq \sin(\mp \phi_p)$. This may be accounted for, in practice, by the introduction of an extra angle ζ. Now a difference between $J_{c_s}^{i}$ and $J_{c_s}^{o}$ can be expected, even for $\phi = 0$.

Unfortunately we cannot compare our experimental results with formula (3.1), firstly because we have not varied ϕ and secondly because the field and temperature dependence of J_{c_s} in this formula is uncertain, mainly due to the factor n. On the other hand, the shape of the curves in fig. 3.12 gives some indication that the surface contribution of J_c is indeed mainly due to an enhanced pinning in the surface region, as the shape of this curve is very similar to those predicted by different models for bulk pinning (see section 3.4.2(c), fig. 3.20) rather than the one predicted by the Bean-Livingston barrier. The dotted lines in the figure represent a hyperbola and its vertical asymptote at H'/H_{c_2}. The hyperbola was fitted to our experimental results by determining H' and α' from a $(\Delta B_s)^{-1}$ versus H/H_{c_2} plot. From fig. 3.12 we conclude that our experimental results can be approximated reasonably well by the hyperbola:

$$J_{c_s}(H - H') = \alpha' H_{c_2} \qquad (3.2)$$

In increasing field H'/H_{c2} is found to be equal to H_{c1}/H_{c2}, averaged over the temperature region considered. (The variation of H_{c1}/H_{c2} is indicated by the horizontal bar in the figure.) This rather crude approximation, similar to the critical state model of Kim et al. [13], can be useful in order to compare the pinning in the surface before and after irradiation, as it provides us with a measure of the effectiveness of this pinning, α'.

3.4.2 *The irradiated samples.*

a. The surface effects after irradiation. From the results described in section 3.3.2(a) (see fig. 3.5) we concluded that heat treatment at 400°C in an oxygen atmosphere leads to a much more reversible magnetization curve, but annealing in high vacuum does not influence the irreversibility. We conclude that, just as in the case of the unirradiated samples, the oxidation removes the irreversible surface barrier, while the pinning centres are not influenced. This is in agreement with the electron microscope pictures, which show no difference in the defect structure. Unfortunately, due to the H_{c2} shift, we cannot investigate the surface barrier simply by comparing the magnetization curves before and after oxidation. We can only discuss the surface effects after irradiation by comparing the samples N(400)-319 and NO-319, which were both irradiated with a dose of 3.10^{19} n/cm^2 but were annealed, respectively in vacuum and in an oxygen atmosphere.

The magnetization curves for these samples are shown in fig. 3.5. We found that, also for these samples, the surface barrier, which, due to the peak effect, can only be discussed in the low field region, is asymmetric with respect to the direction of motion of the flux lines. In fig. 3.13 we plotted the surface barrier in increasing field for three temperatures versus the reduced external field. As can be seen the same temperature dependence as for the unirradiated samples is found. The full line in the figure represents the experimental data of fig. 3.12, so it gives the results for the unirradiated samples. The shift between the two curves is partly due to the difference in the average value of H_{c1}/H_{c2} (as can be seen from fig. 3.7 the H_{c2} value for NO-319 is somewhat lower than for NO-0), but it is also due to an increased pinning. From a $(\Delta B_s)^{-1}$ versus H/H_{c2} plot we derived a value for the constant α' in formula (3.2), which is only 20% higher than the one obtained for NO-0. In comparing this to the increase of the bulk pinning, which is considerably larger, we conclude that the surface barrier is not much affected by the irradiation.

This result seems to be in contradiction with the idea that the surface contribution to J_c is due to pinning. But it appears that no cluster formation

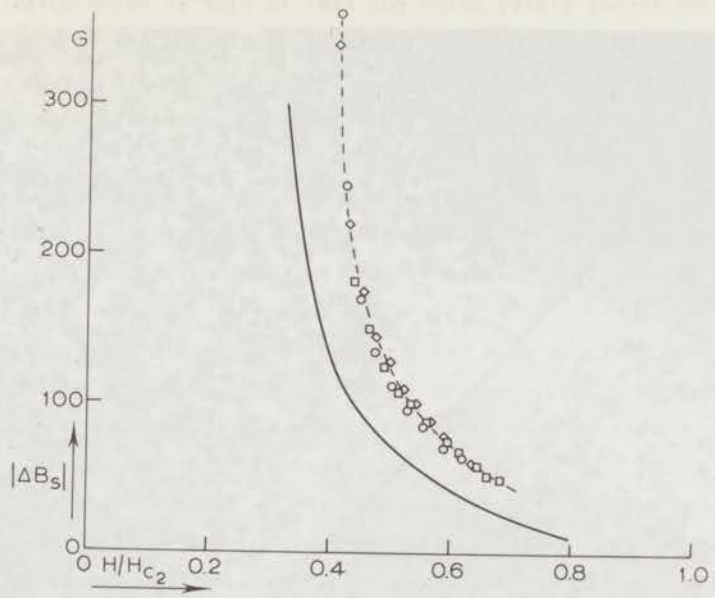

Fig. 3.13 *Surface contribution of the critical current in increasing field for N-0 (full line) and N(400)-319 (dotted line).* ◇ : *T = 3.25 K;* □ : *T = 3.75 K;* ○ : *T = 4.2 K.*

takes place in the surface layer. This is illustrated by an electron microscope picture of N-319 given in fig. 3.14, which shows a grain boundary. It is clear that, near the boundary, there is a region in which no clusters are observed. The reason is that in this so-called "denuded zone" the interstitials, formed during the irradiation, are absorbed by the grain boundary before they can cluster. This is because the grain boundary can be considered, energetically, as a sink for the interstitials. It is plausible that such a denuded zone is also formed at the surface of the sample and this explains why the irradiation does not affect the surface barrier too strongly.

A rather accurate method for investigating the surface barrier of the irradiated samples is the measurement of the permeability in alternating fields. We will discuss this in chapter 6.

b. The H_{c_2} shift. We discussed in section 3.3.2(b) that due to the irradiation H_{c_2} is increased. Heat treatment at 400°C in an oxygen atmosphere as well as in high vacuum reduces H_{c_2} again to its original value. So, in spite of the fact

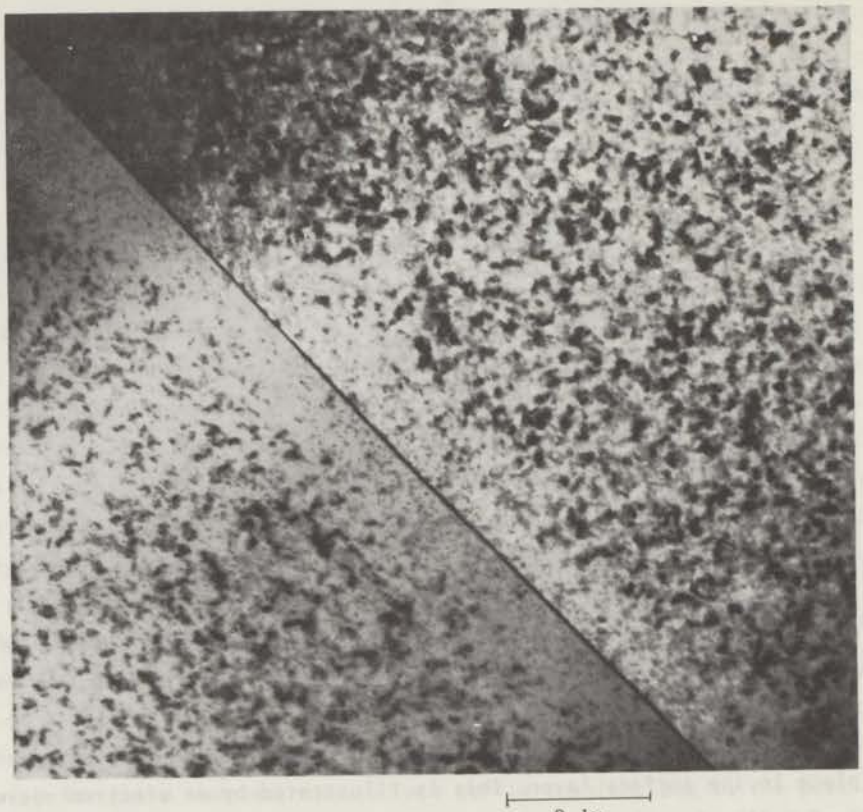

Fig. 3.14 *Electron microscope picture of N-319, showing a denuded zone.*

that the pinning centres are not influenced H_{c_2} is strongly affected by heat treatment. We can explain this by assuming that annealing at 400°C influences small irradiation defects (small clusters, perhaps interstitials and vacancies, the so-called Frenkel pairs). As these defects reduce the electron mean free path and thereby increase the residual resistance ρ, the Ginzburg-Landau parameter κ is increased according to the relation given by Goodman [14]):

$$\kappa = \kappa_0 + C\gamma^{\frac{1}{2}}\rho \quad ,$$

in which γ is the electronic specific heat coefficient and C is a numerical constant. Since $H_{c_2} = \sqrt{2}\kappa H_c$, $\Delta' H_{c_2}$ should be proportional to the increase of the residual resistance. We measured ρ and it appears that indeed the resistance

increases due to the irradiation, but after annealing at 400°C decreases again to a value which is more or less the value before the irradiation. The difference between the value before and after annealing is referred to as $\Delta\rho$. In fig. 3.15 we plotted $\Delta'H_{c_2}$ versus $\Delta\rho$. It can be seen that $\Delta'H_{c_2}$ is proportional to $\Delta\rho$ as was expected. This also explains why the H_{c_2} increase is much faster for samples irradiated at lower temperature [7], because the Frenkel pairs, which are induced by the irradiation, will not cluster at low temperatures. Therefore the electronic mean free path is influenced much more, which gives rise to a much faster increase of the residual resistance and consequently of H_{c_2}.

From the considerations given above we can also conclude that for our samples ρ is hardly influenced by the large clusters, so in general ρ is not a good measure of the pinning of a sample (see also chapter 1).

c. Irreversible effects due to bulk pinning. In this section we will restrict ourselves to a discussion of the irreversibility of the oxidized samples, in which only bulk effects play a part. A thorough review of bulk pinning in type II superconductors has been given by Campbell and Evetts [15].

In order to describe the irreversibility of a superconductor we not only have to know the local pinning force p_m of one pinning centre on one vortex but also how the local pinning forces add up, giving a bulk pinning force density P_v. In order to carry out this summation the influence of the mutual interactions between the vortices on the efficiency of the pinning has to be taken into account. This problem was discussed extensively by Fietz and Webb [16] and solved in principle by Labusch [17]. He introduced the elastic moduli of the flux lattice and (eqs. 1.3 - 1.6) demonstrated that they can be deduced from the reversible magnetization curve.

We calculated C_{11} for NO-320 at T = 5.49 K, using the experimental magnetization curve (shown in fig. 3.18) and the reversible curve, which was obtained using the method proposed by Kes et al. [1] (eq. 1.9) by applying eqs. 28(a) and (b) and method (ii) of their paper. The results are given in fig. 3.16.

By statistical summation Labusch [17] found that for a dilute system of point defects the pinning force per unit volume is given by eq. (1.7). Good and Kramer [19] found that for line defects the pinning force per unit volume is given by eq. (1.8).

In most samples both pinning due to point defects and due to line defects will occur. Therefore it must be expected that most irreversible magnetization

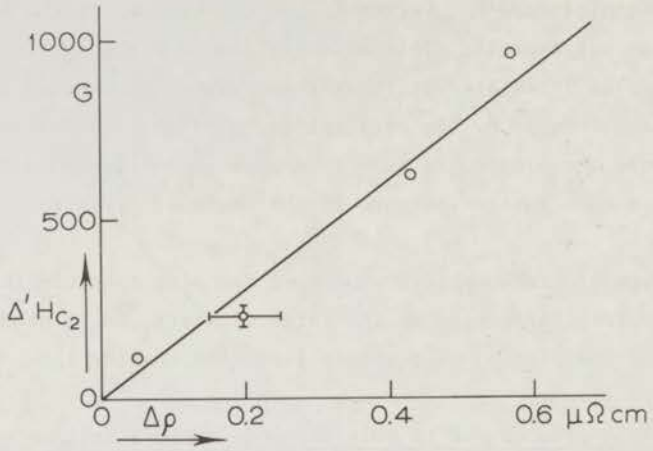

Fig. 3.15 *The increase of H_{c_2} due to the irradiation versus the increase of the residual resistance.*

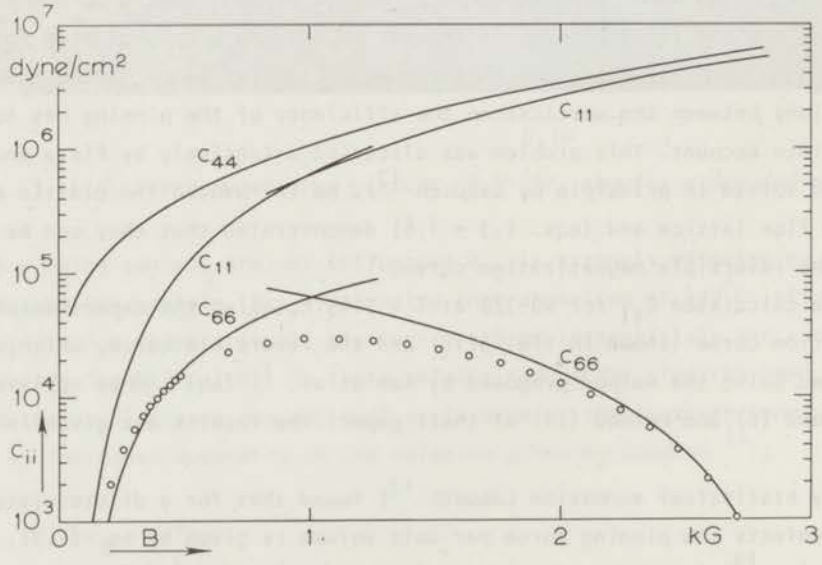

Fig. 3.16 *Elastic moduli C_{11}, C_{44} and C_{66} for NO-320 versus the average internal induction. The dots represent the results obtained from eq. 3.3.*

curves can only be described by a combination of the formulae (1.7) and (1.8). This idea is corroborated by the fact that some empirical critical state models [20,21], which are not directly related to one of the above formulae, give, in many cases, a rather good description of the irreversible magnetization curves [1].

Kramer [22] defined a critical length l^* given by:

$$l^* = \left(\frac{C_{44}\Phi_0}{C_{66}B}\right)^{\frac{1}{2}}$$

He suggested that if the spacing of the defects is much smaller than l^* they can be treated as line defects, if the spacing is much larger the pinning can be considered as being due to point defects.

In order to investigate whether the defect structure in our samples must be considered as point or as line defects we calculated l^* for NO-320 at T = 5.49 K and (for high fields only) at T = 3.25 K, and also for NO-319 at T = 4.20 K. The results are given in fig. 3.17 as a function of B/B_{c_2}. The horizontal dotted line represents the spacing of the defects, as obtained from the electron microscope pictures. As can be seen from the figure l^* increases very rapidly when H_{c_2} is approached. In the neighbourhood of H_{c_2} l^* is much larger than the cluster spacing, so we believe that in this field region only line pinning plays a role. This is also in agreement with the occurrence of the peak effect which can only be explained by pinning due to line defects [17]. We will discuss the peak effect in relation to pinning due to both line and point defects in chapter 4. Near H_{c_1} l^* also increases but at intermediate fields one could expect a combination of line and point pinning. Therefore we decided to calculate the magnetization curves with both formulae (1.7) and (1.8).

The calculation of the irreversible magnetization curves can be carried out in the way described by Kes et al. [1], but only if an analytic expression for C_{66}, valid in the whole field region, is available. In order to obtain such an expression we tentatively assumed:

$$C'_{66} = \frac{H - H_{c_1}}{H_{c_2} - H_{c_1}} \frac{H_{c_2}}{H} C_{66} \qquad (3.3)$$

which, as is shown in fig. 3.16 by the circles, gives a reasonable fit near H_{c_1} as well as near H_{c_2}. Kes [23] used eq. (3.3) for the sample NO-0 and found an equally good agreement, using C_{66} as given in eq. (16).

Using eqs. (1.4), (1.6) and (3.3) and setting p_m proportional to $(H_{c_2} - B)$

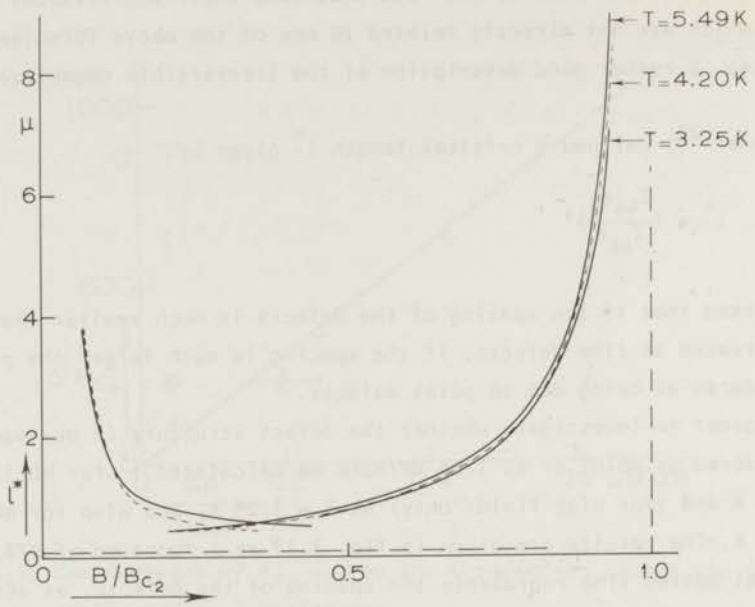

Fig. 3.17 *The parameter l^* versus B/B_{c_2} for the sample NO-320 (full lines) at T = 5.49 K and T = 3.25 K, and for NO-319 (dotted line) at T = 4.20 K. The horizontal dotted line represents the defect spacing in NO-320 and NO-319 as derived from the electron microscope pictures.*

in the whole field region [1,15,20,21,24]) eq. (1.7) reduces to:

$$J_c = \frac{P_v}{B} \approx \frac{H_{c_2} - B}{[H_{rev}(B) - H_{c_1}]^{\frac{1}{2}}} \tag{3.4}$$

Here the term $(C_{44}C_{11})^{-\frac{1}{2}}$ of eq. (1.7) has been neglected because C_{11} is much larger than C_{66} (see fig. 3.16). Neglecting the logarithm in eq. (1.8) this equation reduces to:

$$J_c \approx \frac{H_{rev}(B)}{[H_{rev}(B) - H_{c_1}]B^{\frac{1}{2}}} \tag{3.5}$$

Also from these formulae it is immediately clear that, if indeed both types of pinning are present, the line pinning becomes dominant near H_{c_2}.

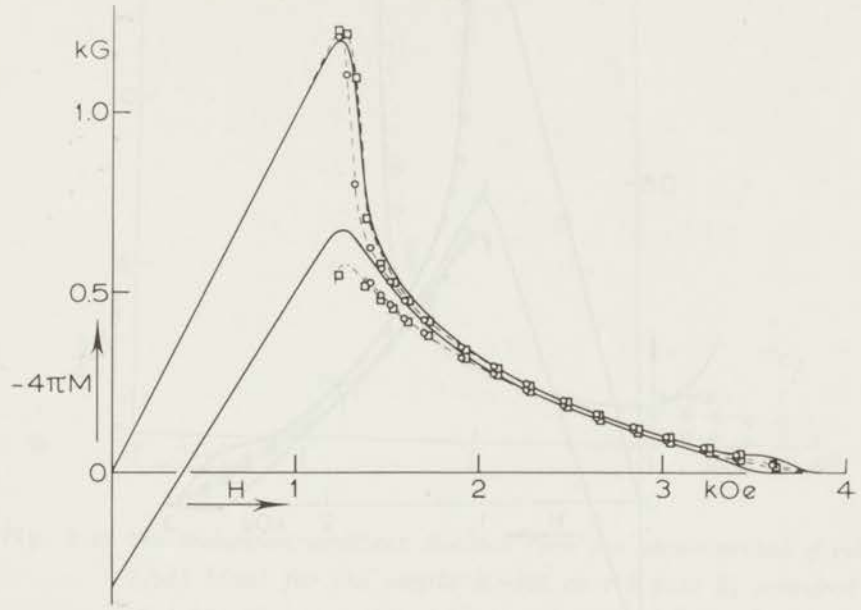

Fig. 3.18 *Calculated magnetization curve compared with the experimental one for NO-320 at T = 5.49 K. The adaptation is made at H = 1700 Oe.* □ *: Good and Kramer's formula for pinning due to line defects;* ○ *: Labusch's formulae for pinning due to point defects.*

In figs. 3.18 and 3.19 we plotted the experimental magnetization curves of the sample NO-320 at T = 5.49 K and of NO-319 at T = 4.20 K respectively, together with the curves derived from Labusch's formula for point pinning eq. (3.4) and for Good and Kramer's formula for line pinning (eq. 3.5). The adaptations were made at H = 1700 Oe (fig. 3.18) and at H = 2200 Oe (fig. 3.19). From these results it appears that in the lower field region none of the models describe the experimental curves exactly, although the differences do not seem to be very dramatic. In the higher field region up to the beginning of the peak effect both models fit the experimental curve.

For a more precise analysis we plotted $(\partial B/\partial x)$ as a function of the magnetic field in fig. 3.20 for NO-319 at T = 4.20 K. The points have been

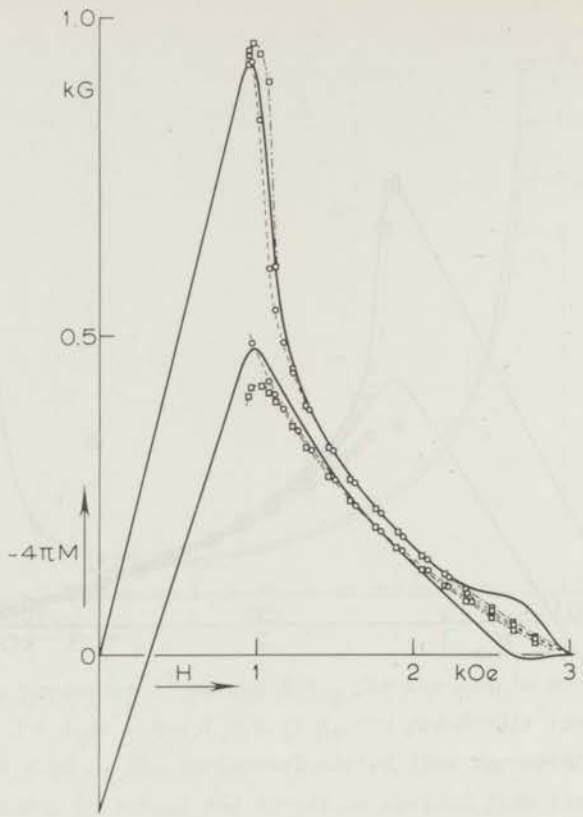

Fig. 3.19 *Calculated magnetization curve compared with the experimental one for NO-319 at T = 4.20 K. The adaptation is made at H = 2200 Oe.* □ *: Good and Kramer's formula for pinning due to line defects;* ○ *: Labusch's formula for pinning due to point defects.*

directly computed from eqs. (3.4) and (3.5). The adaptation was made at H = 2200 Oe. The experimental curve (full line) is obtained from the difference $4\pi\Delta M$ of the magnetization curve in increasing and decreasing field [1]). As can be seen in the higher field region the line pinning formula gives the best description. Close to H_{c_2} the deviation between the experimental curve and the calculated results is due to the peak effect, which is caused by a more effective pinning and therefore not reflected in the theoretical curves (see chapter 4).

We conclude that in the higher field region line pinning dominates, whereas at lower fields a combination of point and line pinning occurs.

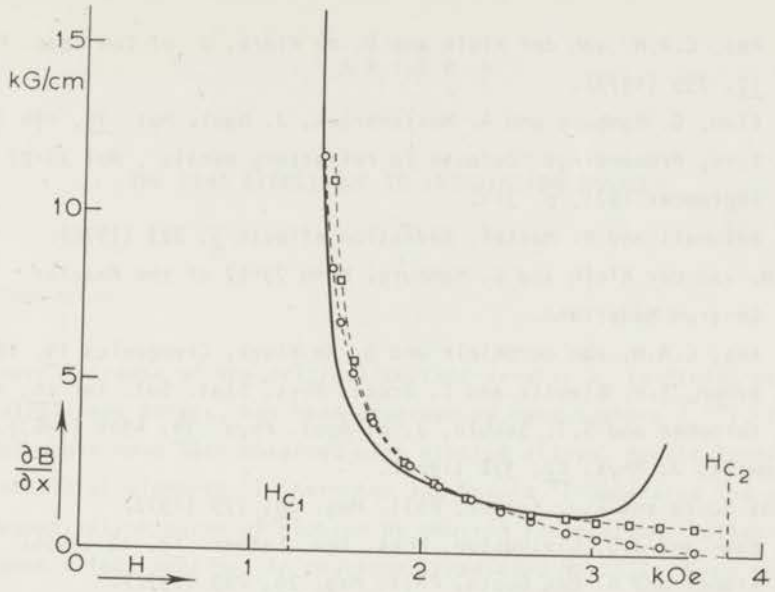

Fig. 3.20 *The induction gradient derived from the experimental curve (full line) for the sample NO-319 at T = 4.20 K, compared with the theoretical models.* □ *: line pinning model;* ○ *: point pinning model.*

References

1. P.H. Kes, C.A.M. van der Klein and D. de Klerk, J. of Low Temp. Phys. 10, 759 (1973).
2. J.D. Elen, G. Hamburg and A. Mastenbroek, J. Nucl. Mat. 39, 194 (1971).
3. B.L. Eyre, Proceedings "Defects in refractory metals", Mol 20-22 September 1971, p. 311.
4. J.L. Brimhall and B. Mastel, Radiation effects 3, 203 (1970).
5. C.A.M. van der Klein and G. Hamburg, Memo 73-02 of the Reactor Centrum Nederland.
6. P.H. Kes, C.A.M. van der Klein and D. de Klerk, Cryogenics 14, 168 (1974).
7. B.S. Brown, T.H. Blewitt and T. Scott, Phys. Stat. Sol. (a) 16, 105 (1973).
8. R.H. Kernohan and S.T. Sekula, J. of Appl. Phys. 38, 4904 (1967).
9. J. Lowell, J. Phys. C2, 372 (1969).
10. A. Das Gupta and E.J. Kramer, Phil. Mag. 26, 779 (1972).
11. C.P. Bean and J.D. Livingston, Phys. Rev. Letters 12, 14 (1964).
12. E.J. Kramer and A. Das Gupta, Phil. Mag. 26, 769 (1972).
13. Y.B. Kim, C.F. Hemstead and A.R. Strnad, Phys. Rev. Letters 9, 306 (1962).
14. B.B. Goodman, I.B.M. J. Res. Developm. 6, 63 (1962).
15. A.M. Campbell and J.E. Evetts, Adv. in Phys. 21, 199 (1972).
16. W.A. Fietz and W.W. Webb, Phys. Rev. 178, 657 (1969).
17. R. Labusch, Crystal Lattice Defects 1, 1 (1969).
18. R. Labusch, Phys. Stat. Sol. 19, 715 (1967); 36, 439 (1969).
19. J.A. Good and E.J. Kramer, Phil. Mag. 22, 329 (1970).
20. S.H. Goedemoed, P.H. Kes, F.Th.A. Jacobs and D. de Klerk, Physica 35 273 (1967).
21. A.M. Campbell, J.E. Evetts and D. Dew-Hughes, Phil. Mag. 18, 313 (1968).
22. E.J. Kramer, J. Appl. Phys. 44, 1360 (1973).
23. P.H. Kes, thesis, Leiden (1974).
24. H.C. Freyhardt, Phil. Mag. 23, 345 (1971).

CHAPTER 4

THE PEAK EFFECT DUE TO IRRADIATION DAMAGE

§4.1 *Introduction*

A sharp increase of the critical current density J_c in fields near H_{c_2}, the so-called peak effect, has been observed by many authors [1-16]. The most pronounced peaks have been obtained with niobium alloys, particularly if doped with interstitial elements [1]. Kernohan and Sekula [5] generated the peak effect in the magnetization curve of niobium by neutron irradiation. Keller et al. [6] found a peak effect near H_{c_2} in deuteron-irradiated Nb-25%Zr. For a more detailed review we refer to a paper by Campbell and Evetts [7].

In order to explain these effects several theories are proposed. Some authors [3], following the suggestion by Anderson and Kim [8], ascribed the peak effect to an increased flux lattice rigidity occurring near H_{c_2} due to mutual fluxoid interaction. But Pippard [9] pointed out that, on the contrary, due to a decrease of the lattice rigidity near H_{c_2}, flux vortices conform more readily to the crystal defect pattern. Indeed, Labusch [10] calculated that near H_{c_2} the shear modulus C_{66} of the flux lattice (see eq. 1.6) falls to zero proportionally to $(H_{c_2} - B)^2$. The Pippard calculations were somewhat extended by Campbell and Evetts [7] only for the case that pinning in the sample is due to line defects.

We observed a peak effect in the magnetization curve of niobium samples after irradiation with fast neutrons. Although the overall irreversibility due to the irradiation does not increase very much, a large peak effect occurs for an irradiated dose of 10^{20} n/cm^2 (see chapter 3).

§4.2 *Experimental results*

A description of the samples has been given in chapter 3. In the present chapter we pay special attention to the samples NO-318, NO-319 and NO-320. These samples were irradiated in the High Flux Reactor of the Reactor Centrum

Nederland, Petten, with fast neutron doses (equivalent fission spectrum) of 3.75×10^{18}, 3.65×10^{19} and 1.5×10^{20} n/cm^2 respectively (see table 3.1). After irradiation the samples were heat treated during a few minutes in an oxygen atmosphere at 400°C in order to remove surface effects.

The experimental set-up for measuring the dc magnetization curves has been described in chapters 2 and 3.

Figure 4.1 shows the magnetization curves in longitudinal fields at different temperatures for NO-320, in increasing and, partially, in decreasing

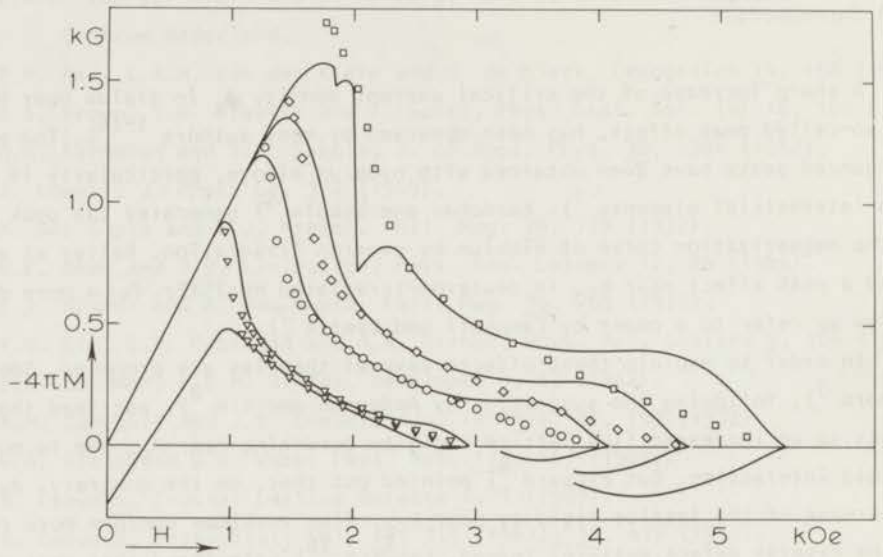

Fig. 4.1 *Magnetization curves in increasing and, partially, in decreasing fields, for NO-320 at different temperatures (fully drawn lines). The points represent theoretical results (see text)* ▽ : *T = 5.49 K;* ○ : *T = 4.20 K;* ◇ : *T = 3.25 K;* □ : *T = 1.77 K.*

field (fully drawn lines). The dots represent calculated values of the magnetization using the critical state model for flux pinning proposed by Goedemoed, Kes, Jacobs and De Klerk [11]) combined with the reversible state model proposed by Kes et al. [12]). From the irreversible curves, using eqs. 28a and b together with method (ii) given by Kes et al. (page 761) we obtained the reversible magnetization curve and also the pinning parameter γd, from which the irreversible curve can be calculated. The adaptation is made at a field value not too far below the field at which the peak effect shows up.

Subtracting these theoretical values from the experimental curves we obtain

the decrease of the average internal induction due to the peak effect. Fig. 4.2 shows the results for several temperatures versus reduced external field. This decrease ΔB is proportional to the increase of the induction gradient $\partial B/\partial x$ and so proportional to the increase of the critical current density. Under the assumption of the London-Bean model ($\partial B/\partial x$ is constant throughout the sample) $\Delta J_c = 4\Delta B/d$, in which d is the half-thickness of the sample. Therefore ΔB is comparable with the experimental results of Lubell and Kroeger [3]) and of Osborne [2]). The areas below the curves in fig. 4.2 are proportional to the extra pinning energy which corresponds to the peak effect.

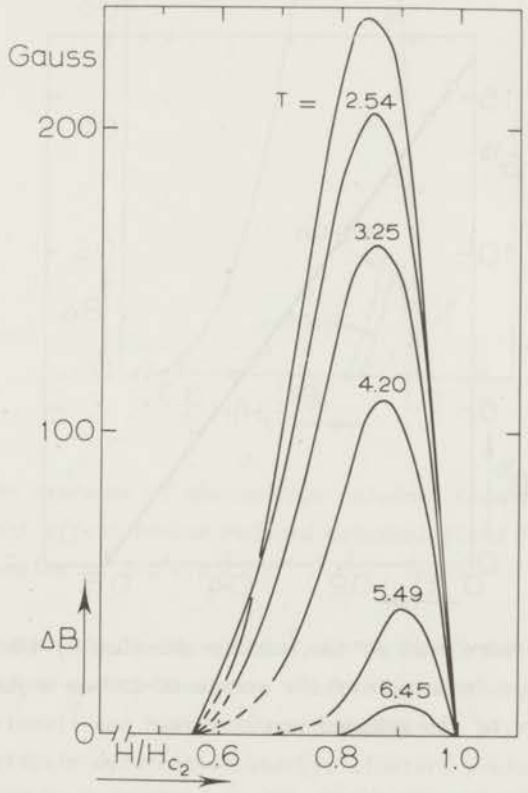

Fig. 4.2 *The decrease of the average internal induction due to the peak effect versus reduced external field at different temperatures for NO-320.*

As can also be seen from fig. 4.2 the reduced field value at which the maximum of the peak effect occurs ($h_p = H_p/H_{c2}$) as well as the height of the peak (ΔB_p) depend on temperature. In fig. 4.3 we can see that ΔB_p is

proportional to $(c_0 - t^2)^2$ in which $c_0 = 0.6$, which means that the peak effect vanishes in a region just below T_c. For NO-319 we found ΔB_p also proportional to $(c_0 - t^2)^2$, in which now $c_0 = 0.5$. Lubell and Kroeger [3] found $c_0 = 1$ as was predicted by Bychkov, Vereshchagin, Zuev, Karasik, Kurganov and Mal'tsev [13] for the rigid lattice model of Anderson and Kim [8]. From these results we believe that an explanation of the peak effect in terms of the (reduced) temperature will be rather difficult. It will come out in section 4.3 that the peak effect can be explained in terms of the average flux density at the peak field.

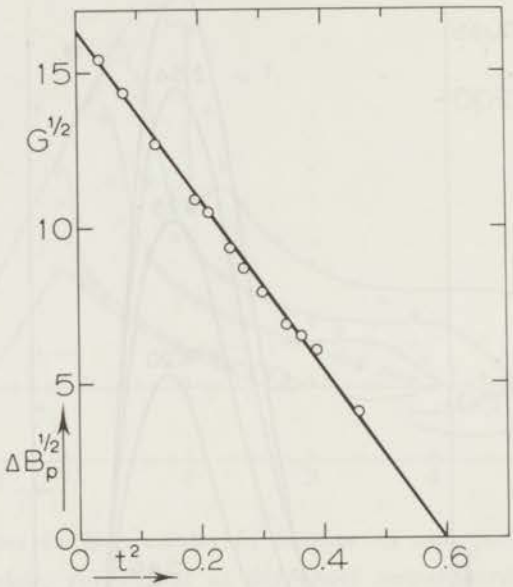

Fig. 4.3 *The square root of the maximum decrease of the internal average induction of the sample NO-320 as a function of the square of the reduced temperature.*

For NO-318 and NO-319 the field and temperature dependences of the peak effect have been derived in the same way as described above. Figure 4.4 shows ΔB versus reduced field for all three samples at $T = 4.2$ K. As can be seen from this figure there is a steep increase of the height of the peak effect for the highest dose. This sudden increase is due to the metallurgical character of the irradiation damage.

Information about the defect structure is given by electron microscope pictures shown in fig. 3.1 (c,d,e,f). As stated in chapter 3 the average cluster

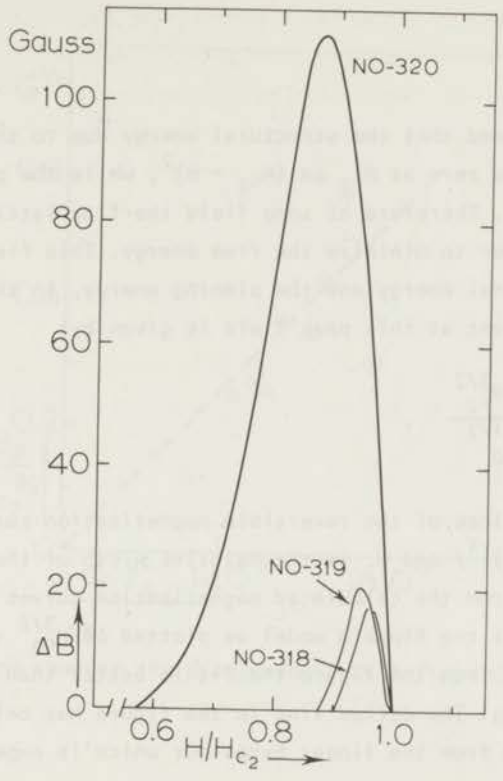

Fig. 4.4 *The decrease of the average internal induction due to the peak effect versus reduced external field for 3 different samples at T = 4.2 K.*

size in NO-318 and NO-319 is about 100 Å, while in NO-320 the size of the clusters is increased due to secondary clustering of the loops. It has been pointed out by Brimhall and Mastel [14]) and by Elen et al. [15]) that, in order to minimize the elastic deformation energy, clusters prefer to settle close to each other, forming "rafts". The size of these extended defects in NO-320 is of the order of 800 Å.

From these observations we can explain the difference in magnitude of the peak effect for the samples NO-318 and NO-319 on the one hand and for NO-320 on the other. As for the first ones the clusters are of a size smaller than the coherence length (ξ) and therefore they cannot pin the vortices very effectively, only the more extended rafts lead to an effective pinning and thus to a large peak effect.

In section 4.3 we will restrict ourselves to the sample NO-320.

§4.3 *Discussion*

Pippard [9]) assumed that the structural energy due to the rigidity of the flux lattice falls to zero at H_{c_2} as $(H_{c_2} - H)^2$, while the pinning energy falls to zero as $(H_{c_2} - H)$. Therefore at some field the flux lattice conforms to the pinning sites in order to minimize the free energy. This field can be found by equating the structural energy and the pinning energy. In this model the value of the critical current at this peak field is given by:

$$J_{c_p} \sim \frac{\alpha_1 \alpha_2^2 B_{c_2}^{3/2}}{60 \phi_0^{1/2}} \quad ,$$

in which α_1 is the slope of the reversible magnetization curve near H_{c_2} ($\alpha_1 = [1.16(2\kappa_2^2 - 1)]^{-1}$) and α_2 is the relative width of the peak $(H_{c_2} - H_p)/H_{c_2}$. We deduced α_1 from the calculated magnetization curves (see section 4.2).

In order to test the Pippard model we plotted $\Delta B/H_{c_2}^{3/2}$ versus $\alpha_1 \alpha_2^2$ (fig. 4.5). As can be seen from the figure the fit is better than found by Osborne [2]) but not too promising. The dotted line in the figure has only been given to stress the deviation from the linear behaviour which is expected from the model [†]).

One of the objections against Pippard's model is that it suggests that the peak effect should occur more often than is actually found [16]).

In order to overcome this difficulty a more precise analysis of the equilibrium between flux lattice rigidity on the one hand and the local pinning forces on the other is necessary. Campbell and Evetts [7]) pointed out that this can be done by calculating the pinning energy using the elastic constants of the flux lattice. They also mentioned that a sharp peak effect should only be expected in the case that the pinning is due to line defects parallel to the vortices, rather than if it is due to point defects. We can illustrate this by comparing the formulae for distortion of one vortex due to a point defect with that for distortion by a line defect.

According to Labusch [10]) the distortion due to a point defect, near H_{c_2} obeys the relation:

[†]) A slight improvement can be obtained if $(H_{c_2} - H_p)/H_{c_2}$ is replaced by $(H_{c_2} - B_p)/H_{c_2}$.

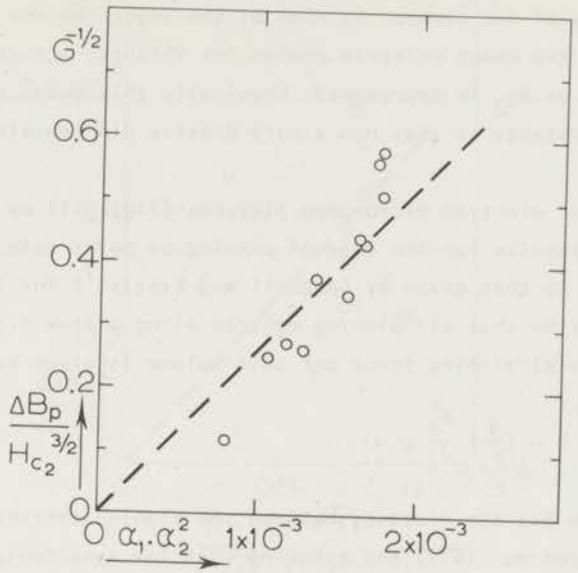

Fig. 4.5 *Graph showing the disagreement with Pippard's theory.*

$$u_0 = \frac{p_m^p}{4\pi^{\frac{1}{2}}} \left(\frac{B}{\phi_0}\right)^{\frac{1}{2}} \frac{1}{(C_{44}C_{66})^{\frac{1}{2}}} \qquad (4.1)$$

in which p_m^p is the maximum pinning force of one point defect, C_{44} is the elastic constant correlated to the local bending of a flux line and C_{66} is the shear modulus of the flux lattice (see eqs. 1.4 and 1.6). Since C_{44} is proportional to $hb(= HB/H_{c_2}^2)$, the shear modulus C_{66} to $(1 - b)^2$ and p_m to $(1 - b)$, the distortion does not vary much as H_{c_2} is reached. The pinning energy, which is proportional to $p_m u_0$ falls to zero at H_{c_2} as $(1 - b)$, in agreement with Pippard's assumption.

In the case of pinning by line defects parallel to the vortices the distortion, according to Good and Kramer [17]) obeys:

$$u_0 = \frac{5p_m^\ell}{16\pi C_{66}} \ln(r/a_0) \qquad (4.2)$$

in which p_m^{ℓ} is the pinning force per unit length of one line defect on one vortex, a_0 the flux lattice spacing ($= 1.07(\phi_0/B)^{\frac{1}{2}}$), and r is the distance to the fixed boundary of the sample. In view of the logarithm the results are not very sensitive to the exact criteria chosen for this cut-off distance. u_0 can become very large as H_{c_2} is approached. Physically this means that the pinning energy remains constant, so that now a more drastic pinning effect can be expected near H_{c_2}.

In view of our electron microscope pictures (fig. 3.1) we decided to check our experimental results for the case of pinning by point defects. Our derivation is analogous to that given by Campbell and Evetts [7]) for line defects. Making the assumption that all pinning centres along a flux line operate independently the total pinning force per unit volume is given by:

$$P_v = J_c \cdot B = \left(\frac{B}{\phi_0}\right) \frac{p_m^p}{d_n} , \qquad (4.3)$$

in which d_n is the average distance between the pinning centres along a vortex. Substituting p_m^p from eq. (4.1) and assuming that for synchronization of the flux lattice to the inhomogeneities pattern a distortion $u_0 = ka_0$ is required we derived:

$$J_{c_p} \sim \frac{3.5k\alpha_1^{\frac{1}{2}} H_{c_2}}{(1 + \alpha_1) d_n} (1 - b_p) ,$$

in which b_p is the average induction at the peak field divided by H_{c_2}. In fig. 4.6 we plotted $\Delta B/H_{c_2}^{3/2}$ versus $(1 - b_p)\alpha_1^{3/2}/(1 + \alpha_1)H_{c_2}^{\frac{1}{2}}$. As can be seen from the figure our results cannot be explained by this model. We have to conclude that the assumption of eq. (4.3) that the pinning centres along a flux line operate independently is too crude.

The electron microscope pictures (fig. 3.1e and f) show that the size of the extended point defects is of the same order of magnitude as their mutual spacing, which, in our sample, is comparable with the coherence length ξ. This makes it rather unlikely indeed that they actually operate as independent pinning centres. A better assumption seems to be that effectively a vortex is pinned over its whole length without interruptions, so that the distortion can be better described on the basis of line defects (eq. (4.2)) than of point defects (eq. (4.1)). In other words the distortion does not depend on the local bending parameter C_{44} any more, but on the shear modulus C_{66} only. The same idea has also been proposed very recently by Kramer [18]). The fact that his critical length l^* (see section 3.4.2c) increases strongly for H_a approaching H_{c_2} corroborates

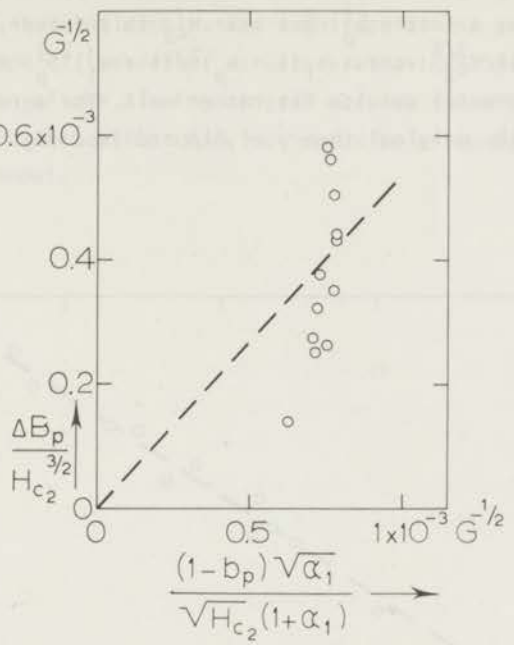

Fig. 4.6 *Graph showing the disagreement with the theory based on pinning due to point defects.*

the idea that the peak effect is due to line pinning. As stated in chapter 3 also the dc magnetization curve near H_{c_2} can be described better by a critical state model based on line pinning than by one based on point pinning, see fig. 3.20. The derivation based on pinning by line defects parallel to a vortex has been given by Campbell and Evetts [7] for high κ materials, but it can easily be generalized for all κ's.

Making the assumption that all vortices are pinned the total pinning force per unit volume is given by the number of flux lines per unit area times the pinning force per unit length of one line defect on one vortex, so:

$$P_v = \left(\frac{B}{\phi_0}\right) p_m^{\ell} \qquad (4.4)$$

Now the peak critical current is given by:

$$J_{c_p} \simeq \frac{2kH_{c_2}^{3/2}}{\ln(r/a_0)\phi_0^{\frac{1}{2}}} \cdot \frac{\alpha_1(1-b_p)^2}{(1+\alpha_1)^2 b_p^{\frac{1}{2}}} ,$$

which, apart from the coefficient, differs from the expression derived by Campbell and Evetts by a factor $b_p^{\frac{1}{2}}$. But near H_{c_2} this factor approaches 1. In fig. 4.7 we plotted $\Delta B/H_{c_2}^{3/2}$ versus $\alpha_1(1 - b_p)^2/(1 + \alpha_1)^2 b_p^{\frac{1}{2}}$. As can be seen from the figure our experimental results fit rather well. The agreement is obviously better than with the original theory of Pippard (see fig. 4.5).

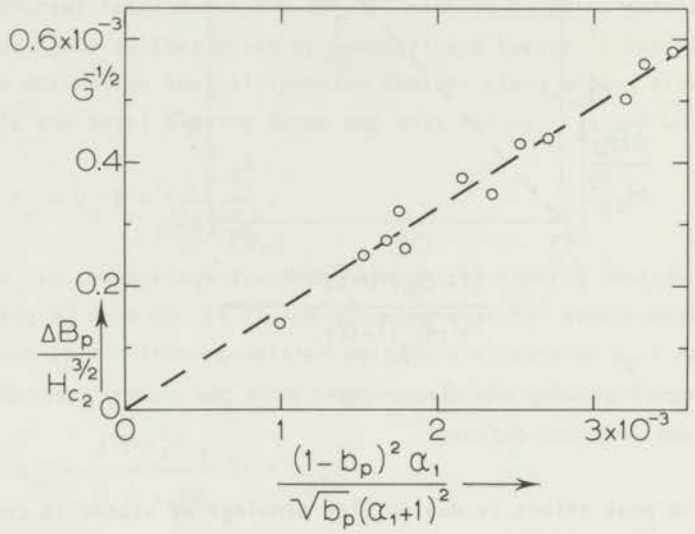

Fig. 4.7 *Graph showing the agreement with the theory based on pinning due to line defects.*

Setting for $J_{c_p} = 4\Delta B_p/d$ (see section 4.2) we derived from the slope of the dotted line in the figure:

$$\frac{k}{\ln(r/a_0)} = 5.6 \times 10^{-3} \quad .$$

With the assumption $r \approx 10a_0$ this corresponds very well with the value of k of the order of 0.01 mentioned by Campbell and Evetts. Nevertheless this leads to a distortion u_0 which seems rather small. But the assumption for eq. (4.4) was that all the vortices are pinned. If only a fraction is pinned, k will increase proportional to this fraction and the distortion increases as well. Therefore we think this theory explains the order of magnitude of the peak effect rather well.

In conclusion we can say that the general model given by Pippard is essentially correct, but too simple. The magnitude of the peak effect depends strongly on the type of the defect structure. The local pinning force as well as the distribution of the pinning centres must be taken into account. This may explain why the peak effect does not occur so often as should be expected from the Pippard model.

References

1. W. De Sorbo, Rev. Mod. Phys. 36, 90 (1964).
2. K.E. Osborne, Phil. Mag. 23, 1113 (1971).
3. M.S. Lubell and D.M. Kroeger, Physica 55, 394 (1971).
4. K. Tachikawa, Proceedings appl. Supercond. Conf. Annapolis, Maryland, p. 371 (1972).
5. R.H. Kernohan and S.T. Sekula, J. appl. Phys. 38, 4904 (1967).
6. E.L. Keller, H.T. Coffey, A. Petterson and S.H. Autler, Appl. Phys. Letters 9, 270 (1966).
7. A.M. Campbell and J.E. Evetts, Adv. Phys. 21, 199 (1972).
8. P.W. Anderson and Y.B. Kim, Rev. Mod. Phys. 36, 39 (1964).
9. A.B. Pippard, Phil. Mag. 19, 217 (1969).
10. R. Labusch, Phys. Stat. Sol. 32, 439 (1969).
11. S.H. Goedemoed, P.H. Kes, F.Th.A. Jacobs and D. de Klerk, Physica 35, 273 (1967).
12. P.H. Kes, C.A.M. van der Klein and D. de Klerk, J. of Low Temp. Phys. 10, 759 (1973).
13. Yu. Bychkov, V.G. Vereshchagin, M.T. Zuev, V.R. Karasik, G.B. Kurganov and V.A. Mal'tsev, Soviet Phys. JETP Lett. 9, 271 (1969).
14. J.L. Brimhall and D. Mastel, Radiation Effects 3, 203 (1970).
15. R.H. Kernohan and S.T. Sekula, J. appl. Phys. 38, 4904 (1967).
16. D. Dew-Hughes, Rep. Prog. Phys. 34, 821 (1971).
17. J.A. Good and E.J. Kramer, Phil. Mag. 22, 329 (1970).
18. E.J. Kramer, J. appl. Phys. 44, 1360 (1973).

CHAPTER 5

CALCULATIONS ON THE PERMEABILITY BASED ON THE LONDON-BEAN MODEL

§5.1 *Introduction*

In chapter 2 we described a series of experiments on the influence of physical impurities on the magnetic behaviour of superconducting niobium.

Material of high chemical purity was cold rolled and cut into rectangular samples of 30 x 3 x 0.15 mm. The dislocation density was varied by heat treatment at different temperatures. A gradual increase in reversibility with the heat treatment was observed for the magnetic moment; two different types of behaviour were found, however, for the susceptibility. For samples with a high dislocation density (larger than about 10^9 cm^{-2}) the whole variation of the susceptibility took place in the region between the upper critical field H_{c_2} and the nucleation field H_n (which proved to be noticeably higher than the field H_{c_3} introduced by Saint James and de Gennes [1]).† For samples with lower dislocation densities the variation of the susceptibility started already at the lower critical field H_{c_1}.

The aim of the present paper is to give models for both types of behaviour, and since they were observed in the most pronounced way for the samples heat treated at 1000°C (P_{1000}) and 1600°C (P_{1600}), we will restrict ourselves to the discussion of these samples, figs. 2.8 and 2.11 respectively.

Many experiments and calculations have been carried out in the past on the influence of varying magnetic fields on type-II superconductors. A detailed list of references is given in a survey article by Wipf [2]. In general, two approaches have been applied. Some investigators used large amplitudes [3-6], the field going up and down from a value somewhere between H_{c_1} and H_n to minus the same value. In other experiments [7-17] a constant field H was applied on which an alternating field of small amplitude H_0 was superimposed. The latter was also

---

†) Resonance investigations on one of our samples by P.L. Indovina (Istituto Superior di Sanita, Rome) corroborated our H_n values (private communication).

our approach. Both H and the alternating field were parallel to the sample; the field H could be adjusted at any value (H_a) between zero and well above H_n; the amplitude H_0 was varied between 0.72 and 9.52 Oe.

Our final results were presented in a diagram (fig. 2.13) in which the imaginary component of the susceptibility χ'' was plotted against the real part χ' (actually we plotted $4\pi\chi''$ against $-4\pi\chi'$). This is standard practice in investigations on paramagnetic relaxation, and we think that also in the case of type-II superconductors such diagrams are very useful because they give much sharper criteria for the validity of possible theoretical models than the usual plots of the a.c. losses against the amplitude of the alternating field (see also chapter 6).

For both our samples P_{1000} and P_{1600} it was found that the directly measured values of χ' and χ'' for different values of the steady field, H_a were, within the limits of the experimental accuracy, independent of the frequency of the alternating field, but strongly dependent on the amplitude. In the $4\pi\chi''$ vs. $-4\pi\chi'$ diagram, however, a universal curve was found for the sample P_{1000}, which was almost symmetrical with respect to the line $-4\pi\chi' = 0.5$ (see fig. 2.12). Totally different results were obtained with P_{1600}. Different curves were found for different amplitudes of the alternating field. The maxima were lower than in the case of P_{1000} and they were lower the smaller the amplitude. Moreover, the curves were strongly asymmetrical.

These results are shown again in fig. 5.1, but in a slightly modified way. Instead of plotting $4\pi\chi''$ against $-4\pi\chi'$ we plotted the permeability component μ'' ($= 4\pi\chi''$) as a function of μ' ($= 1 + 4\pi\chi'$). This was done because the formulae derived in the subsequent sections become simpler if they are expressed in terms of permeabilities. It only means that the left- and right-hand sides of the diagrams are reversed.

In view of the complete absence of any frequency dependence in our experiments it seems justified to discuss the results with the help of hysteresis models only, neglecting all relaxation effects.

In section 5.2 of this paper we will introduce and justify the different theoretical models used in our calculations, in section 5.3 the models will be treated mathematically, and in section 5.4 the results will be discussed.

§5.2 *The theoretical models*

5.2.1 *The influence of surface screening above H_{c_2}.* For the sample P_{1000} the whole variation of μ' and μ'' takes place between H_{c_2} and H_n. In this region

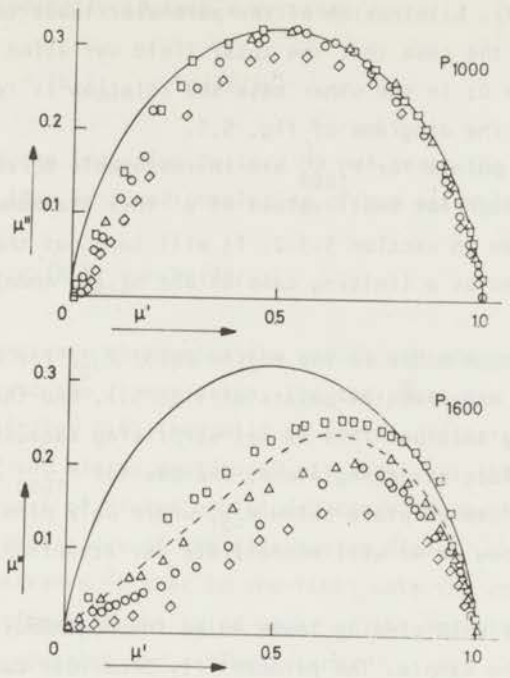

Fig. 5.1 *Diagram of the real and imaginary components of the magnetic permeability of the samples P_{1000} and P_{1600} for different amplitudes H_0 of the alternating field: □ , H_0 = 9.52 Oe; Δ , H_0 = 4.81 Oe; ○ , H_0 = 2.41 Oe; ◇ , H_0 = 0.72 Oe. Fully drawn curves: theoretical curve of sections 5.2.1 and 5.3.2; dotted line: theoretical curve of sections 5.2.2 and 5.3.3.*

the bulk of the sample is in the normal state, only a layer of the order of the coherence length ξ remaining superconducting [1]). Persisting currents may occur in this layer which screen off part of the variations of the external field from the core. The critical current density gives rise to a maximum difference ΔH between the internal induction and the external field.

If the total variation due to the alternating field is less than 2ΔH the induction inside the sample is constant over the whole cycle. If it is larger than 2ΔH we find a hysteresis loop in the shape of a parallelogram. The two cases are sketched in the right-hand part of fig. 5.4.

Hysteresis loops very similar to such parallelograms have actually been measured by Rollins and Silcox [12]).

Fourier analysis of the hysteresis loop leads to expressions for both μ' and μ'' as functions of only one dimensionless parameter (which is, of course,

directly related to ΔH). Elimination of the parameter leads to a relation between μ' and μ''. In the case that the total field variation is less than $2\Delta H$ we only find $\mu' = \mu'' = 0$; in the other case the relation is represented by the drawn line in each of the diagrams of fig. 5.1.

The experimental points for P_{1000} are in reasonable agreement with this theoretical curve, though for small values of μ' they are somewhat low.

Formulae are given in section 5.3.2. It will turn out that, in a way, this model may be considered as a limiting case of one of the models discussed later.

5.2.2 *The London-Bean model in the region below H_{c_2}.* For P_{1600} there is no agreement between the experimental points of fig. 5.1, and the theoretical curve of the foregoing section. This is not surprising because the theoretical curve is based on surface screening alone, whereas for P_{1600} a big part of the variation of μ' and μ'' takes place below H_{c_2}, where bulk pinning must play an important role. From now on we will concentrate our attention to the region below H_{c_2}.

The occurrence of bulk pinning leads to an inhomogeneous flux-density distribution inside the sample. The permeability behaviour can be derived in a straightforward way from the variations of the induction pattern, as caused by the variations of the external field.

The simplest model for the induction pattern available in the literature is the London-Bean model [3,4]. It neglects all irreversible surface effects and it assumes a constant flux-density gradient $\partial B/\partial x$ throughout the sample. So if the field is increased monotonically from zero to a value somewhere between H_{c_1} and H_{c_2} the flux density inside the sample falls linearly from the surface value $(B_s)_{max}$ to a value $(B_s)_{max} - d(\partial B/\partial x)$ at the centre, where d is the half-thickness of the sample. This is illustrated in fig. 5.5.

If thereupon the external field is decreased somewhat the surface induction decreases to a value B_s and the inside flux density increases linearly from the surface until it intersects the line originally belonging to $(B_s)_{max}$. From there on it further follows this line.

On further decrease of the external field this flux distribution behaviour persists in such a way that the intersection with the original $(B_s)_{max}$ line moves gradually towards the centre. When B_s reaches values below $(B_s)_{max} - 2d(\partial B/\partial x)$ the flux density increases all the way from the surface to the centre of the sample.

The detailed considerations will be given in section 5.3.3 together with the formulae. It turns out that two cases must be distinguished. If the external

field varies periodically in such a way that

$$(B_s)_{max} - (B_s)_{min} < 2d(\partial B/\partial x)$$

the variations in the induction pattern do not reach the centre of the sample and a hysteresis loop is found consisting of two parabolas. In the case

$$(B_s)_{max} - (B_s)_{min} > 2d(\partial B/\partial x)$$

the variations penetrate throughout the sample and the hysteresis loop consists of two parabolas and two linear parts. The two cases are illustrated in the right-hand half of fig. 5.6. They will be further referred to as the cases of "small amplitude" and "large amplitude". It turns out that for samples with weak pinning the case of "large amplitude" cannot be neglected, not even for relatively small amplitudes of the alternating field.

London demonstrated [3]) that in the first case the energy losses in the sample are proportional to the third power of the amplitude; in the second they consist of a constant and a linear term.

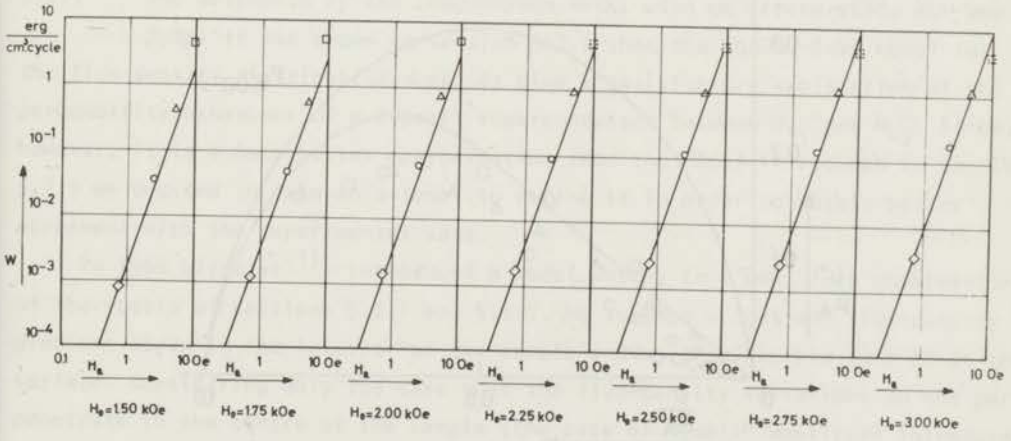

Fig. 5.2 *Energy losses vs. the amplitude H_0 of the alternating field for different values of the external field for the sample P_{1600}. The lines represent third powers of H_0. □, H_0 = 9.52 Oe; △, H_0 = 4.81 Oe; ○, H_0 = 2.41 Oe; ◇, H_0 = 0.72 Oe.*

Figure 5.2 shows logarithmic diagrams of the energy losses (in erg·cm^{-3}·cycle^{-1}) vs. the amplitude for the sample P_{1600}, as derived from the experimental μ'' data for a number of values of the external field. The fully drawn points represent the cases of "small" amplitude, the dotted ones those of "large" amplitude (this will be further elucidated later). The lines in the figure are third powers of the amplitude; each line has been drawn through the lowest experimental point. It turns out that for the fully drawn points the H_0^3 law is approximately fulfilled; in fact, the power is somewhat higher, about 3.3. The dotted points are lower, as should be expected.

As a first attempt we decided to neglect the difference between the powers 3 and 3.3 and to assume the London-Bean model as correct. Fourier analysis of the hysteresis loops (section 5.3.3) demonstrates that it is impossible to express μ' and μ'' as functions of only one dimensionless parameter. It is possible to do so, however, for the quantities μ'/μ_A and μ''/μ_A, where μ_A is the slope of the reversible Abrikosov curve $(\partial B/\partial H)_A$, which is a function of the steady external field H only. The dimensionless parameter is directly related to $\partial B/\partial x$. The relation between μ'/μ_A and μ''/μ_A is represented by the lower line of fig. 5.3 and for the special case $\mu_A = 1$ by the dotted line of fig. 5.1.

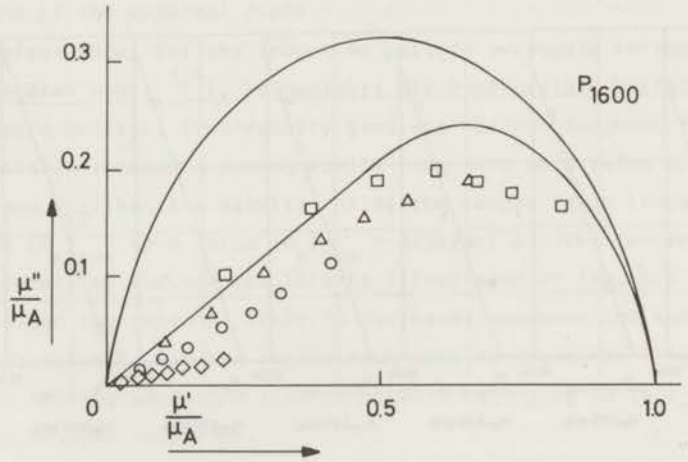

Fig. 5.3 *Permeability diagram for P_{1600} showing μ''/μ_A vs. μ'/μ_A for the same values H_a of the external field and the same amplitudes H_0 of the alternating field as in fig. 5.2. For each H_0 the point closest to the origin represents the smallest value of H_a. The curves represent the cases of sections 5.2.1 and 5.2.2.*

The linear part refers to "small" amplitude, the curved part to "large" amplitude.

For fig. 5.3 we have read μ' and μ'' from the curves of fig. 2.11 at the external field values of fig. 5.2 (all below H_{c_2}). For each point they were divided by the appropriate value of μ_A, which was obtained by graphical differentiation of an Abrikosov curve that was constructed with the help of the experimental magnetization curve of figs. 2.4 and 2.11 (Some values for μ_A are given at the bottom of fig. 5.13.) This brings the points closer to the origin than in fig. 5.1.

It follows that, after this procedure, the great majority of the points falls below the theoretical curve instead of on it. This means that the London-Bean model does not account in the proper way for the amplitude dependence found in our experiments. So the fact that the ac losses are in reasonable agreement with this model apparently does not mean that it gives a satisfactory description of the permeability behaviour as a whole.

On the other hand it is clear that the London-Bean curve is in better agreement with the experimental data than the upper curve, which was derived for the region above H_{c_2}. It is asymmetric and it has the correct general shape.

5.2.3 *The extension of the London-Bean model with an irreversible surface jump.* It was shown in section 5.2.2 that the London-Bean model for the flux-density distribution does not give a satisfactory explanation of the permeability behaviour of a type-II superconductor between H_{c_1} and H_{c_2}. Since, however, it is a much better approximation than the model introduced in section 5.2.1 we decided to make an attempt to refine it in order to obtain better agreement with the experimental data.

In 1966 Ullmaier [11]) introduced a model which, in a way, is a combination of the models of sections 5.2.1 and 5.2.2. He assumed a constant flux-density gradient $\partial B/\partial x$ in the interior of the sample and an irreversible jump ΔH at the surface. Considering only the case that the flux-density variations do not perpenetrate to the centre of the sample (the case of "small" amplitude introduced in section 5.2.2) he derived that the alternating field losses are proportional to $(H_0 - \Delta H)^3$. This results into a logarithmic diagram of the losses against the amplitude which is steeper than H_0^3. (Notice that our definition of ΔH is a factor two different from Ullmaier's.)

Wipf [2]) gave a thorough discussion of Ullmaier's model. He made an analysis of nearly 20 different investigations on niobium, by many different authors, and found that all their points fell inside a (not too narrow) band of a

logarithmic diagram. The slope of the band was larger than three. This led him to the conclusion that this model gives the correct description.

Sekula and Barrett [18]) demonstrated that the alternating field losses in Ullmaier's model are not proportional to $(H_0 - \Delta H)^3$ but to $(H_0 - \Delta H)^2(H_0 + 2\Delta H)$ (see also section 5.3.4). Also for this expression, however, the loss curve in a logarithmic diagram is steeper than H_0^3, though the difference in slope is smaller.

In fig. 5.2 we expressed our losses in erg/cm^3 · cycle. Wipf used J/cm^2 of the surface of the sample per cycle (which is meaningful in the case of "small" amplitude). If we reduce our values to his units it appears that they are a factor 100 left of his data band. This is probably not too surprising because Wipf only considered cases in which the external field was varied from a high positive value through zero to the opposite value (the remarkable point is that for samples with really strong pinning this may still be the case of "small" amplitude), whereas in our experiments a small alternating field was superimposed on a large steady field (see section 5.1).

Since in our diagram of fig. 5.2 the losses were somewhat steeper than H_0^3 we thought that the introduction of an irreversible surface jump ΔH into the London-Bean model might lead to better agreement between the theory and the experimental data for P_{1600}.

If in this model the external field is increased from zero to a value H_{max} the induction at the surface of the sample reaches a value $(B_s)_{max}$, and in the interior it decreases linearly until the value $(B_s)_{max} - d(\partial B/\partial x)$ at the centre. If, now, the field is decreased nothing happens to the internal flux pattern until the value $H_{max} - 2\Delta H$ is reached. On further decrease of the external field the flux pattern behaves in exactly the same way as in the pure London-Bean model, described in section 5.2.2. As long as the surface induction is larger than $(B_s)_{max} - 2d(\partial B/\partial x)$ the flux density first increases from the surface and then decreases; for B_s smaller than $(B_s)_{max} - 2d(\partial B/\partial x)$ it increases all the way from the surface to the centre.

Now we must distinguish three cases for the hysteresis loop. If the total variation due to the alternating field is less than $2\Delta H$ the induction pattern inside the sample is constant over the whole cycle. If it is larger than $2\Delta H$ but still so small that the variations of the induction pattern do not reach the centre of the sample a hysteresis loop is observed which consists of two horizontal lines and two parabolas. If the total variation of the external field is so large that the variations of the induction pattern do reach the centre of the sample the hysteresis loop consists of two horizontal lines, two parabolas,

and two parallel straight lines with finite slope. The three cases are illustrated in the right-hand part of fig. 5.8.

Fourier analysis of the hysteresis loops shows that in the first case we only obtain the point $\mu' = \mu'' = 0$ for the permeability. In the other cases we can derive expressions for μ'/μ_A and μ''/μ_A as functions of two dimensionless parameters, one of which is related to ΔH and the other to $\partial B/\partial x$. For the details we refer to section 5.3.4.

If the two parameters take all possible values it turns out that any μ', μ'' combination in fig. 5.3 can occur *between the two drawn curves*, and therefore between the theoretical curves of sections 5.2.1 and 5.2.2. Since the great majority of the experimental points of fig. 5.3 is below the lower curve it follows that the extension of the London-Bean model with an irreversible surface jump does not explain our experiments with the sample P_{1600}.

Of course this does not mean that no samples could be found for which the model would apply; it only means that it has no general validity, as was claimed by Wipf.

In a way we can even think that the sample P_{1000}, for which the points near the origin of fig. 5.1 are somewhat low, obeys this model. We will come back to this point later.

5.2.4 *The extension of the London-Bean model with a surface layer without pinning.* As was shown in section 5.2.3 the extension of the London-Bean model with an irreversible surface jump ΔH does not explain the permeability behaviour of our sample P_{1600}. The correction to the pure London-Bean model goes in the wrong direction.

For this reason we thought that a correction in the opposite sense might lead to a more satisfactory description. So instead of introducing a surface barrier ΔH we assumed a surface layer in which the pinning effect is weaker than in the core of the sample. The simplest (and also the crudest) possibility is that $\partial B/\partial x$ is completely zero in this layer and constant in the remainder of the volume.

The physical background of this model is not directly clear. It appears that the thickness of the surface layer is not of the order of the coherence length; it is a noticeable fraction δ of the half-thickness d of the sample. The model should be considered as a first-order approximation of the case that $\partial B/\partial x$ is not constant throughout the sample. We come back to this point in section 5.4 and also in chapter 6.

In this model the flux density in the surface layer is equal to the surface

induction B_s. In the core the pattern is similar to that of the pure London-Bean model of section 5.2.2. This means that as long as the variations in the induction pattern do not reach the centre of the sample ("small amplitude") the ac losses are the same as in the London-Bean model. No work is done against any pinning forces in the surface layer, and in the core the energy dissipation is the same as in the London-Bean model. This means that, as in section 5.2.2, we neglect the difference between H_0^3 and $H_0^{3.3}$.

The induction patterns are represented in fig. 5.9. If the external field is increased monotonically from zero to H_{max} the flux density in the surface layer becomes equal to $(B_s)_{max}$, and in the core it falls linearly to the value $(B_s)_{max} - (1 - \delta)d(\partial B/\partial x)$ at the centre.

If thereupon the external field is decreased somewhat the induction in the surface layer decreases to a value B_s and the flux density in the core increases linearly from this value until it intersects the line originally belonging to $(B_s)_{max}$. From there on it further follows this line.

This pattern is maintained until the flux density in the surface layer reaches values below $(B_s)_{max} - 2(1 - \delta)d(\partial B/\partial x)$. From there on the induction in the core increases all the way to the centre of the sample.

The detailed considerations will be given in section 5.3.5. For the hysteresis loop we must distinguish two cases again. If the external field varies periodically in such a way that

$$(B_s)_{max} - (B_s)_{min} < 2(1 - \delta)d(\partial B/\partial x)$$

the variations of the induction pattern do not reach the centre of the sample. This must be considered now as the case of "small" amplitude. The hysteresis loop consists of two parabolas. In the case

$$(B_s)_{max} - (B_s)_{min} > 2(1 - \delta)d(\partial B/\partial x)$$

which is now the case of "large" amplitude, the variations are observed throughout the sample and the hysteresis loop consists of two parabolas and two linear parts.

The two cases are illustrated in the right-hand part of fig. 5.10. The difference with fig. 5.6 (the case of the pure London-Bean model of section 5.2.2) is that there the parabolas started with horizontal tangents, whereas here they start with finite slopes.

Fourier analysis of the hysteresis loops yields expressions for μ'/μ_A and

μ''/μ_A as functions of two dimensionless parameters. One of them is the fraction δ of the thickness of the sample with zero pinning (see above); the other is directly related to $\partial B/\partial x$ in the core. This is further explained in section 5.3.5, where the formulae are derived.

If the two parameters take all the possible values it appears that any μ', μ'' combination in fig. 5.3 can occur *below the lower theoretical curve*. Since all the experimental points for P_{1600}, with only few exceptions, are in this region we believe that for this sample the extension of the London-Bean model with a surface layer without pinning is a better approximation of the true flux pattern than the extension with an irreversible surface jump as discussed by Ullmaier [11]) and Wipf [2]).

The detailed numerical discussion of our experimental results will be given in section 5.4.2.

§5.3 *Derivation of the formulae*

5.3.1 *Introduction.* If the field H goes up and down periodically between H_{max} and H_{min} we can introduce the steady component

$$H_a = \tfrac{1}{2}(H_{max} + H_{min})$$

and the amplitude of the alternating component

$$H_0 = \tfrac{1}{2}(H_{max} - H_{min})$$

We only consider the case $H_0 \ll H_a$.

If the total field is

$$H = H_a + H_0 \cos \omega t \tag{5.1}$$

the measured induction, henceforth referred to as $\overline{B}$, can be developed into a Fourier series:

$$\overline{B} = \overline{B}_0 + \sum_n \mu_n' H_0 \cos n\omega t + \sum_n \mu_n'' H_0 \sin n\omega t \tag{5.2}$$

Here, $\mu_1' = 1 + 4\pi\chi'$ and $\mu_1'' = 4\pi\chi''$ are the permeability components as determined in the experiment. The indices will further be omitted. So μ' and μ'' follow from

$$\pi H_0 \mu' = \int_0^{2\pi/\omega} \omega \overline{B} \cos \omega t \, dt \qquad (5.3a)$$

$$\pi H_0 \mu'' = \int_0^{2\pi/\omega} \omega \overline{B} \sin \omega t \, dt \qquad (5.3b)$$

The alternating field losses per unit volume and per cycle are given by

$$W = \frac{1}{4\pi} \oint H d\overline{B} = \tfrac{1}{4} H_0^2 \mu'' \qquad (5.4)$$

In view of our experimental conditions we always consider, in our derivations, the case of a flat sheet of superconducting material parallel to the field. The thickness of the sheet, 2d, is supposed to be much smaller than the length and width of the sample, so that demagnetizing effects may be neglected. The ac losses per unit area of the sample (which are considered by most authors) are in this case equal to

$$W_s = \tfrac{1}{4} H_0^2 d\mu''$$

5.3.2 *The influence of surface screening on the permeability.* This is the case introduced in section 5.2.1, where only surface screening occurs (no bulk pinning).

If the external field is increased from zero to a value H_{max} between H_{c_2} and H_n the induction inside the sample reaches a value B_{max} (homogeneous over the volume) which is lower than H_{max}:

$$B_{max} = H_{max} - \Delta H$$

where ΔH is caused by the critical surface current J_{c_s}, which per unit length is given by

$$\Delta H = 4\pi J_{c_s}$$

If the external field decreases, the screening current decreases, it reverses sign when $H = B_{max}$, and it reaches the value $-J_{c_s}$ when

$$H = B_{max} - \Delta H = H_{max} - 2\Delta H$$

Over this field interval B inside the sample is constant and equal to B_{max}.

On further decrease of the field to a value H_{min} the surface current density remains equal to J_{c_s}, so that from now on

$$B = H + \Delta H$$

If after this the field is increased again B remains constant and equal to B_{min} until $H = H_{min} + 2\Delta H$. After this B increases again according to

$$B = H - \Delta H$$

Now, if H_{max} is small as compared to $H_n - H_{c_2}$ we may consider ΔH as constant between H_{max} and H_{min}. This assumption is certainly justified in our experiments where H_0 is less than 10 Oe.

In the further calculations we must consider two cases:

$$H_{max} - H_{min} = 2H_0 < 2\Delta H$$

$$H_{max} - H_{min} = 2H_0 > 2\Delta H$$

If we introduce a parameter

$$\eta = \Delta H/H_0 \tag{5.5}$$

these cases are $\eta > 1$ and $\eta < 1$.

In the case $\eta > 1$ the induction inside the sample is constant during the whole cycle of the alternating field:

$$B = H_{max} - \eta H_0 \tag{5.6}$$

In the case $\eta < 1$ the induction in decreasing field is

$$H_{max} > H > H_{max} - 2\eta H_0: \quad B = H_{max} - \eta H_0 \tag{5.7a}$$

$$H_{max} - 2\eta H_0 > H > H_{min}: \quad B = H + \eta H_0 \tag{5.7b}$$

and in increasing field

$$H_{min} < H < H_{min} + 2\eta H_0: \quad B = H_{min} + \eta H_0 \tag{5.7c}$$

$$H_{min} + 2\eta H_0 < H < H_{max}: \quad B = H - \eta H_0 \tag{5.7d}$$

So η is the fraction of the alternating field over which B is constant. It is the dimensionless parameter referred to in section 5.2.1. The cases $\eta > 1$ and $\eta < 1$ are illustrated in the upper and lower halves of fig. 5.4.

Making use of these expressions we can compute μ' and μ'' using (5.3a), (5.3b) and (5.1). The case $\eta > 1$ leads to

$$\mu' = 0 \tag{5.8a}$$

$$\mu'' = 0 \tag{5.8b}$$

which is represented by the origin of the $\mu''(\mu')$ diagram alone. In the case $\eta < 1$ the Fourier integrals consist each of four intervals. The first two are interconnected at $H = H_{max} - 2\eta H_0$, corresponding to a time t_A which is given by

$$\cos \omega t_A = 1 - 2\eta$$

The permeability components in this case are equal to

$$\pi\mu' = \pi - 2(2\eta - 1)\sqrt{\eta(1 - \eta)} - \arccos(1 - 2\eta) \tag{5.9a}$$

$$\pi\mu'' = 4\eta(1 - \eta) \tag{5.9b}$$

This result is represented by the fully drawn lines in fig. 5.1.

The alternating current losses per unit volume, in the case $\eta > 1$, are given by

$$W = \tfrac{1}{4} H_0^2 \mu'' = 0 \tag{5.10}$$

In the case $\eta < 1$ they are equal to

$$W = \frac{H_0^2}{\pi} \cdot \eta(1 - \eta) = \frac{\Delta H}{\pi} (H_0 - \Delta H) \tag{5.11}$$

hence linear with the amplitude.

Formally we can also consider a model in which there is surface screening

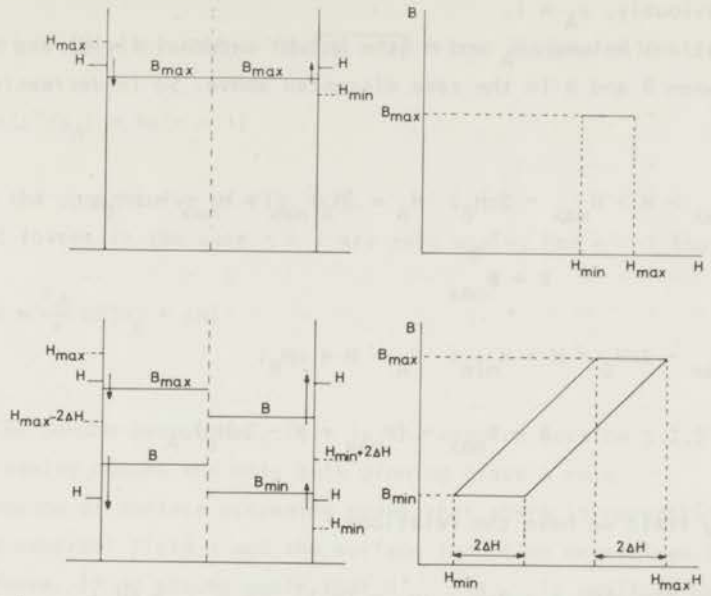

Fig. 5.4 *Induction patterns and hysteresis loops in the case when the magnetic behaviour is determined by surface screening only (sections 5.2.1 and 5.3.2). Upper part, $\eta > 1$; lower part, $\eta < 1$. The left-hand parts of the induction patterns refer to decreasing field and the right-hand parts to increasing field, as indicated by the arrows.*

and no bulk pinning in the region between H_{c_1} and H_{c_2}. The model corresponds to the somewhat hypothetic case of a pure Abrikosov superconductor with surface contamination. In that case we have a reversible surface jump which is determined by the Abrikosov curve, on which the irreversible jump ΔH is superimposed. It appears that this is a limiting case of the London-Bean model with ΔH extension discussed in section 5.3.4.

The case can be treated most easily by introducing a field H_A, the "Abrikosov field" which is in reversible equilibrium with the induction inside the sample. If the field variations are small as compared to $H_{c_2} - H_{c_1}$ we may consider μ_A, the slope of the Abrikosov curve $(\partial B/\partial H)_A$ (introduced in section 5.2.2), as a constant. In that case we have the relations

$$B_{max} - B = \mu_A[(H_A)_{max} - H_A] \tag{5.12a}$$

$$B - B_{min} = \mu_A[H_A - (H_A)_{min}] \tag{5.12b}$$

Above H_{c_2}, obviously, $\mu_A = 1$.

The relations between H_A and H (the actual external field) are the same as those between B and H in the case discussed above. So in decreasing field we obtain

$$H_{max} > H > H_{max} - 2\eta H_0: \quad H_A = (H_A)_{max} = H_{max} - \eta H_0;$$

$$B = B_{max} \tag{5.13a}$$

$$H_{max} - 2\eta H_0 > H > H_{min}: \quad H_A = H + \eta H_0;$$

$$B = B_{max} - (H_{max} - H - 2\eta H_0)\mu_A \tag{5.13b}$$

In increasing field we have the relations

$$H_{min} < H < H_{min} + 2\eta H_0: \quad H_A = (H_A)_{min} = H_{min} + \eta H_0;$$

$$B = B_{min} \tag{5.13c}$$

$$H_{min} + 2\eta H_0 < H < H_{max}: \quad H_A = H - \eta H_0;$$

$$B = B_{min} + (H - H_{min} - 2\eta H_0)\mu_A \tag{5.13d}$$

Here

$$B_{max} - B_{min} = (H_{max} - H_{min} - 2\eta H_0)\mu_A \tag{5.14}$$

In the case $\eta > 1$ the induction inside the sample is constant over the whole cycle of the alternating field. In the case $\eta < 1$ we have a hysteresis loop in the shape of a parallelogram, but the difference with fig. 5.4 is that the sides with finite slope are a factor μ_A steeper now.

In the case $\eta > 1$ Fourier analysis leads again to the relations

$$\mu' = 0 \tag{5.15a}$$

$$\mu'' = 0 \tag{5.15b}$$

In the case $\eta < 1$ (5.9a) and (5.9b) are replaced by

$$\pi(\mu'/\mu_A) = \pi - 2(2\eta - 1)\sqrt{\eta(1 - \eta)} - \arccos(1 - 2\eta) \qquad (5.16a)$$

$$\pi(\mu''/\mu_A) = 4\eta(\eta - 1) \qquad (5.16b)$$

leading to the upper curve of fig. 5.3.

The ac losses in the case $\eta > 1$ are zero again. For $\eta < 1$ they are

$$W = \frac{\mu_A}{\pi} \Delta H(H_0 - \Delta H) \qquad (5.17)$$

5.3.3 *The London-Bean model.* This is the case of section 5.2.2 where no surface screening occurs and only bulk pinning plays a role.

The absence of surface screening means that there is reversible equilibrium between the external field H and the surface induction determined by the Abrikosov curve. If we assume again that $H_{max} - H_{min}$ is small as compared to $H_{c2} - H_{c1}$, we may consider μ_A, the slope of the Abrikosov curve, as a constant. This leads to the relations

$$(B_s)_{max} - B_s = \mu_A(H_{max} - H) \qquad (5.18a)$$

$$B_s - (B_s)_{min} = \mu_A(H - H_{min}) \qquad (5.18b)$$

which are simplifications of (5.12a) and (5.12b). It should be noticed that the factor μ_A was neglected in the original papers of London [3]) and Bean [4]). In this respect our treatment is more complete.

The induction pattern inside the sample is completely determined by the bulk pinning. Under our assumption that $H_{max} - H_{min}$ is much smaller than $H_{c2} - H_{c1}$ we may consider $\partial B/\partial x$, not only as a constant throughout the sample (as required by the London-Bean model, see section 5.2.2), but also as independent of H. This leads to the induction patterns sketched in fig. 5.5.

If the external field is increased from zero to H_{max} the induction falls linearly from $(B_s)_{max}$ at the surface to $(B_s)_{max} - d(\partial B/\partial x)$ at the centre of the sample. If the external field is decreased to a value H the surface inductance B_s adapts itself to the Abrikosov value, and B inside the sample increases as a function of the distance from the surface until it intersects the line which originally belonged to $(B_s)_{max}$; from there on it further follows this line. For B_s smaller than $(B_s)_{max} - 2d(\partial B/\partial x)$ the flux density increases

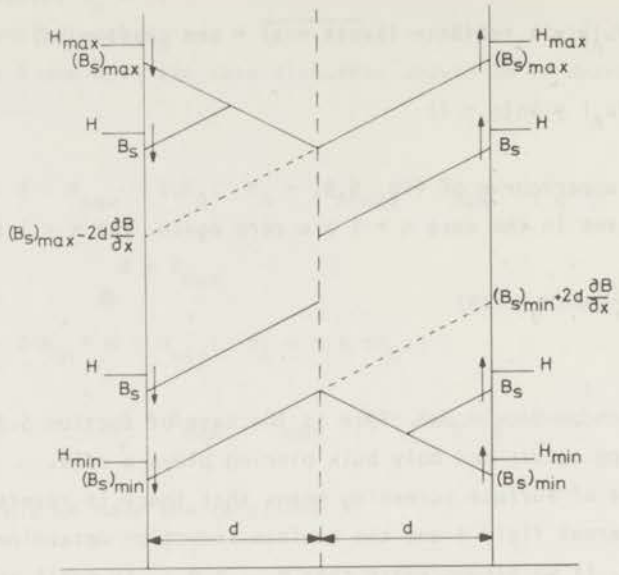

Fig. 5.5 *Induction patterns for the London-Bean model (sections 5.2.2 and 5.3.3) for various values of the external field. The left-hand half of the figure refers to decreasing field and the right-hand half to increasing field, as indicated by the arrows. The same values of the external field were chosen for both halves of the figure.*

linearly from the surface to the centre.

If B_s increases again from $(B_s)_{min}$ we have first a region between $(B_s)_{min}$ and $(B_s)_{min} + 2d(\partial B/\partial x)$ where B inside the sample first decreases and then increases with distance. In the region between $(B_s)_{min} + 2d(\partial B/\partial x)$ and $(B_s)_{max}$ the flux density decreases linearly until the centre of the sample.

For the computation of the average flux density $\overline{B}$ (the quantity determined in the experiment) from the induction pattern we must distinguish two cases:

$$(B_s)_{max} - (B_s)_{min} < 2d\left(\frac{\partial B}{\partial x}\right)$$

$$(B_s)_{max} - (B_s)_{min} > 2d\left(\frac{\partial B}{\partial x}\right)$$

which, according to (5.18a) and (5.18b) are equivalent to

$$H_{max} - H_{min} < \frac{2d}{\mu_A}\left(\frac{\partial B}{\partial x}\right)$$

$$H_{max} - H_{min} > \frac{2d}{\mu_A}\left(\frac{\partial B}{\partial x}\right)$$

If we introduce a parameter

$$\zeta = \frac{d}{\mu_A H_0}\left(\frac{\partial B}{\partial x}\right) \tag{5.19}$$

the cases are $\zeta > 1$ and $\zeta < 1$.

In the case $\zeta > 1$ the variations of the external field only influence the induction pattern in an outer layer of the sample. In decreasing field the relation between the measured induction $\overline{B}$ and the surface induction B_s can be easily calculated from the sum of the areas of two trapezoids; in increasing field it follows from the sum of the areas of three trapezoids (see fig. 5.5 and the upper half of fig. 5.6). (This is only true if we consider a flat sheet of superconducting material, as was assumed in section 5.3.1; in the case of a cylindrical sample the calculalions become somewhat more complicated.)

In the case $\zeta < 1$ the variations of the external field influence the flux distribution throughout the sample. In decreasing field the relation between $\overline{B}$ and B_s can be calculated: for the region $H_{max} > H > H_{max} - 2\zeta H_0$, from the

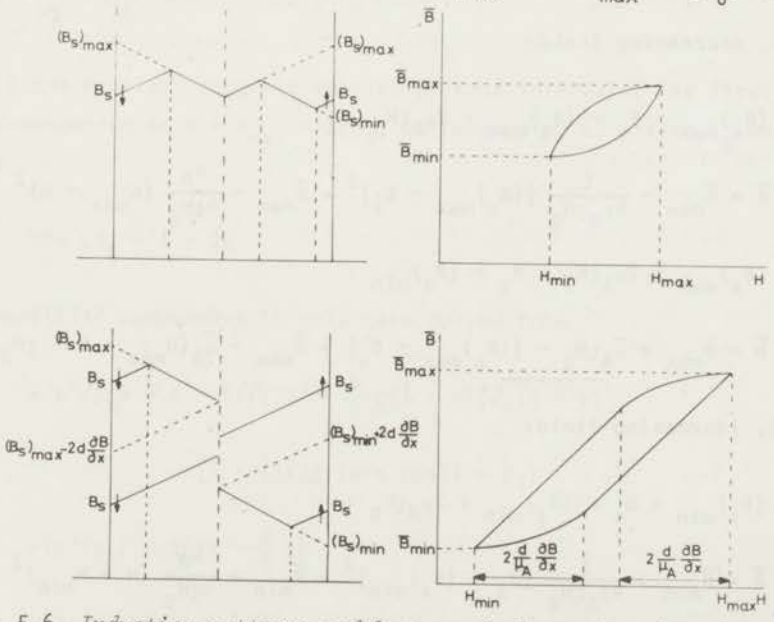

Fig. 5.6 *Induction patterns and hysteresis loops for the London-Bean model (sections 5.2.2 and 5.3.3). Upper part, $\zeta > 1$; lower part, $\zeta < 1$.*

sum of the areas of two trapezoids; for the region $H_{max} - 2\zeta H_0 > H > H_{min}$, from the area of one trapezoid (see the lower half of fig. 5.6). In increasing field the phenomena are analogous.

All these calculations have been carried out. The result is that the hysteresis loop which represents $\overline{B}$ as a function of H consists, in the case $\zeta > 1$, of two parabolas. In the case $\zeta < 1$ it consists of two parabolas and two linear parts. This is illustrated in the right-hand part of fig. 5.6.

The formulae are:

$\zeta > 1$, decreasing field:

$$\overline{B} = \overline{B}_{max} - \frac{1}{4\mu_A \zeta H_0} [(B_s)_{max} - B_s]^2 = \overline{B}_{max} - \frac{\mu_A}{4\zeta H_0} [H_{max} - H]^2 \quad (5.20a)$$

$\zeta > 1$, increasing field:

$$\overline{B} = \overline{B}_{min} + \frac{1}{4\mu_A \zeta H_0} [B_s - (B_s)_{min}]^2 = \overline{B}_{min} + \frac{\mu_A}{4\zeta H_0} [H - H_{min}]^2 \quad (5.20b)$$

with

$$\overline{B}_{max} - \overline{B}_{min} = \frac{1}{4\mu_A \zeta H_0} [(B_s)_{max} - (B_s)_{min}]^2 = \frac{\mu_A}{4\zeta H_0} (H_{max} - H_{min})^2 \quad (5.21)$$

$\zeta < 1$, decreasing field:

$(B_s)_{max} > B_s > (B_s)_{max} - 2\mu_A \zeta H_0$:

$$\overline{B} = \overline{B}_{max} - \frac{1}{4\mu_A \zeta H_0} [(B_s)_{max} - B_s]^2 = \overline{B}_{max} - \frac{\mu_A}{4\zeta H_0} (H_{max} - H)^2 \quad (5.22a)$$

$(B_s)_{max} - 2\mu_A \zeta H_0 > B_s > (B_s)_{min}$:

$$\overline{B} = \overline{B}_{max} + \mu_A \zeta H_0 - [(B_s)_{max} - B_s] = \overline{B}_{max} - \mu_A (H_{max} - H - \zeta H_0) \quad (5.22b)$$

$\zeta < 1$, increasing field:

$(B_s)_{min} < B_s < (B_s)_{min} + 2\mu_A \zeta H_0$:

$$\overline{B} = \overline{B}_{min} + \frac{1}{4\mu_A \zeta H_0} [B_s - (B_s)_{min}]^2 = \overline{B}_{min} + \frac{\mu_A}{4\zeta H_0} (H - H_{min})^2 \quad (5.22c)$$

$$(B_s)_{min} + 2\mu_A\zeta H_0 < B_s < (B_s)_{max} :$$

$$\overline{B} = \overline{B}_{min} - \mu_A\zeta H_0 + [B_s - (B_s)_{min}] = \overline{B}_{min} + \mu_A(H - H_{min} - \zeta H_0) \tag{5.22d}$$

with

$$\overline{B}_{max} - \overline{B}_{min} = [(B_s)_{max} - (B_s)_{min}] - \mu_A\zeta H_0 = \mu_A(H_{max} - H_{min} - \zeta H_0) \tag{5.23}$$

It is obvious that $\mu_A\zeta$ is the fraction of B_s over which $\overline{B}$ varies quadratically, and that ζ is the fraction of H over which this happens; ζ is the dimensionless parameter referred to in section 5.2.2.

In these formulae we can insert (5.1) for H and then compute the permeability components from (5.3a) and (5.3b). For $\zeta > 1$ each Fourier integral consists of two intervals. The result can be written

$$\frac{\mu'}{\mu_A} = \frac{1}{2\zeta} \tag{5.24a}$$

$$\frac{\pi\mu''}{\mu_A} = \frac{2}{3\zeta} \tag{5.24b}$$

For $\zeta < 1$ the Fourier integrals consist of four intervals. The first and second are interconnected at $H = H_{max} - 2\zeta H_0$, corresponding to a time t_B which is given by

$$\cos \omega t_B = 1 - 2\zeta$$

The permeability components in this case follow from

$$\pi(\mu'/\mu_A) = \pi - (1/\zeta)[1 - \tfrac{4}{3}\zeta(1 - \zeta)]\sqrt{\zeta(1 - \zeta)}$$

$$- [1 - (1/2\zeta)]\arccos(1 - 2\zeta) \tag{5.25a}$$

$$\pi(\mu''/\mu_A) = 2\zeta(1 - \tfrac{2}{3}\zeta) \tag{5.25b}$$

The relation between μ'/μ_A and μ''/μ_A is represented by the lower curve of fig. 5.3. The linear part of the curve refers to (5.24a) and (5.24b), the

curved part to (5.25a) and (5.25b). The two parts are interconnected with equal slopes at $\mu'/\mu_A = \frac{1}{2}$, $\mu''/\mu_A = 2/(3\pi)$. The maximum occurs at $\mu'/\mu_A = 0.641$, $\mu''/\mu_A = 3/(4\pi)$.

The alternating field losses per unit volume per cycle follow from (5.4). For the case $\zeta > 1$ we obtain

$$W = \frac{1}{6\pi} \frac{\mu_A^2}{d} \left(\frac{\partial B}{\partial x}\right)^{-1} H_0^3 \tag{5.26}$$

For $\zeta < 1$ the result is

$$W = \frac{1}{2\pi} dH_0 \left(\frac{\partial B}{\partial x}\right) \left[1 - \frac{2d}{3\mu_A H_0} \left(\frac{\partial B}{\partial x}\right)\right] \tag{5.27}$$

which is the same as London's result [3]) if μ_A is taken unity and $\frac{\partial B}{\partial x}$ is replaced by $4\pi J_c$ (see section 5.2.2).

5.3.4 *The London-Bean model with an irreversible surface jump.* The case that both bulk pinning and surface screening occur (section 5.2.3) can be treated by introducing an "Abrikosov field" H_A. So the procedure is somewhat similar to that of the second half of section 5.3.2. This time we must distinguish four induction and field quantities: the average inductance $\overline{B}$, determined in the experiment; the surface inductance B_s; the Abrikosov field H_A, which is in reversible equilibrium with B_s and the external field H.

The flux pattern inside the sample is the same as in the pure London-Bean model, so that the relation between $\overline{B}$ and B_s can be expressed again in terms of the parameter ζ, defined by (5.19). For the case $\zeta > 1$ it is represented by the first two members of equations (5.20a), (5.20b) and (5.21); for $\zeta < 1$ it is represented by the first two members of (5.22a), (5.22b), (5.22c), (5.22d) and (5.23).

The relation between H_A and B_s is determined by the slope of the Abrikosov curve μ_A. We obtain

$$(B_s)_{max} - B_s = \mu_A[(H_A)_{max} - H_A] \tag{5.28a}$$

$$B_s - (B_s)_{min} = \mu_A[H_A - (H_A)_{min}] \tag{5.28b}$$

similar to (5.12a) and (5.12b).

The relation between H and H_A is determined by the irreversible surface jump ΔH. It can be expressed in terms of the parameter η, defined by (5.5). In the case $\eta > 1$ we have, throughout the alternating field cycle,

$$H_A = (H_A)_{max} = H_{max} - \eta H_0 \tag{5.29}$$

which is similar to (5.6); in the case $\eta < 1$ we have, in decreasing field,

$$H_{max} > H > H_{max} - 2\eta H_0: \quad H_A = H_{max} - \eta H_0 \tag{5.30a}$$

$$H_{max} - 2\eta H_0 > H > H_{min}: \quad H_A = H + \eta H_0 \tag{5.30b}$$

and, in increasing field,

$$H_{min} < H < H_{min} + 2\eta H_0: \quad H_A = H_{min} + \eta H_0 \tag{5.30c}$$

$$H_{min} + 2\eta H_0 < H < H_{max}: \quad H_A = H - \eta H_0 \tag{5.30d}$$

similar to (5.7a), (5.7b), (5.7c) and (5.7d). The relations between H, H_A, B_s, and the internal flux pattern are illustrated in fig. 5.7. For all these formulae the assumption has been made that $H_{max} - H_{min}$ is small compared to $H_{c_2} - H_{c_1}$, so that μ_A, ζ and η can be considered as constants.

Eliminating H_A and B_s from these expressions we can obtain relations between $\overline{B}$ and H. For the calculation of the hysteresis loop we must now distinguish three cases:

$$H_{min} > H_{max} - 2\Delta H \qquad \text{or} \quad \eta > 1$$

$$H_{max} - 2\Delta H > H_{min} > H_{max} - 2\Delta H - \frac{2d}{\mu_A}\left(\frac{\partial B}{\partial x}\right) \qquad \text{or} \quad \eta < 1 < \eta + \zeta$$

$$H_{max} - 2\Delta H - \frac{2d}{\mu_A}\left(\frac{\partial B}{\partial x}\right) > H_{min} \qquad \text{or} \quad \eta + \zeta < 1$$

In the case $\eta > 1$ we have throughout the magnetization cycle

$$\overline{B} = \overline{B}_{max} \tag{5.31}$$

The hysteresis loop consists of a horizontal line. This case is illustrated in the upper part of fig. 5.8.

In the case $\eta < 1 < \eta + \zeta$ the loop consists of two horizontal lines and two parabolas, as shown in the middle part of fig. 5.8. The formulae are, in decreasing field,

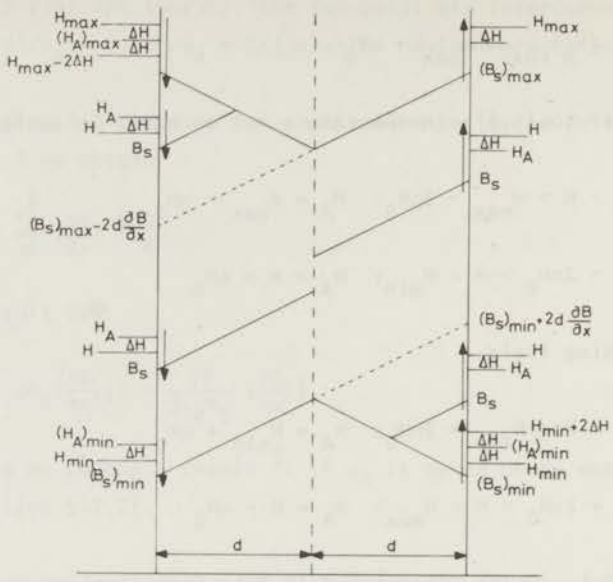

Fig. 5.7 *Induction patterns for the London-Bean model with a surface barrier (sections 5.2.3 and 5.3.4) for various values of the external field. The left-hand half of the figure refers to decreasing field and the right-hand half to increasing field, as indicated by the arrows. The same values of the external field were chosen for both halves of the figure.*

$$H_{max} > H > H_{max} - 2\eta H_0: \quad \overline{B} = \overline{B}_{max} \tag{5.32a}$$

$$H_{max} - 2\eta H_0 > H > H_{min}: \quad \overline{B} = \overline{B}_{max} - \frac{\mu_A}{4\zeta H_0}(H_{max} - H - 2\eta H_0)^2 \tag{5.32b}$$

in increasing field we have

$$H_{min} < H < H_{min} + 2\eta H_0: \quad \overline{B} = \overline{B}_{min} \tag{5.32c}$$

$$H_{min} + 2\eta H_0 < H < H_{max}: \quad \overline{B} = \overline{B}_{min} + \frac{\mu_A}{4\zeta H_0}(H - H_{min} - 2\eta H_0)^2 \tag{5.32d}$$

with

$$\overline{B}_{max} - \overline{B}_{min} = \frac{\mu_A}{4\zeta H_0}(H_{max} - H_{min} - 2\eta H_0)^2 \tag{5.33}$$

In the case $\eta + \zeta < 1$ the loop consists of two horizontal lines, two

parabolas, and two straight lines with finite slope, as indicated in the lower part of fig. 5.8. The formulae, in decreasing field,

$$H_{max} > H > H_{max} - 2\eta H_0 :$$

$$\overline{B} = \overline{B}_{max} \tag{5.34a}$$

$$H_{max} - 2\eta H_0 > H > H_{max} - 2\eta H_0 - 2\zeta H_0 :$$

$$\overline{B} = \overline{B}_{max} - \frac{\mu_A}{4\zeta H_0} (H_{max} - H - 2\eta H_0)^2 \tag{5.34b}$$

$$H_{max} - 2\eta H_0 - 2\zeta H_0 > H > H_{min} :$$

$$\overline{B} = \overline{B}_{max} - \mu_A (H_{max} - H - 2\eta H_0 - \zeta H_0) \tag{5.34c}$$

in increasing field we have

$$H_{min} < H < H_{min} + 2\eta H_0 :$$

$$\overline{B} = \overline{B}_{min} \tag{5.34d}$$

$$H_{min} + 2\eta H_0 < H < H_{min} + 2\eta H_0 + 2\zeta H_0 :$$

$$\overline{B} = \overline{B}_{min} + \frac{\mu_A}{4\zeta H_0} (H - H_{min} - 2\eta H_0)^2 \tag{5.34e}$$

$$H_{min} + 2\eta H_0 + 2\zeta H_0 < H < H_{max} :$$

$$\overline{B} = \overline{B}_{min} + \mu_A (H - H_{min} - 2\eta H_0 - \zeta H_0) \tag{5.34f}$$

with

$$\overline{B}_{max} - \overline{B}_{min} = \mu_A (H_{max} - H_{min} - 2\eta H_0 - \zeta H_0) \tag{5.35}$$

Now η is the fraction of the varying field over which $\overline{B}$ is constant, ζ is the fraction over which it varies quadratically, and $1 - \eta - \zeta$ is the linear fraction.

In all these cases we can calculate μ' and μ'' from (5.3a) and (5.3b) after inserting (5.1) for H. In the case $\eta > 1$ we obtain, simply,

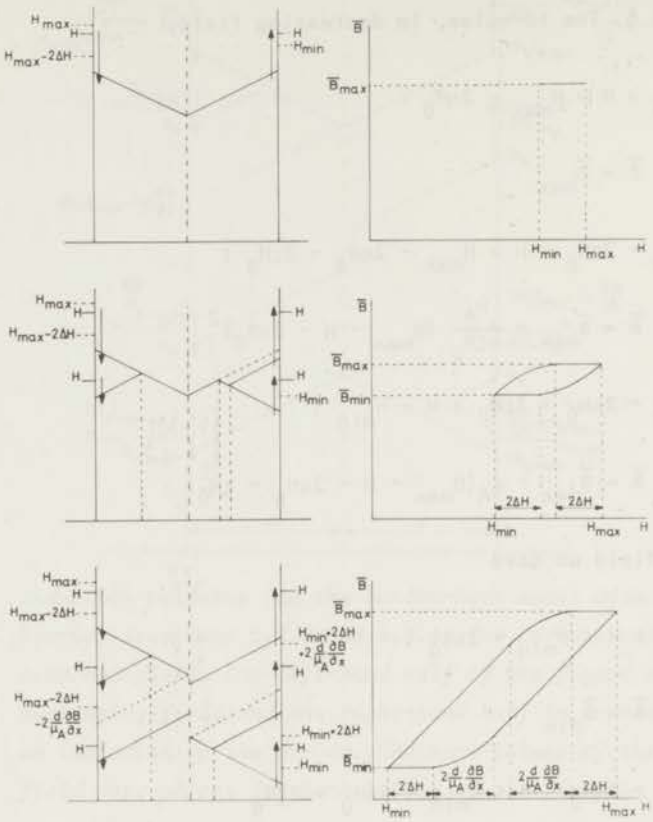

Fig. 5.8 *Induction patterns and hysteresis loops for the London-Bean model with a surface barrier (sections 5.2.3 and 5.3.4). Upper part,* $\eta > 1$; *middle part,* $\eta < 1 < \eta + \zeta$; *lower part,* $\eta + \zeta < 1$.

$$\mu'/\mu_A = 0 \tag{5.36a}$$

$$\mu''/\mu_A = 0 \tag{5.36b}$$

In the case $\eta < 1 < \eta + \zeta$ each Fourier integral consists of four intervals. The first and second are connected at $H = H_{max} - 2\eta H_0$, corresponding to a time t_A obeying

$$\cos \omega t_A = 1 - 2\eta$$

The permeability components are

$$\pi(\mu'/\mu_A) = (1/2\zeta)\{2[1 - \frac{4}{3}\eta(1 - \eta)]\sqrt{\eta(1 - \eta)} + (1 - 2\eta)\arccos(2\eta - 1)\} \quad (5.37a)$$

$$\pi(\mu''/\mu_A) = (2/3\zeta)(1 - \eta)^2(1 + 2\eta) \quad (5.37b)$$

In the case $\eta + \zeta < 1$ each Fourier integral consists of six intervals. The first and second are connected at $H = H_{max} - 2\eta H_0$ corresponding again to $\cos \omega t_A = 1 - 2\eta$. The second and third are connected at $H = H_{max} - 2\eta H_0 - 2\zeta H_0$, corresponding to t_B which obeys

$$\cos \omega t_B = 1 - 2\eta - 2\zeta$$

The permeability components are

$$\pi(\mu'/\mu_A) = \pi - (1/2\zeta)\{2[1 - \frac{4}{3}(\eta + \zeta)(1 - \eta - \zeta)]\sqrt{(\eta + \zeta)(1 - \eta - \zeta)} - 2[1 - \frac{4}{3}\eta(1 - \eta)]\sqrt{\eta(1 - \eta)} - (1 - 2\eta - 2\zeta)\arccos(1 - 2\eta - 2\zeta) + (1 - 2\eta)\arccos(1 - 2\eta)\} \quad (5.38a)$$

$$\pi(\mu''/\mu_A) = 2\zeta(1 - \frac{2}{3}\zeta) + 4\eta(1 - \eta - \zeta) \quad (5.38b)$$

For $\eta = 0$ eqs. (5.37a) and (5.37b) become equivalent with (5.24a) and (5.24b), whereas (5.38a) and (5.38b) become equivalent with (5.25a) and (5.25b). This leads again to the London-Bean curve of fig. 5.3. If we take $\zeta = 0$ in (5.38a) and (5.38b) the l'Hôpital limit gives (5.16a) and (5.16b), hence the upper curve of fig. 5.3, the limit referred to in section 5.3.2.

Arbitrary combinations of η and ζ give points in the μ'/μ_A, μ''/μ_A diagram between these two curves. The general case will be discussed in detail in section 5.4.1.

The alternating field losses per unit volume and per cycle are obtained by substituting χ'' in (5.4). For $\eta > 1$ the losses are zero. For $\eta < 1 < \eta + \zeta$ we obtain

$$W = \frac{\mu_A^2}{6\pi d}\left(\frac{\partial B}{\partial x}\right)^{-1}(H_0 - \Delta H)^2(H_0 + 2\Delta H) \qquad (5.39)$$

which is equivalent with the expression of Sekula and Barrett [18]) (see section 5.2.3). The case $\eta + \zeta < 1$ leads to

$$W = \frac{\mu_A}{2\pi}\{H_0[\frac{d}{\mu_A}(\frac{\partial B}{\partial x}) + 2\Delta H]\cdot[\frac{2d^2}{3\mu_A^2}(\frac{\partial B}{\partial x})^2] +$$

$$+ \frac{2d}{\mu_A}(\frac{\partial B}{\partial x})\Delta H + 2(\Delta H)^2\} \qquad (5.40)$$

which is linear in amplitude.

5.3.5 *The London-Bean model extended with a surface layer without pinning.*

In the case of a surface layer of thickness δd in which $\partial B/\partial x = 0$ and a core with constant $\partial B/\partial x$ (the case of section 5.2.4) the relation between the external field H and the surface induction B_s is determined by the reversible Abrikosov curve. This means that, if $H_{max} - H_{min}$ is so small that μ_A can be considered as a constant, the relations (5.18a) and (5.18b) remain valid.

The induction in the surface layer obeys

$$B = B_s$$

and the flux pattern in the core is analogous to that of the pure London-Bean model of section 5.3.3. This is illustrated in fig. 5.9.

If the field is increased from zero to H_{max} the induction in the core decreases linearly towards the axis. If the field decreases again the induction in the surface layer adapts itself to the Abrikosov value and, as long as

$$B_s > (B_s)_{max} - 2(1 - \delta)d(\frac{\partial B}{\partial x})$$

the induction in the core first increases and then decreases; in the region

$$B_s < (B_s)_{max} - 2(1 - \delta)d(\frac{\partial B}{\partial x})$$

it increases all the way until the centre of the sample (see, also, section 5.2.4).

In increasing field the phenomena are analogous.

For the computation of the average flux density $\overline{B}$ we must now distinguish

between the cases

$$(B_s)_{max} - (B_s)_{min} < 2(1 - \delta)d(\frac{\partial B}{\partial x}) \quad \text{or } (1 - \delta)\zeta > 1$$

$$(B_s)_{max} - (B_s)_{min} > 2(1 - \delta)d(\frac{\partial B}{\partial x}) \quad \text{or } (1 - \delta)\zeta < 1$$

where ζ is defined again by (5.19).

In the case $(1 - \delta)\zeta > 1$ in decreasing field the relation between $\overline{B}$ and B_s is calculated from the sum of the areas of a rectangle and two trapezoids; in increasing field it follows from the sum of the areas of a rectangle and three trapezoids. This is illustrated in the upper half of fig. 5.10.

In the case $(1 - \delta)\zeta < 1$ in decreasing field the relation between $\overline{B}$ and B_s is derived, in the region $(B_s)_{max} > B_s > (B_s)_{max} - 2(1 - \delta)d(\partial B/\partial x)$, from the areas of a rectangle and two trapezoids and in the region $(B_s)_{max} - 2(1 - \delta)d(\partial B/\partial x) > B_s > (B_s)_{min}$ from the areas of a rectangle and one trapezoid. In increasing field the phenomena are analogous (see the lower half of fig. 5.10).

The results are, after insertion of (5.18a) and (5.18b) for B_s,

$(1 - \delta)\zeta > 1$, decreasing field

$$\overline{B} = \overline{B}_{max} - \mu_A\delta(H_{max} - H) - \frac{\mu_A}{4\zeta H_0}(H_{max} - H)^2 \qquad (5.41a)$$

$(1 - \delta)\zeta > 1$, increasing field

$$\overline{B} = \overline{B}_{min} + \mu_A\delta(H - H_{min}) + \frac{\mu_A}{4\zeta H_0}(H - H_{min})^2 \qquad (5.41b)$$

with

$$\overline{B}_{max} - \overline{B}_{min} = \mu_A\delta(H_{max} - H_{min}) + \frac{\mu_A}{4\zeta H_0}(H_{max} - H_{min})^2 \qquad (5.42)$$

$(1 - \delta)\zeta < 1$, decreasing field

$(B_s)_{max} > B_s > (B_s)_{max} - 2(1 - \delta)\mu_A\zeta H_0$:

$$\overline{B} = \overline{B}_{max} - \mu_A\delta(H_{max} - H) - \frac{\mu_A}{4\zeta H_0}(H_{max} - H)^2 \qquad (5.43a)$$

$(B_s)_{max} - 2(1 - \delta)\mu_A\zeta H_0 > B_s > (B_s)_{min}$:

$$\overline{B} = \overline{B}_{max} + (1 - \delta)^2\mu_A\zeta H_0 - \mu_A(H_{max} - H) \qquad (5.43b)$$

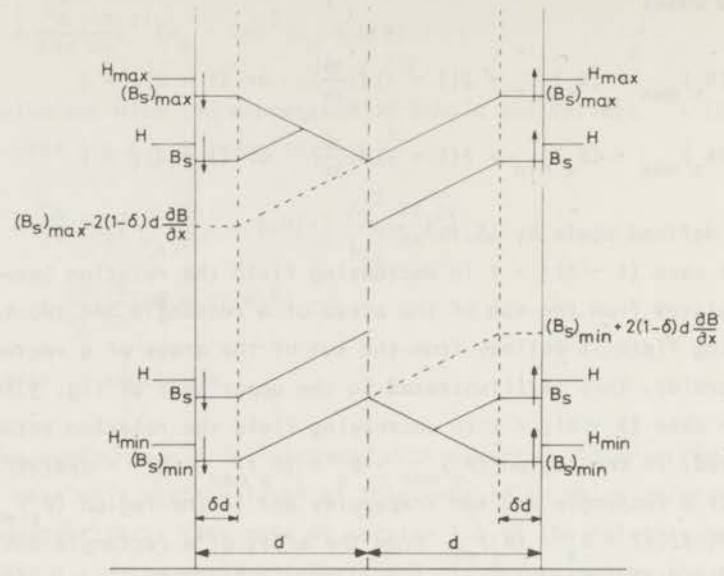

Fig. 5.9 *Induction patterns for the London-Bean model with a surface layer without pinning (sections 5.2.4 and 5.3.5). The left-hand half of the figure refers to decreasing field and the right-hand half to increasing field, as indicated by the arrows. The same values for the external field were chosen for both halves of the figure.*

$(1 - \delta)\zeta < 1$, increasing field

$(B_s)_{min} < B_s < (B_s)_{min} + 2(1 - \delta)\mu_A\zeta H_0$:

$$\overline{B} = \overline{B}_{min} + \mu_A\delta(H - H_{min}) + \frac{\mu_A}{4\zeta H_0}(H - H_{min})^2 \qquad (5.43c)$$

$(B_s)_{min} + 2(1 - \delta)\mu_A\zeta H_0 < B_s < (B_s)_{max}$:

$$\overline{B} = \overline{B}_{min} - (1 - \delta)^2\mu_A\zeta H_0 + \mu_A(H - H_{min}) \qquad (5.43d)$$

with

$$\overline{B}_{max} - \overline{B}_{min} = \mu_A[H_{max} - H_{min} - (1 - \delta)^2\zeta H_0] \qquad (5.44)$$

The hysteresis loop which represents $\overline{B}$ as a function of H consists, in the case $(1 - \delta)\zeta > 1$, of two parabolas. In the case $(1 - \delta)\zeta < 1$ it consists

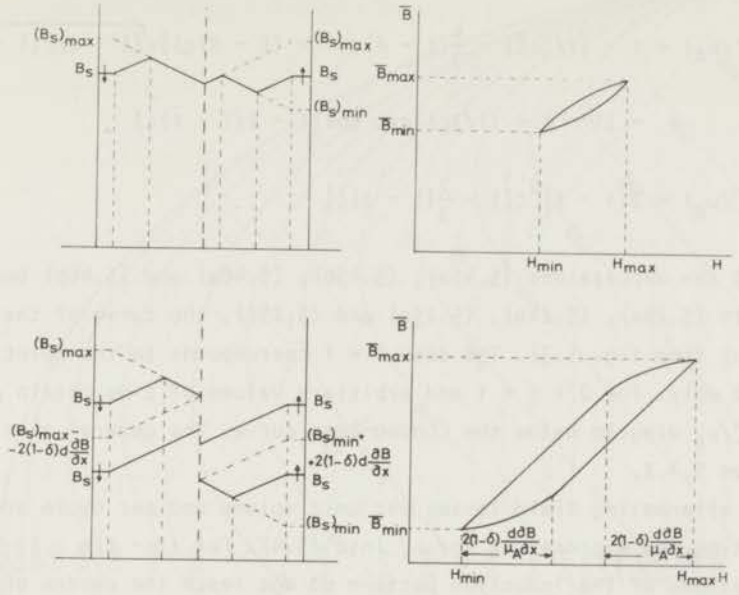

Fig. 5.10 *Induction patterns and hysteresis loops for the London-Bean model with a surface layer without pinning (sections 5.2.4 and 5.3.5). Upper part, $(1 - \delta)\zeta > 1$; lower part, $(1 - \delta)\zeta < 1$.*

of two parabolas and two linear parts (see the right-hand part of fig. 5.10). The difference with the pure London-Bean model of fig. 5.6 is that there the parabolas started with horizontal tangents, now they start with finite slopes.

In these formulae we can insert (5.1) for H and then calculate μ' and μ'' from (5.3a) and (5.3b). For $(1 - \delta)\zeta > 1$ each Fourier integral consists of two intervals. The result can be written

$$\frac{\mu'}{\mu_A} = \delta + \frac{1}{2\zeta} \tag{5.45a}$$

$$\pi\frac{\mu''}{\mu_A} = \frac{2}{3\zeta} \tag{5.45b}$$

For $(1 - \delta)\zeta < 1$ each Fourier integral consists of four intervals. The first two are interconnected at $H = H_{max} - 2(1 - \delta)\zeta H_0$, corresponding to t_B, which obeys

$$\cos \omega t_B = 1 - 2(1 - \delta)\zeta$$

The result is

$$\pi(\mu'/\mu_A) = \pi - (1/\zeta)[1 - \tfrac{4}{3}(1 - \delta)\zeta(1 - (1 - \delta)\zeta)]\sqrt{(1 - \delta)\zeta[1 - (1 - \delta)\zeta]}$$

$$- [1 - \delta - (1/2\zeta)]\arccos[1 - 2(1 - \delta)\zeta] \qquad (5.46a)$$

$$\pi(\mu''/\mu_A) = 2(1 - \delta)^2\zeta[1 - \tfrac{2}{3}(1 - \delta)\zeta] \qquad (5.46b)$$

For $\delta = 0$ the expressions (5.45a), (5.45b), (5.46a) and (5.46b) become identical with (5.24a), (5.24b), (5.25a) and (5.25b), the curve of the pure London-Bean model (see fig. 5.3). The case $\delta = 1$ corresponds to the point $\mu'/\mu_A = 1$, $\mu''/\mu_A = 0$ only. For $0 < \delta < 1$ and arbitrary values of ζ we obtain points in the μ'/μ_A, μ''/μ_A diagram below the London-Bean curve. The general case is discussed in section 5.4.2.

The alternating field losses per unit volume and per cycle are obtained by inserting the expressions for μ'' into (5.4). For $(1 - \delta)\zeta > 1$, the case that the variations of the induction pattern do not reach the centre of the sample, we obtain

$$W = \frac{\mu_A^2}{6\pi d}\left(\frac{\partial B}{\partial x}\right)^{-1} H_0^3 \qquad (5.47)$$

identical with (5.26), the case of the pure London-Bean model (see, also, section 5.2.4). For $(1 - \delta)\zeta < 1$ we obtain the relation

$$W = \frac{d(1 - \delta)^2}{2\pi} H_0\left(\frac{\partial B}{\partial x}\right)\left[1 - \frac{2d(1 - \delta)}{3\mu_A H_0}\left(\frac{\partial B}{\partial x}\right)\right] \qquad (5.48)$$

somewhat similar to (5.27).

§5.4 *Discussion of the models*

5.4.1 *The permeability diagram.* The full permeability diagram which shows μ''/μ_A as a function of μ'/μ_A is given in fig. 5.11.

At the top it is bounded by the curve of section 5.3.2, which represents eqs. (5.16a) and (5.16b). The parameter η obeys (5.5). The curve, here referred to as $\zeta = 0$, is identical with the upper one of fig. 5.3 and it describes the case when only surface screening occurs and no bulk pinning.

The region enclosed by this curve is divided into two separate parts by the London-Bean curve. It is the heavy line in fig. 5.11, and it is identical with the lower line of fig. 5.3. Here it is referred to by both $\eta = 0$ and

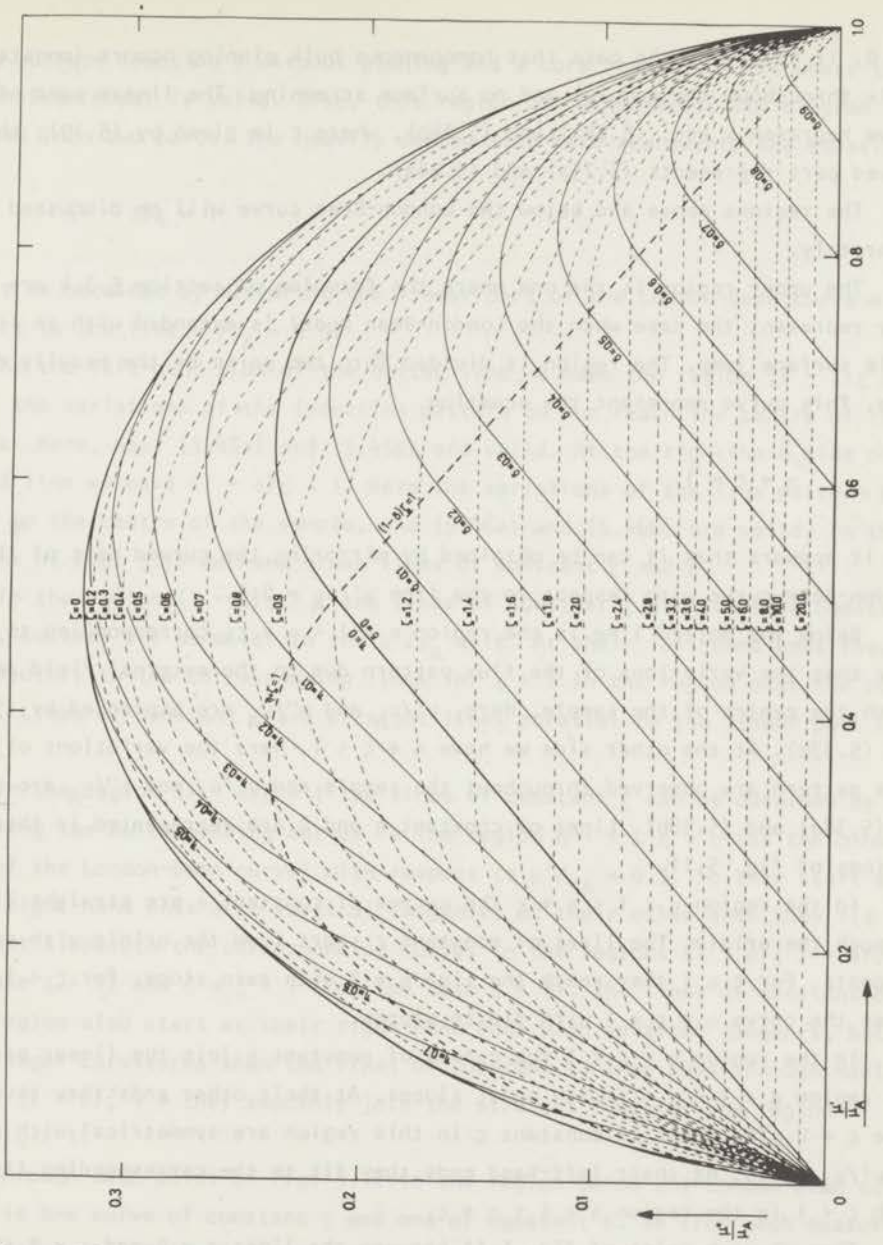

Fig. 5.11 *The permeability diagram showing* μ''/μ_A *vs.* μ'/μ_A. *The heavy line in the middle is the London-Bean curve* $\eta = 0$, $\delta = 0$. μ', μ'' *combinations in the region above it lead to* η, ζ *combinations from which* ΔH *and* $\partial B/\partial x$ *can be derived [eqs. (5.5) and (5.19)].* μ', μ'' *combinations in the region below it lead to* δ, ζ *combinations from which the thickness of the surface layer without pinning* (δd) *and* $\partial B/\partial x$ [*eq. (5.19)*] *can be derived.*

$\delta = 0$. It describes the case that homogeneous bulk pinning occurs (constant $\partial B/\partial x$ throughout the sample) and no surface screening. The linear part of this curve represents eqs. (5.24a) and (5.24b), where ζ is given by (5.19); the curved part represents (5.25a) and (5.26a).

The regions above and below the London-Bean curve will be discussed separately.

The upper region is the one where the formulae of section 5.3.4 are valid. They represent the case when the London-Bean model is extended with an irreversible surface jump. The region is divided into two parts by the heavily dotted line. This curve represent the equation

$$\eta + \zeta = 1$$

and it appears that it can be obtained by mirroring the curved part of the London-Bean curve with respect to the line $\mu'/\mu_A = 0.5$.

Below the dotted line is the region $\eta < 1 < \eta + \zeta$, corresponding to the case that the variations of the flux pattern due to the external field do not reach the centre of the sample. Here, μ'/μ_A and μ''/μ_A are expressed by (5.37a) and (5.37b). At the other side we have $\eta + \zeta < 1$. Here the variations of the flux pattern are observed throughout the sample and μ'/μ_A and μ''/μ_A are given by (5.38a) and (5.38b). Lines of constant η and ζ are represented in these regions of fig. 5.11.

In the region $\eta < 1 < \eta + \zeta$ the curves of constant η are straight lines through the origin. The lines of constant ζ start from the origin with vertical tangents. For $\zeta \geq 1$ they reach the line $\eta = 0$ with zero slope. For $\zeta < 1$ they cross the curve $\eta + \zeta = 1$ with finite slopes.

In the region $\eta + \zeta < 1$ the curves of constant η join the linear parts of the region $\eta < 1 < \eta + \zeta$ with equal slopes. At their other ends they touch the line $\zeta = 0$. The lines of constant ζ in this region are symmetrical with respect to $\mu'/\mu_A = 0.5$. At their left-hand ends they fit to the corresponding lines with $\zeta < 1$ in the region $\eta < 1 < \eta + \zeta$.

Through each point of fig. 5.11 between the lines $\zeta = 0$ and $\eta = 0$ there is one curve of constant η and one of constant ζ. So, for a measured combination μ', μ'' in this region we can read the corresponding values of η and ζ from the diagram. From η we can calculate the surface jump ΔH using (5.5), from ζ we obtain $\partial B/\partial x$ applying (5.19).

The part of fig. 5.11 below the London-Bean curve is the region where the relations of section 5.3.5 are valid. They represent the case that the sample

has a surface fraction δ without pinning and a core fraction $1 - \delta$ where the London-Bean model is valid. Also, this region of the permeability diagram is divided into two parts. The heavily dotted line here represents the equation

$$(1 - \delta)\zeta = 1$$

and it is obtained by mirroring the linear part of the London-Bean curve with respect to the line $\mu'/\mu_A = 0.5$.

At the left-hand side of the dotted line we have the region $(1 - \delta)\zeta > 1$, where the variations of the induction pattern do not reach the centre of the sample. Here, eqs. (5.45a) and (5.45b) are valid. At the right-hand side of the dotted line we have $(1 - \delta)\zeta < 1$. Here the variations of the flux pattern penetrate to the centre of the sample, and (5.46a) and (5.46b) are valid. In these regions of fig. 5.11 we have drawn lines of constant ζ and δ.

In the region $(1 - \delta)\zeta > 1$ the lines of constant ζ are lines of constant μ''/μ_A, so they are parallel to the μ'/μ_A axis. At their left-hand ends they fit smoothly to the corresponding lines for $\zeta > 1$ in the region over the curve $\delta = 0$. Lines of constant δ are straight lines parallel to the linear part of $\delta = 0$.

In the region $(1 - \delta)\zeta < 1$ the lines of constant ζ can be obtained by mirroring the corresponding curves in the region $\eta < 1 < \eta + \zeta$ (at the other side of the London-Bean curve) with respect to $\mu'/\mu_A = 0.5$. So they start at their right-hand ends with vertical tangents. At their other ends they fit with constant slopes to the corresponding curves in the regions $(1 - \delta)\zeta > 1$ (for the case $\zeta > 1$) and $\eta + \zeta < 1$ (for the case $\zeta < 1$). The lines of constant δ in this region also start at their right-hand ends with vertical tangents, but with larger curvatures than the lines of constant ζ. They pass through maxima and at $(1 - \delta)\zeta = 1$ they smoothly join the straight lines of the region $(1 - \delta)\zeta > 1$.

Through each point of fig. 5.11 in the region below the London-Bean curve there is one curve of constant ζ and one of constant δ. So from each measured combination μ', μ'' in this region we can directly read the corresponding values of ζ and δ. From δ we can calculate the thickness δd of the surface layer without pinning; from ζ we can derive the flux density gradient $\partial B/\partial x$ in the core, using (5.19).

The very strict division of the permeability diagram into two separate regions by the London-Bean curve (with different parameters at each side of the curve) is due to the lack of flexibility of our models. We either introduce

an irreversible surface jump or a surface layer without pinning. It is possible to perform calculations on a model in which they both occur simultaneously. In that case no such strict division is found.

The disadvantage of that model is, however, that we obtain three adaptable parameters simultaneously (ζ, η and δ), and in general a three-parameter model is appreciably less critical for the discussion of experimental results than a two-parameter model. Moreover, the nice property of the diagram of fig. 5.11, that the parameters can immediately be read off for each measured combination μ', μ'', is given up in the case of a three-parameter model.

5.4.2 *The results obtained with the sample P_{1600}.* As has been stated in section 5.2.1 (see fig. 5.1) the experimental results for P_{1000} are very well in agreement with the theoretical ones obtained from the calculations on the surface barrier above H_{c_2}. We will restrict ourselves now to a discussion on the sample P_{1600}.

Figure 5.3 shows the μ'/μ_A, μ''/μ_A data for the sample P_{1600} for four different amplitudes of the alternating field H_0 and various values of the steady field H_a. In section 5.2.2 we pointed out how this diagram was obtained.

Since almost all the experimental points are below the London-Bean curve we based our further calculations on the model of section 5.2.4 and on the formulae of section 5.3.5. From the comparison of figs. 5.3 and 5.1 we obtained values for the parameters δ and ζ, and from these we derived the thickness of the surface layer δd and the flux-density gradient $\partial B/\partial x$ [eq. (5.19)].

The results are shown in fig. 5.12. The left-hand part shows δd in microns against the external field H_a. The two dotted points at the bottom correspond to the points above the London-Bean curve, for which we took $\delta = 0$. The middle part shows $\partial B/\partial x$ and the right-hand part gives the critical current density as computed from the averaged $\partial B/\partial x$ values according to

$$4\pi J_c = \frac{\partial H}{\partial x} = \frac{1}{\mu_A}\left(\frac{\partial B}{\partial x}\right)$$

It turns out that, apart from the two dotted points for δd, all the values obtained with different amplitudes of the alternating field are in mutual agreement within a factor of two, and that there are no systematical differences between the values obtained with the different amplitudes. In view of the crudeness of our model and of the limited precision of our experimental data (small ac losses in the circuits of the Hartshorn bridge, uncertainties in the zero lines of the susceptibility measurements and in the graphical differentiation

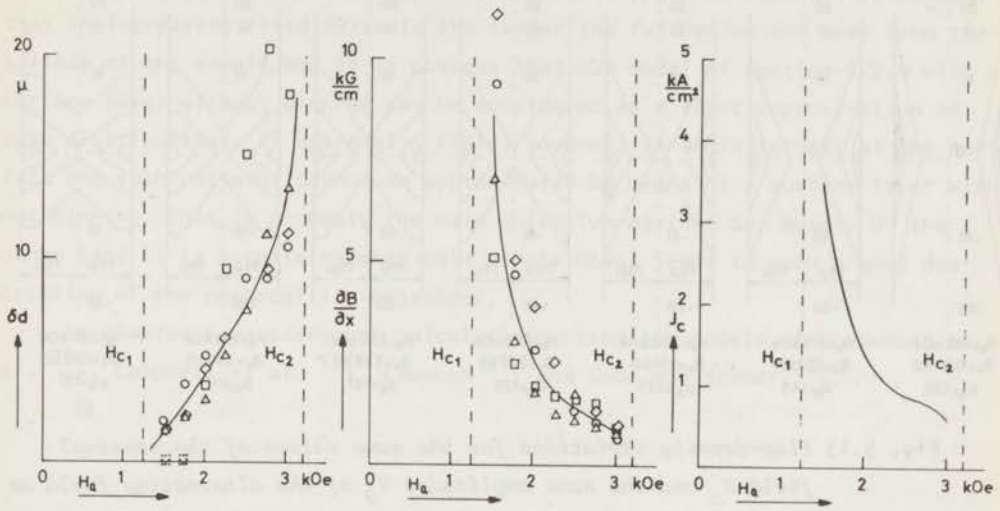

Fig. 5.12 *Results for the sample P_{1600}. Left-hand part, thickness of the surface layer without pinning vs. the external field H; middle part, flux-density gradient $\partial B/\partial x$; right-hand part, bulk critical current density J_c.* □ , H_0 = 9.52 Oe; △ , H_0 = 4.81 Oe; ○ , H_0 = 2.41 Oe; ◇ , H_0 = 0.72 Oe.

of the Abrikosov curve may lead to systematic errors which are hard to estimate) we think that this result is satisfactory. Also, the critical current densities of fig. 5.12 are of a reasonable order of magnitude for a sample with weak pinning.

Nevertheless, it seemed important to repeat the experiments with improved precision and with a larger number of amplitudes of the alternating field. Such investigations were carried out on the irradiated samples (see chapter 6).

The patterns of the flux-density variations for all four amplitudes and for the external field values of figs. 5.2 and 5.12 have been sketched in fig. 5.13. It follows that up to 2 kOe, even with the highest amplitude of 9.52 Oe, the centre of the sample is not reached. At 3 kOe the centre is already reached with an amplitude of 4.81 Oe.

The possibility exists that a model in which both a surface jump and a surface layer without pinning occur would lead to better agreement with the experimental results. The facts that our ac losses, shown in fig. 5.2, are proportional to $H_0^{3.3}$ instead of H_0^3 and that some of the results for the highest

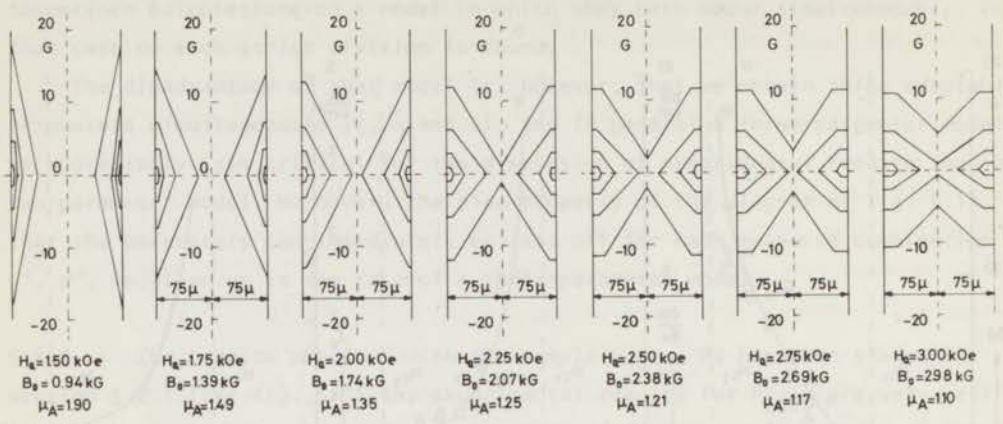

Fig. 5.13 *Flux-density variations for the same values of the external field H_a and the same amplitudes H_0 of the alternating field as in figs. 5.2 and 5.12. The total variation of the surface induction in each case is equal to $2\nu_A H_0$. The quantity plotted along the vertical axes is $B - \frac{1}{2}(B_{max} - B_{min})$.*

amplitude in fig. 5.3 are at the wrong side of the London-Bean curve may be indications that a small surface jump actually exists. At the end of section 5.4.1 we pointed out, however, that such a model has also some serious disadvantages.

The fact that for the sample P_{1000} the μ'' values near the origin are somewhat low (see fig. 5.1) can now easily be explained with the assumption that in the region just above H_{c_2} there is still a very small $\partial B/\partial x$, so that the corners of the hysteresis loop are slightly rounded off, like in the lower part of fig. 5.8. Experiments by Rollins and Silcox [12]) seem to indicate that this phenomenon may actually occur. We made some calculations based on the models of sections 5.2.3 and 5.3.4 which gave $\partial B/\partial x$ values an order of magnitude smaller than those found for sample P_{1600}.

5.4.3 *Other models.* All the formulae derived and discussed above were based on the London-Bean model with extensions in one direction or the other. It is the very simplest model available in the literature.

In the course of time several more sophisticated models for the flux-density distribution have been proposed [19-32]). A survey of most of them was given by Urban [30]). Some of them have as many as three adaptable parameters,

apart from the possibility of an additional irreversible surface jump.

For all of them $\partial B/\partial x$ decreases with increasing flux density. This means that in increasing field $\partial B/\partial x$ is the larger the further we are away from the surface of the sample and it is obvious that our model of section 5.2.4 with a surface layer without pinning can be considered as a first approximation of such distributions. In decreasing field, however, $\partial B/\partial x$ is largest at the surface and such patterns cannot be approximated by means of a surface layer without pinning. This is probably the main objection against our model. On the other hand it is surprising that this simple model leads to such a good description of the permeability behaviour.

In chapter 6 we carry out calculations using the models of Goedemoed et al. [26], Campbell et al. [29], Labusch [31] and Good and Kramer [32].

References

1. D. Saint James and P.G. de Gennes, Phys. Letters 7, 306 (1963).
2. S.L. Wipf, Proceedings 1968 Summer School on Superconducting Devices and Accelerators, Brookhaven National Laboratory Report 50155 (c-55), 1968.
3. H. London, Phys. Letters 6, 162 (1963).
4. C.P. Bean, Rev. Mod. Phys. 36, 31 (1964).
5. R. Hancox, Proc. IEE (London) 113, 1221 (1966).
6. I.M. Green and P. Hlawickza, Proc. IEE (London) 114, 1329 (1967).
7. S.H. Goedemoed, A. van der Giessen, D. de Klerk and C.J. Gorter, Phys. Letters 3, 250 (1963).
8. P.R. Doidge and Kwan Sik-Hung, Phys. Letters 12, 82 (1964).
9. P.P.J. van Engelen, G.J.C. Bots and B.S. Blaisse, Phys. Letters 19, 465 (1965).
10. H. Voigt, Phys. Letters 20, 262 (1966).
11. H.A. Ullmaier, Phys. Letters 21, 307 (1966).
12. R.W. Rollins and J. Silcox, Phys. Rev. 155, 404 (1967).
13. H.J. Fink, Phys. Rev. 161, 417 (1967).
14. L.J.M. van de Klundert, G.E. Alberga, L.C. van der Marel and C. Leynse, Proc. 3rd Intern. Cryog. Eng. Conf., Berlin, 1970.
15. H. Berndt, N. Kartascheff and H. Wenzl, Z. Angew. Phys. 24, 305 (1968).
16. J.E. Ostenson and D.K. Finnemore, Phys. Rev. Letters 22, 188 (1969).
17. A.M. Campbell, J. Phys. Soc. (London) C2, 1492 (1969).
18. S.T. Sekula and J.H. Barrett, Appl. Phys. Letters 17, 204 (1970).
19. Y.B. Kim, C.F. Hempstead and A.R. Strnad, Phys. Rev. 129, 528 (1963).
20. P.W. Anderson, Phys. Rev. Letters 9, 309 (1962).
21. J. Friedel, P.G. de Gennes and J. Matricon, Appl. Phys. Letters 2, 119 (1963).
22. J. Silcox and R.W. Rollins, Appl. Phys. Letters 2, 231 (1963).
23. K. Yasukochi, T. Ogasawara, N. Usui and S. Ushio, J. Phys. Soc. Japan 19, 1649 (1964).
24. F. Irie and K. Yamafuji, J. Phys. Soc. Japan 23, 255 (1967).
25. W.A. Fietz, M.R. Beasly, J. Silcox and W.W. Webb, Phys. Rev. 136, A335 (1964).
26. S.H. Goedemoed, P.H. Kes, F.Th.A. Jacobs and D. de Klerk, Physica 35, 273 (1967); Commun. Kamerlingh Onnes Lab. 356c.
27. T.H. Alden and J.D. Livingston, J. Appl. Phys. 37, 3551 (1966).

28. A.M. Campbell, J.E. Evetts and D. Dew-Hughes, Phil. Mag. 18, 313 (1968).
29. H.T. Coffey, Phys. Rev. 166, 447 (1968).
30. E.W. Urban, J. Appl. Phys. 42, 115 (1971).
31. R. Labusch, Crystal Lattice Defects 1, 1 (1969).
32. J.A. Good and E.J. Kramer, Phil. Mag. 22, 329 (1970).
33. P.H. Kes, C.A.M. van der Klein and D. de Klerk, J. of Low Temp. Phys. 10, 759 (1973).

CHAPTER 6

THE EFFECT OF NEUTRON IRRADIATION DAMAGE ON THE MAGNETIC BEHAVIOUR IN ALTERNATING FIELDS

§6.1 *Introduction*

In chapter 3 we discussed the influence of physical lattice defects, caused by neutron irradiation at reactor ambient temperatures, on the magnetic behaviour of superconducting niobium samples in stationary fields. In this chapter we will discuss the magnetic behaviour of the same neutron irradiated samples when an alternating field, with amplitude between 0.5 and 100 Oe is superimposed on the stationary field. Both ac and dc fields were parallel to the axis of the samples. As in the experiments discussed in chapter 2 the results were strongly dependent on the amplitude of the alternating field, but no frequency dependence was observed between 40 and 420 Hz.

The metallurgical character of the samples has been discussed in chapter 3, section 3.1, while the irradiation data are given in table 3.1. Electron microscope pictures are given in fig. 3.1.

§6.2 *Theoretical considerations*

The magnetic permeability μ determined in the experiments is directly related to the variations of the flux distribution in the sample caused by the ac field. The components μ' and μ'' can be obtained from a simple Fourier transformation of the measured induction $\overline{B}$. In chapter 5 these calculations were performed for four simple models, always under the assumption that the superconductor is in the critical state at any moment during the hysteresis cycle. The results can be represented very nicely in a plot of μ''/μ_A versus μ'/μ_A (fig. 5.11).

Similar computations can obviously be carried out for any other flux distribution pattern. For simple cases the formulae can be derived analytically, for more complicated cases numerical computer calculations are necessary.

Let us write the total pinning force per unit volume of the sample as [1]):

$$P_v = \gamma F^{-1}(B)(H_{c_2} - B)\frac{B}{4\pi}$$

where F(B) is a dimensionless function which is determined by the flux distribution model under consideration. Further γ is a parameter characterizing the pinning properties of the sample. It has the dimension of a reciprocal length and for a given model it can be derived directly from the static magnetization curve. The driving force per unit volume is given by formula (1.1) of Friedel, De Gennes and Matricon [2]). In the critical state, $F_d + P_v = 0$, the result can be written as:

$$\left(\frac{\partial H}{\partial B}\right)_{rev}\left|\frac{\partial B}{\partial x}\right| = \gamma F^{-1}(B)(H_{c_2} - B) \qquad (6.1)$$

which is valid both in increasing and decreasing fields. In these formulae H is the field in reversible equilibrium with the local induction. For the relation between B(x) and H(x) we adopt the empirical formulae (1.7) of Kes, van der Klein and De Klerk [1]).

Introducing the reduced quantities:

$$h_a = (H_a - H_{c_1})/H_{c_2}$$
$$h = (H - H_{c_1})/H_{c_2}$$
$$b = B/H_{c_2}$$
$$h_0 = H_0/H_{c_2}$$
$$h_1 = H_{c_1}/H_{c_2}$$
$$h_2 = (H_{c_2} - H_{c_1})/H_{c_2}$$
$$\xi = x/d$$
$$f(b) = F(B)$$
$$q = \gamma d$$

where d is the half-thickness of the sample, the critical state equation (6.1) becomes:

$$\left|\frac{\partial h}{\partial \xi}\right| = q f^{-1}(b)(1 - b) \qquad (6.1a)$$

and the relation (6.4) between B and H:

$$b(\xi) = h(\xi) + \frac{h_1}{h_2^{\beta}} h^{\beta}(\xi) \quad . \tag{6.2}$$

Now we can calculate the local induction as a function of the distance from the sample surface (where $\xi = 1$). In increasing field we obtain:

$$b^{+}(\xi) = 1 - q^{-1} f(b) \partial h/\partial \xi \tag{6.3a}$$

and in decreasing field:

$$b^{-}(\xi) = 1 + q^{-1} f(b) \partial h/\partial \xi \quad . \tag{6.3b}$$

The parameter q can be obtained from the magnetization curve using equations (6.1a) and (6.2) and equations (28a) and (28b) of ref. 1:

$$4\pi M_{rev}(H_a) = \tfrac{1}{2}(4\pi M^{+} + 4\pi M^{-}) \tag{6.4a}$$

$$-\left(\frac{\partial B^{+}}{\partial \xi}\right)_{H_a} = (4\pi M^{+} - 4\pi M^{-}) \quad . \tag{6.4b}$$

Higher order terms are neglected, which is justified if the external field is sufficiently high, i.e. well above H_a^{*} where the central core with B = 0 disappears [3].

The average flux density $\overline{B}$ in the sample at each moment of the alternating field period can be obtained with the help of expressions (6.3a) and (6.3b), following the same general principles as in chapter 5, Substituting $\overline{B}$ in (5.3a) and (5.3b) we can compute μ' and μ''. Two different cases must be distinguished again. If the variations in the field pattern do not reach the mid-plane of the sample (left-hand part of fig. 6.1) we obtain:

$$\pi h_0 \mu' = -\frac{1}{q}\int_0^{\pi} d\omega t \{ \int_{h(\xi_{T/2})}^{h(\xi_t)} fdh - \int_{h(\xi_t)}^{h_a + h_0 \cos\omega t} fdh \} \cos\omega t$$

$$+ \frac{1}{q}\int_{\pi}^{2\pi} d\omega t \{ \int_{h(\xi_{T/2})}^{h(\xi_t)} fdh - \int_{h(\xi_t)}^{h_a + h_0 \cos\omega t} fdh \} \cos\omega t \quad . \tag{6.5a}$$

$$\pi h_0\mu'' = -\frac{1}{q}\int_0^{\pi} d\omega t\{\int_{h(\xi_{T/2})}^{h(\xi_t)} fdh - \int_{h(\xi_t)}^{h_a+h_0\cos\omega t} fdh\}\sin\omega t$$

$$+\frac{1}{q}\int_{\pi}^{2\pi} d\omega t\{\int_{h(\xi_{T/2})}^{h(\xi_t)} fdh - \int_{h(\xi_t)}^{h_a+h_0\cos\omega t} fdh\}\sin\omega t \quad . \qquad (6.5b)$$

In the variations in the field pattern do reach the mid-plane (right-hand part of fig. 6.1):

$$\pi h_0\mu' = -\frac{1}{q}\int_0^{\omega t_A} d\omega t\{\int_{h_{mA}}^{h(\xi_t)} fdh - \int_{h(\xi_t)}^{h_a+h_0\cos\omega t} fdh\}\cos\omega t$$

$$+\frac{1}{q}\int_{\omega t_A}^{\pi} d\omega t\{\int_{h_{mt}}^{h_a+h_0\cos\omega t} fdh\}\cos\omega t$$

$$+\frac{1}{q}\int_{\pi}^{\omega t_B} d\omega t\{\int_{h_{mB}}^{h(\xi_t)} fdh - \int_{h(\xi_t)}^{h_a+h_0\cos\omega t} fdh\}\cos\omega t$$

$$-\frac{1}{q}\int_{\omega t_B}^{2\pi} d\omega t\{\int_{h_{mt}}^{h_a+h_0\cos\omega t} fdh\}\cos\omega t \quad . \qquad (6.6a)$$

$$\pi h_0\mu'' = -\frac{1}{q}\int_0^{\omega t_A} d\omega t\{\int_{h_{mA}}^{h(\xi_t)} fdh - \int_{h(\xi_t)}^{h_a+h_0\cos\omega t} fdh\}\sin\omega t$$

$$+\frac{1}{q}\int_{\omega t_A}^{\pi} d\omega t\{\int_{h_{mt}}^{h_a+h_0\cos\omega t} fdh\}\sin\omega t$$

$$+\frac{1}{q}\int_{\pi}^{\omega t_B} d\omega t\{\int_{h_{mB}}^{h(\xi_t)} fdh - \int_{h(\xi_t)}^{h_a+h_0\cos\omega t} fdh\}\sin\omega t$$

$$-\frac{1}{q}\int_{\omega t_B}^{2\pi} d\omega t\{\int_{h_{mt}}^{h_a+h_0\cos\omega t} fdh\}\sin\omega t \quad . \qquad (6.6b)$$

The definitions of ξ_t, $\xi_{T/2}$, $h(\xi_t)$, $h(\xi_{T/2})$, t_A, t_B, h_{mA}, h_{mB} and h_{mt} follow from fig. 6.1, which is somewhat similar to fig. 5.6. These quantities can be determined with the help of (6.1a); for instance ξ_t for $0 \leq t \leq t_A$ follows from:

$$q(1 - \xi_t) = \int_{h(\xi_t)}^{h_a+h_0} \frac{f\,dh}{1 - b(h)}$$

in which $h(\xi_t)$ is found from:

$$\int_{h(\xi_t)}^{h_a+h_0} \frac{f\,dh}{1 - b(h)} = \tfrac{1}{2} \int_{h_a+h_0\cos\omega t}^{h_a+h_0} \frac{f\,dh}{1 - b(h)}$$

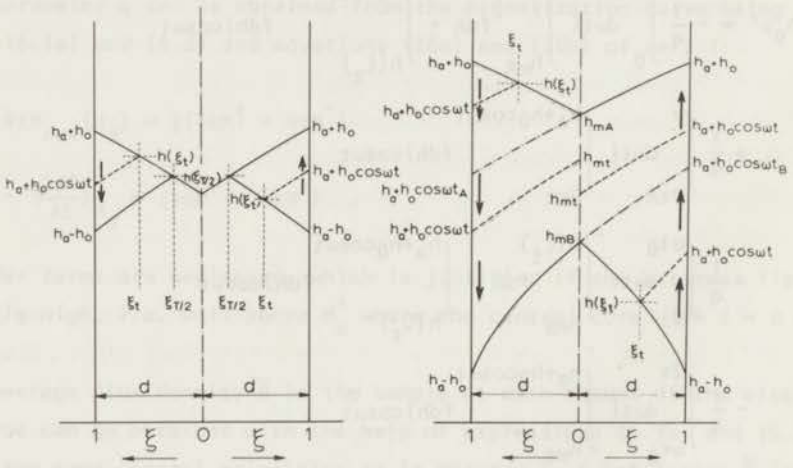

Fig. 6.1 *Definitions of the quantities occurring in the integration limits of equations (6.7a), (6.7b), (6.8a) and (6.8b). The left-hand figure is the case that the variations in the flux density pattern, due to the variations in the external field, do not reach the mid-plane of the sample; the right-hand figure is the case that the variations reach the mid-plane. The left half of each figure refers to decreasing field, the right half to increasing field.*

After the proper choice for f all the computations may be carried out, making use of the value of q derived from the static magnetization curve, see above. In this way we can obtain μ' and μ'' as functions of H_a and H_0 for any critical state model.

We made calculations based on four different critical state models. The model of Labusch [4], originally derived for the case of pinning by a dilute system of point defects, following the interpolation method of chapter 3, section 3.4.2c, leads to:

$$P_v \sim \gamma \frac{(H_{c_2} - B)}{\sqrt{H - H_{c_1}}} \frac{B}{4\pi} \quad , \qquad f = \sqrt{h} \tag{6.7a}$$

The model of Good and Kramer [5], derived for pinning by line defects, using the same interpolation method:

$$P_v \sim \gamma \frac{H}{H - H_{c_1}} \frac{\sqrt{B}}{4\pi} \quad , \qquad f = \frac{h(1 - b)\sqrt{b}}{h + h_1} \tag{6.7b}$$

The empirical model of Goedemoed et al. [6]:

$$P_v \sim \gamma(H_{c_2} - B) \frac{B}{4\pi} \quad , \qquad f = 1 \tag{6.7c}$$

The empirical model of Campbell et al. [7]:

$$P_v \sim \gamma(H_{c_2} - B) \frac{\sqrt{B}}{4\pi} \quad , \qquad f = \sqrt{b} \tag{6.7d}$$

Our calculations were carried out with H_{c_1}, H_{c_2}, β and q adapted to the static magnetization curve at 5.5 K of our sample NO-320, the one with the strongest pinning. Fig. 6.2 shows the values of μ'/μ_A and μ''/μ_A obtained in this way for amplitudes ranging from 1 to 100 Oe at four different values of the external field (H_a = 1000, 1300, 1700 and 2000 Oe). It turns out that all four models practically coincide with the London-Bean curve of fig. 5.11. This is not too surprising, since the pinning in this sample is still relatively weak, so that, except perhaps for very low induction values, $\partial B/\partial x$ must be almost a constant throughout the sample. Obviously the curvature of the B(x) pattern becomes the less relevant the smaller the amplitude, so any critical state model should approach the London-Bean curve for H_0 approaching zero, even for low values of H_a. Hence if the experiments do not coincide with the London-Bean curve, not even for small amplitudes, it follows that the results cannot be described with any critical state model, at least not without amendments. We repeated the calculations with a fifty times higher value of q, and still the deviations from the London-Bean curve of fig. 6.2 remained very small.

If, however, the experimental data are in agreement with the London-Bean curve, this kind of diagram is not suitable to distinguish between different

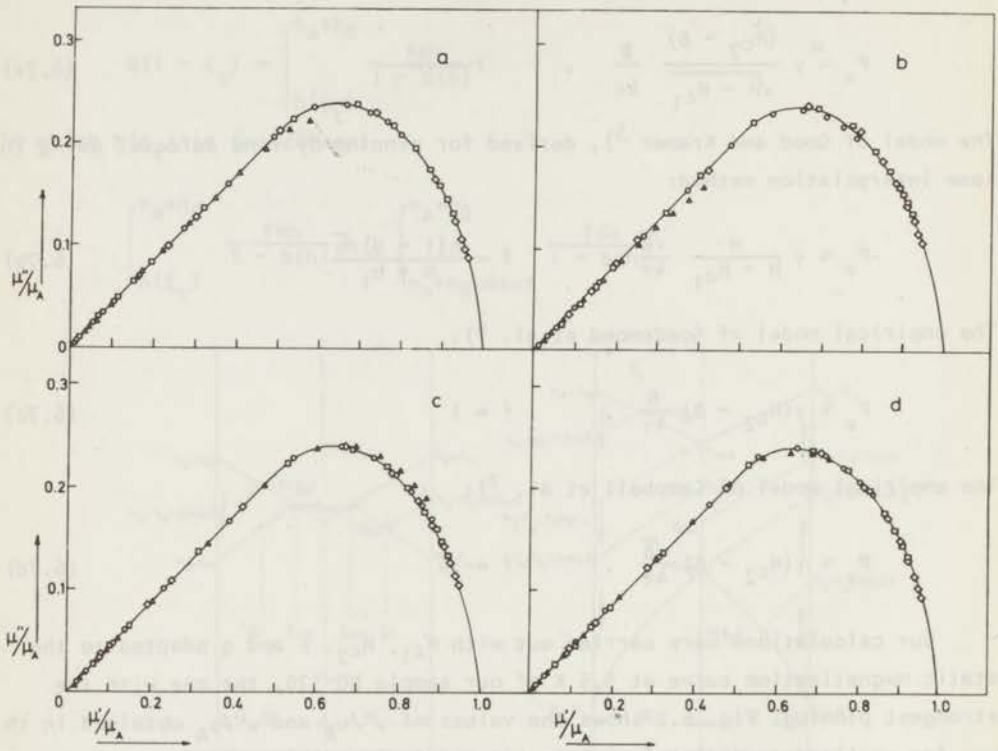

Fig. 6.2 *Plot of μ'/μ_A versus μ''/μ_A, calculated from four theoretical models for sample NO-320 at 5.5 K. a: Labusch model, b: Good and Kramer model, c: Goedemoed model, d: Campbell model.* △ *: applied field H_a = 1100 Oe,* ○ *: H_a = 1300 Oe,* □ *: H_a = 1700 Oe,* ◇ *H_a = 2000 Oe.*

critical state models. This can better be derived from the separate plots of μ' and μ'' versus H_a or H_0, shown in figs. 6.3 and 6.4 for NO-320. The dotted lines are the different theoretical predictions, the drawn curves represent the experimental results, which will be discussed in section 6.5. The adaptations of q to the static magnetization curve were made at 1700 Oe, so here the four curves of fig. 6.3 intersect and those of fig. 6.4 coincide. Figs. 6.5 and

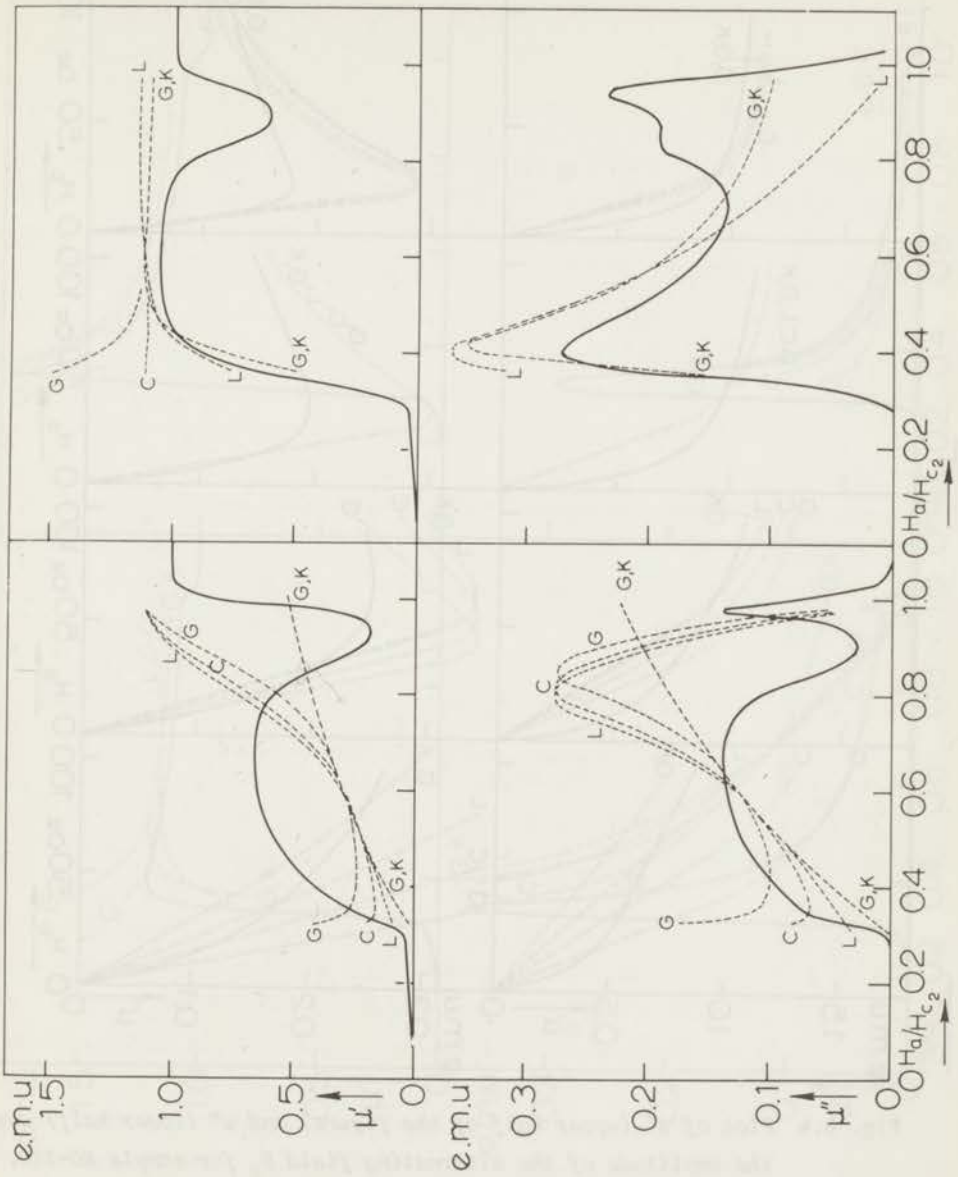

Fig. 6.3 *Plot of μ' (upper half of the figure) and μ'' (lower half) versus the applied stationary field H_a (divided by H_{c_2}) for sample NO-320. Fully drawn curves: experimental results; dotted lines: theoretical models. L: Labusch model; G,K: Good and Kramer model; G: Goedemoed model; C: Campbell model. Left: amplitude at the ac field: H_0 = 10.1 Oe; right: H_0 = 75.3 Oe.*

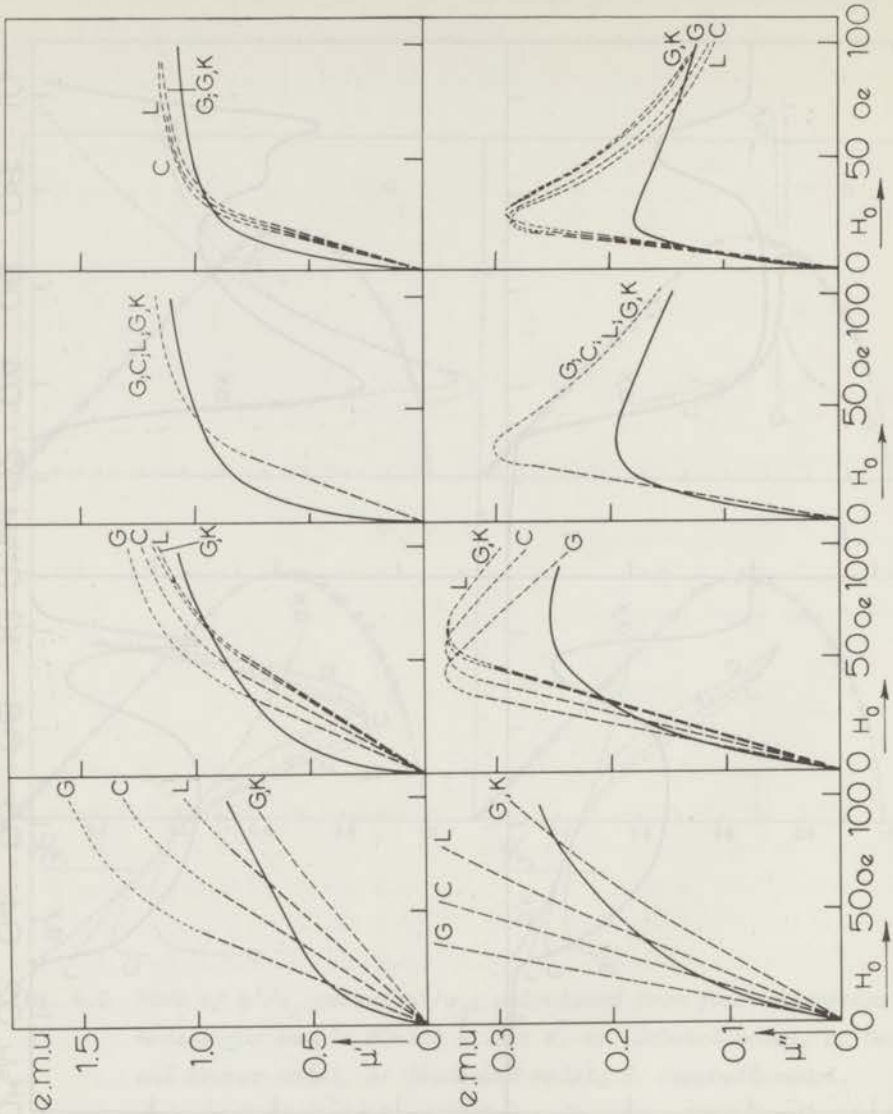

Fig. 6.4 *Plot of μ' (upper half of the figure) and μ'' (lower half) versus the amplitude of the alternating field H_0 for sample NO-320. Fully drawn curves: experimental results; dotted lines: theoretical models; dashed parts: amplitudes for which the variations in the induction pattern do not reach the mid-plane of the sample. L: Labusch model; G,K: Good and Kramer; G: Goedemoed model; C: Campbell model. From left to right: applied stationary field H_a = 1000, 1300, 1700 and 2000 Oe.*

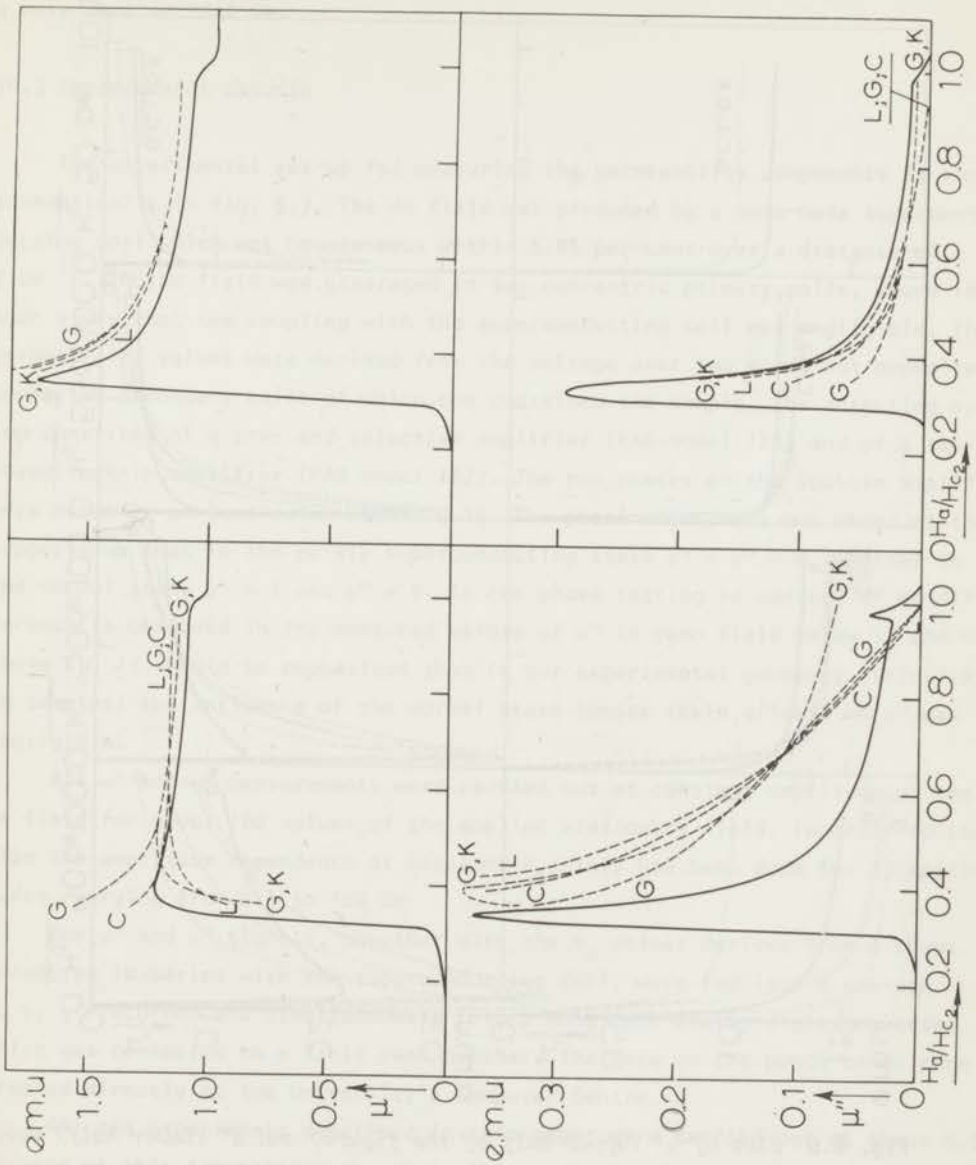

Fig. 6.5 *Plot of μ' (upper half of the figure) and μ" (lower half) versus the applied stationary field H_a (divided by H_{c_2}) for sample NO-0. Fully drawn curves: experimental results; dotted lines: theoretical models. L: Labusch model; G,K: Good and Kramer model; G: Goedemoed model; C: Campbell model. Left: amplitude of the ac field: H_0 = 10.1 Oe; right: H_0 = 75.3 Oe.*

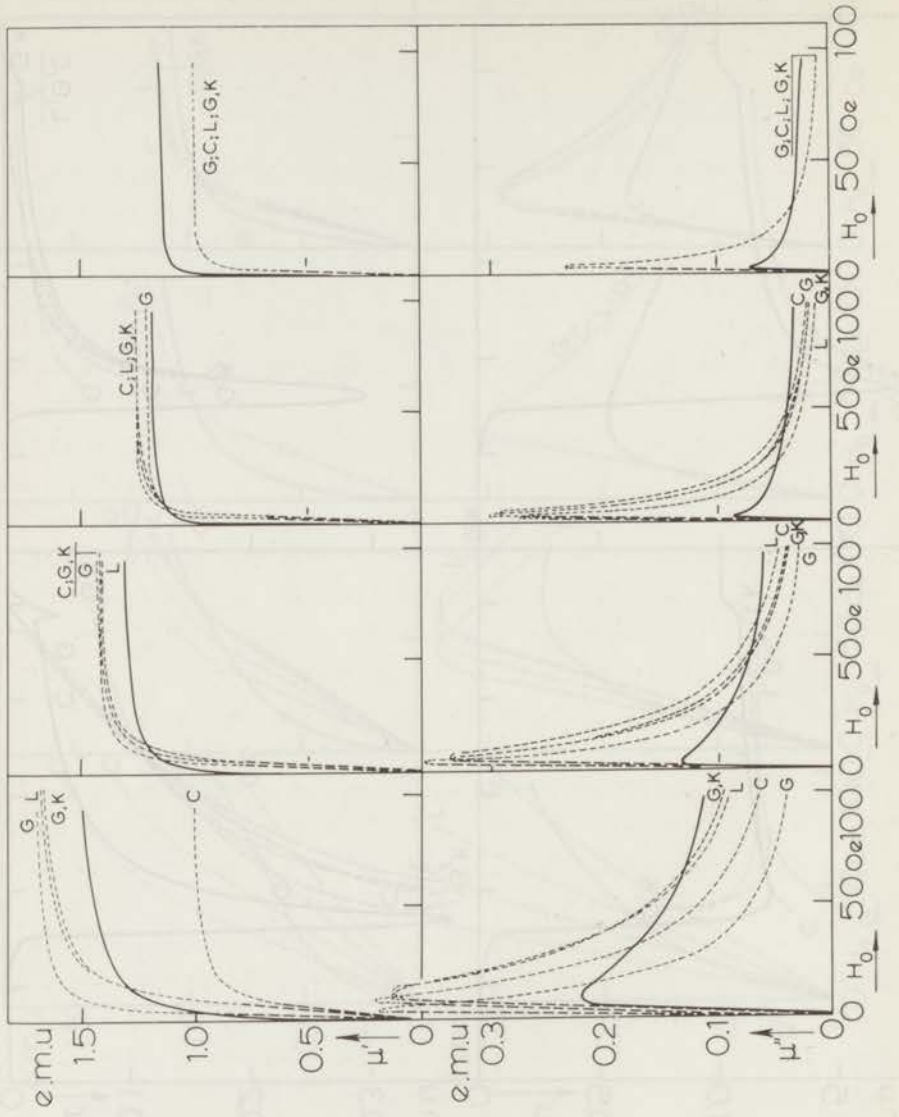

Fig. 6.6 *Plot of μ' (upper half of the figure) and μ'' (lower half) versus the amplitude of the alternating field H_0 for sample NO-0. Fully drawn curves: experimental results; dotted lines: theoretical models; dashed parts: amplitudes for which the variations in the induction pattern do not reach the mid-plane of the sample. L: Labusch model; G,K: Good and Kramer model; G: Goedemoed model; C: Campbell model. From left to right: applied stationary field H_a = 1000, 1300, 1700 and 2000 Oe.*

6.6 give the corresponding results for sample NO-0. Here the adaptations of q were made at 2000 Oe.

§6.3 *Experimental details*

The experimental set-up for measuring the permeability components is shown schematically in fig. 6.7. The dc field was produced by a home-made superconducting coil which was homogeneous within 0.05 per cent over a distance of 7 cm [1]). The ac field was generated in two concentric primary coils, wound in such a way that the coupling with the superconducting coil was negligible. The permeability values were derived from the voltage over two equal but oppositely connected secondary coils of which one contained the sample. The detecting system consisted of a pre- and selective amplifier (PAR model 120) and of a two phase lock-in amplifier (PAR model 127). The two phases of the lock-in amplifier were mutually perpendicular within 0.1%. The phase adjustment was based on the supposition that in the purely superconducting state $\mu' = \mu'' = 0$, whereas in the normal state $\mu' = 1$ and $\mu'' = 0$. So the phase setting is correct if no difference is observed in the measured values of μ'' in zero field below T_c and well above T_c. It should be emphasized that in our experimental geometry (thin flat Nb samples) the influence of the normal state losses (skin effect) on μ'' was negligible.

All μ' and μ'' measurements were carried out at constant amplitude of the ac field for about 100 values of the applied stationary field. In order to study also the amplitude dependence at constant H_a, this has been done for 23 amplitudes, varying from 0.1 to 100 Oe.

The μ' and μ'' signals, together with the H_a values derived from a shunt connected in series with the superconducting coil, were fed into a two-pen x, y, y'-recorder and simultaneously into a home-made analog-digit converter which was connected to a Facit band puncher. The data on the punch bands were treated directly at the University's Computer Centre.

All the experiments described in this paper were carried out at about 5.5 K, because at this temperature the reversible magnetization curves of our samples could still be described very well with the model of Kes et al. [1]). Since no frequency dependence was observed (see section 6.1) the experiments were usually carried out at 114 Hz. The temperature of the sample was measured with a ground-off Allen-Bradley carbon thermometer, glued to the sample with General Electric varnish. The calibration procedure has been described earlier [8]). (See also chapter 3, section 3.3.) The temperature of the samples was stabilized within

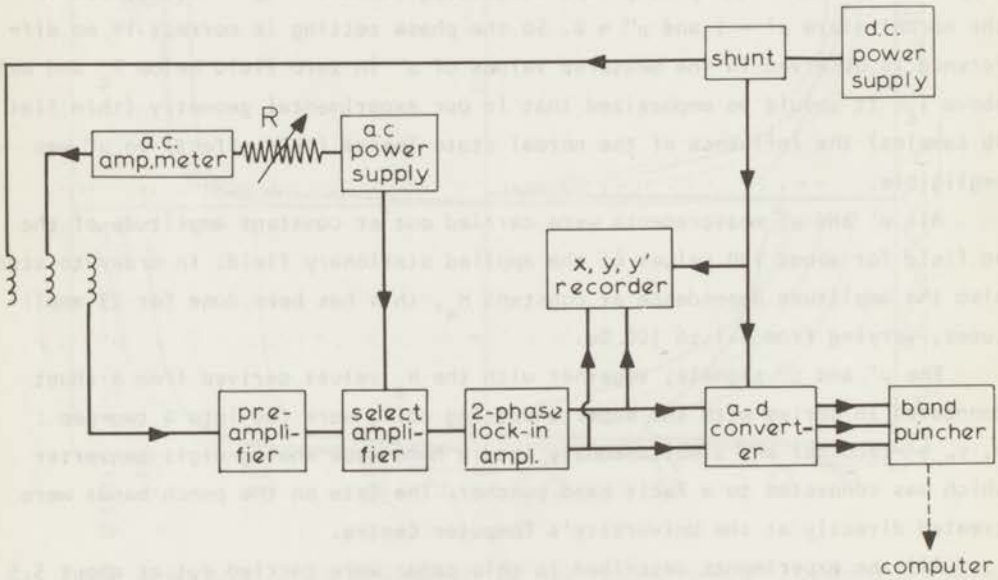

Fig. 6.7 *Block diagram of the measuring equipment.*

10 mK with the help of a home-made lock-in amplifier.

§6.4 *The experimental results*

In fig. 6.8 we plotted μ' and μ'' versus H/H_{c_2} for samples N-0 (left) and NO-0 (right). The influence of the surface barrier is obvious. For N-0 an ac field with small amplitude ($\sim$ 1.0 Oe) is screened off almost completely by this barrier up to H_{c_2} (μ' and μ'' being both small in this field region), whereas between H_{c_2} and H_{c_3} it gradually penetrates through the surface layer [9]). For NO-0, on the other hand, the ac field penetrates immediately at H_{c_1} and no screening is observed any more above H_{c_2}, where $\mu' = 1$ and $\mu'' = 0$. For high amplitudes (above 50 Oe) the surface layer, both above and below H_{c_2}, is penetrated also for N-0. For both samples the whole variation of μ' takes now place between H_{c_1} and H_{c_2} and μ'' (so the energy dissipation) shows a maximum in this region. Obviously for N-0 the ac losses are mainly due to irreversibility in the surface layer, for NO-0 they are caused by bulk pinning. The susceptibility curves for N-0 at an amplitude of 10 Oe have a somewhat intermediate character, ac losses being observed both above and below H_{c_2}.

For NO-0 the μ' curves at the higher amplitudes are very similar to the derivative of the reversible Abrikosov curve. The μ'' curves, so also the energy losses, are low except near H_{c_1}. This is in qualitative agreement with the measured magnetization curve, which is almost reversible over the whole field region, except near H_{c_1} (see chapter 3).

In the left-hand sides of figs. 6.9, 6.10, 6.11 and 6.12 we give the permeability data (again at 5.5 K) of N-0 samples after neutron irradiation at different doses (N-317 to N-320). At the right these figures show the results of the same samples after surface oxidation. The general picture is the same as for fig. 6.8, but especially the μ' curves become the lower the higher the dose. For all our samples the ratio H_{c_3}/H_{c_2} is very well in agreement with the theoretical value 1.7 [9]).

Fig. 6.13 shows the results for all our samples at one value of the amplitude of the ac field: 5 Oe. Apart from some anomalies near H_{c_2}, discussed below, the differences are not too big, only for NO-320 the curve is much lower than for the other samples. Also μ'' is rather low for this sample. Pronounced differences between NO-320 and the other oxidized samples were also observed in the peak effect (see chapter 4) and in the magnetization curves (see chapter 3). Probably all these differences are correlated with the fast increase of the sizes of the clusters of point defects ("raft formation") upon neutron

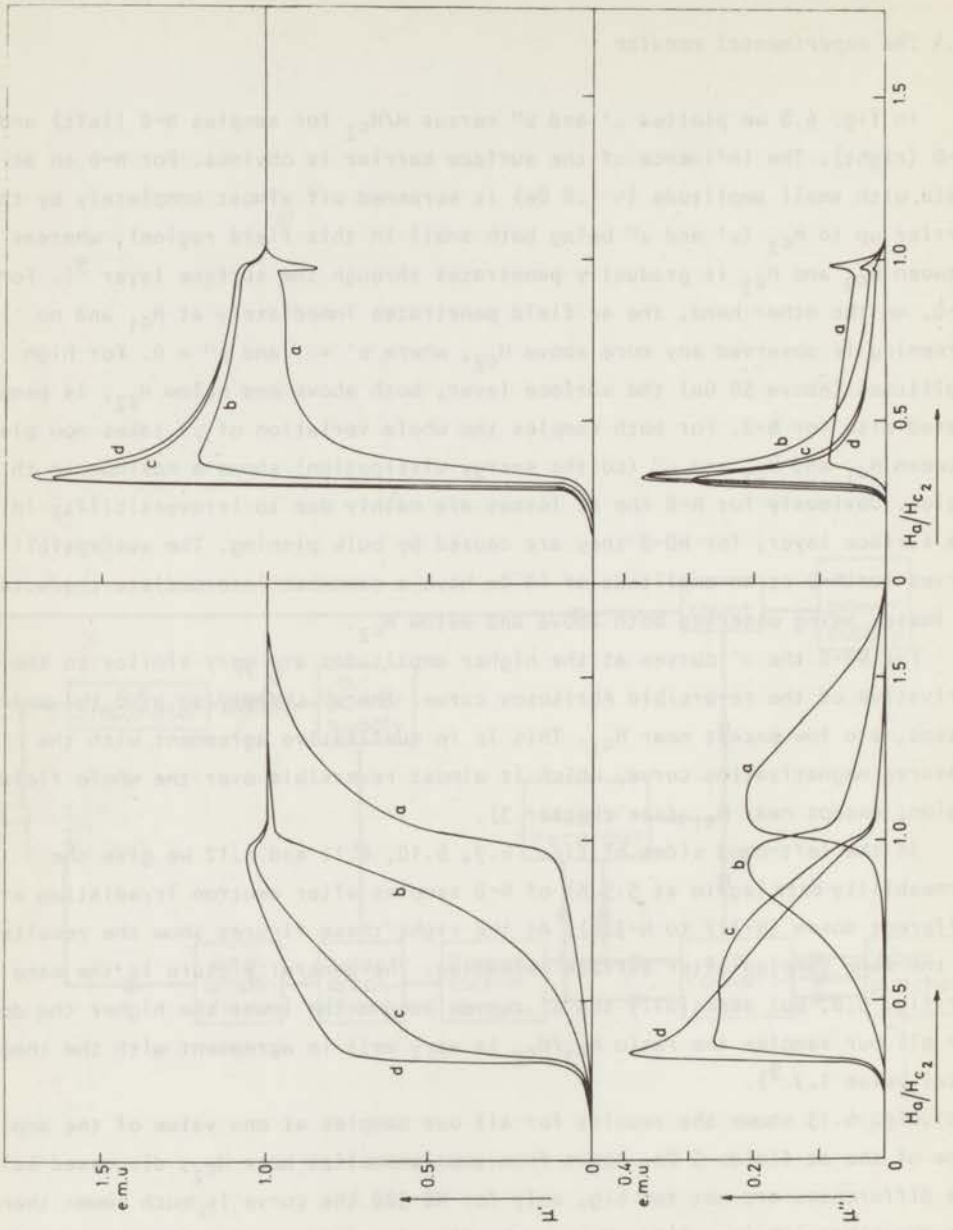

Fig. 6.8 *Plot of μ' (upper half of the figure) and μ'' (lower half) versus the applied stationary field H_a, divided by H_{c_2}; experimental results. Left: sample N-0; right: sample NO-0. a: amplitude H_0 = 1.01 Oe, b: H_0 = 10.1 Oe, c: H_0 = 50.2 Oe, d: H_0 = 75.3 Oe.*

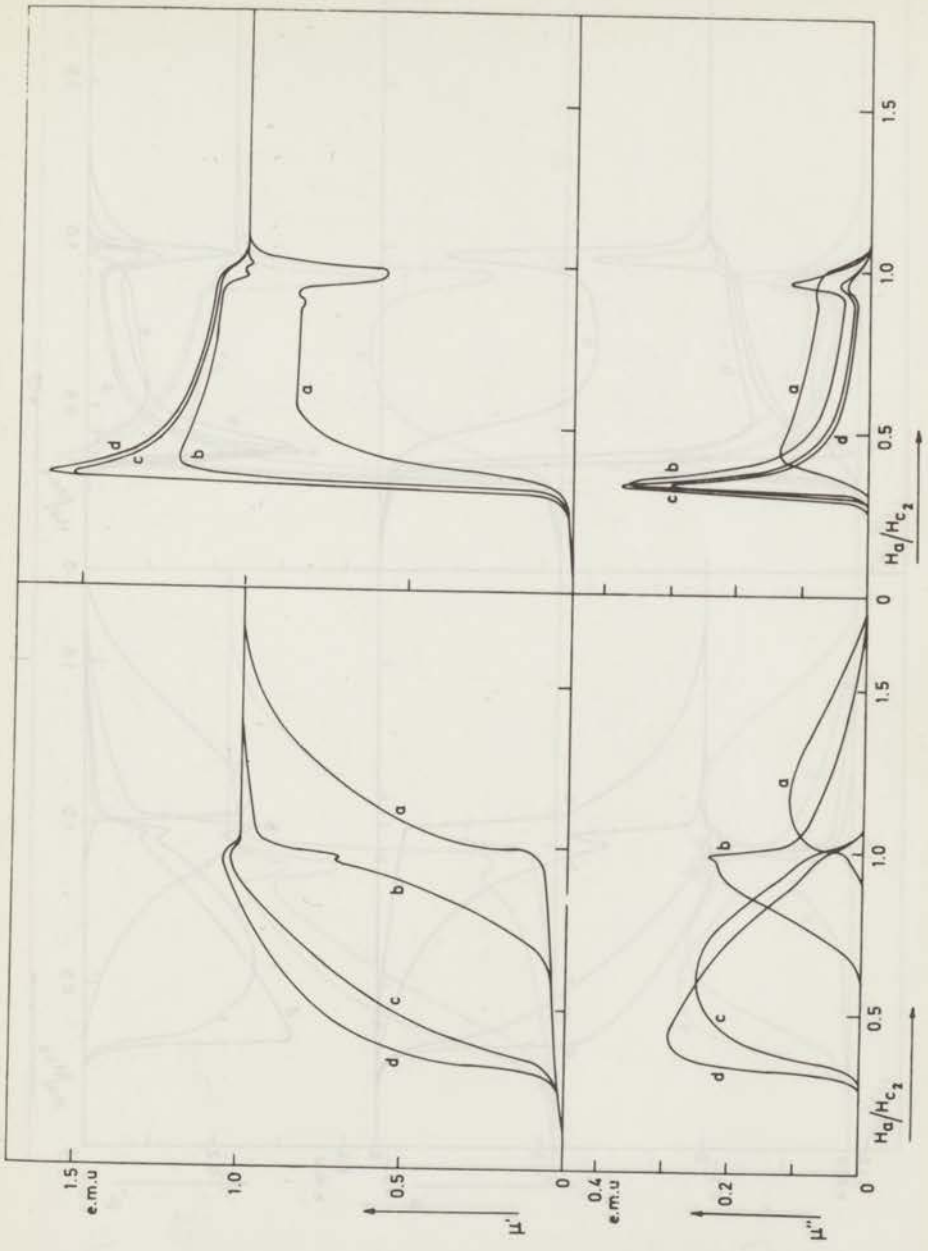

Fig. 6.9 *Plot of μ' (upper half of the figure) and μ'' (lower half) versus the applied stationary field H_a, divided by H_{c_2}; experimental results. Left: sample N-317; right: sample NO-317. a: amplitude H_0 = 1.01 Oe, b: H_0 = 10.1 Oe, c: H_0 = 50.2 Oe, d: H_0 = 75.3 Oe.*

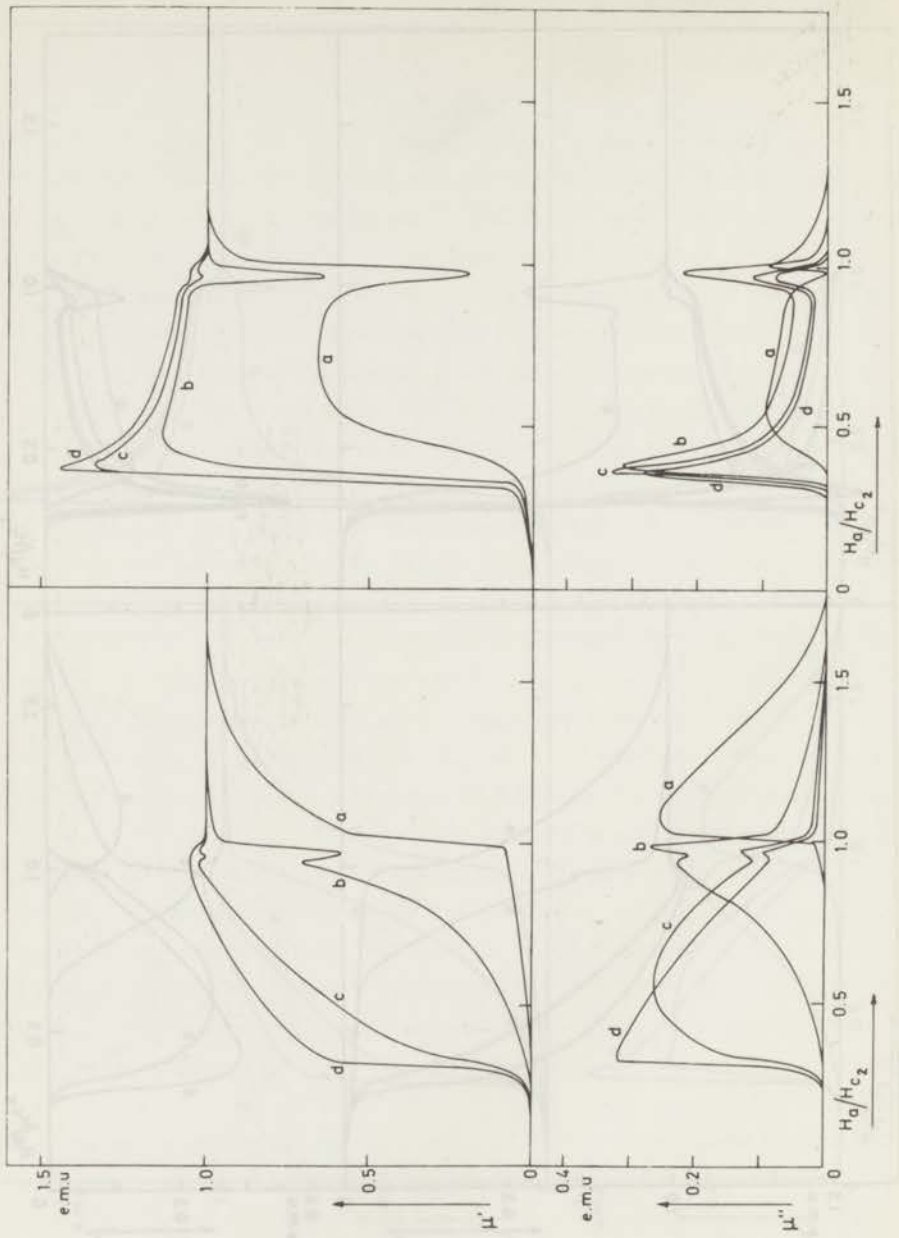

Fig. 6.10 *Plot of μ' (upper half of the figure) and μ" (lower half) versus the applied stationary field H_a, divided by H_{c_2}; experimental results. Left: sample N-318; right: sample NO-318. a: amplitude H_0 = 1.01 Oe, b: H_0 = 10.1 Oe, c : H_0 = 50.2 Oe, d: H_0 = 75.3 Oe.*

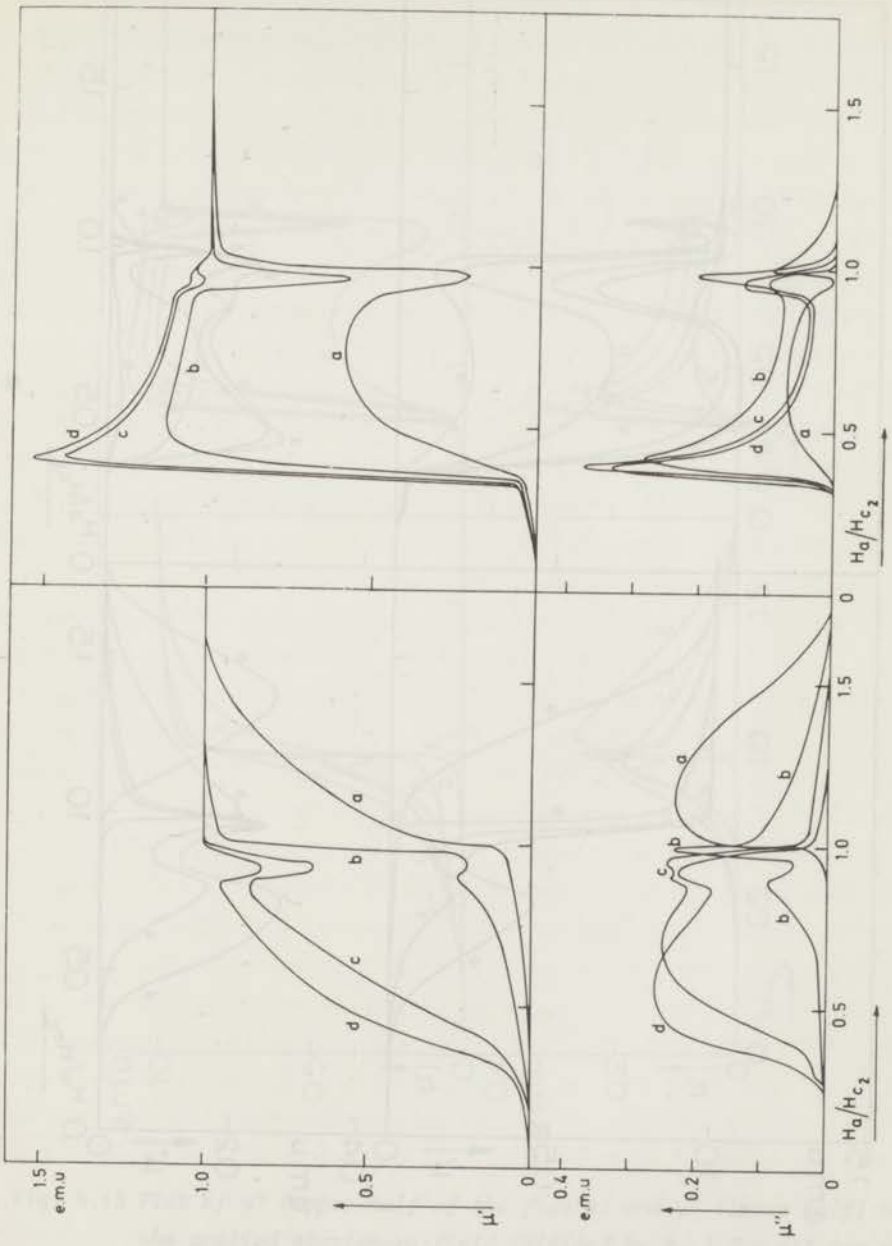

Fig. 6.11 *Plot of μ' (upper half of the figure) and μ'' (lower half) versus the applied stationary field H_a, divided by H_{c2}; experimental results. Left: sample N-319; right: sample NO-319. a: amplitude H_0 = 1.01 Oe, b: H_0 = 10.1 Oe, c: H_0 = 50.2 Oe, d: H_0 = 75.3 Oe.*

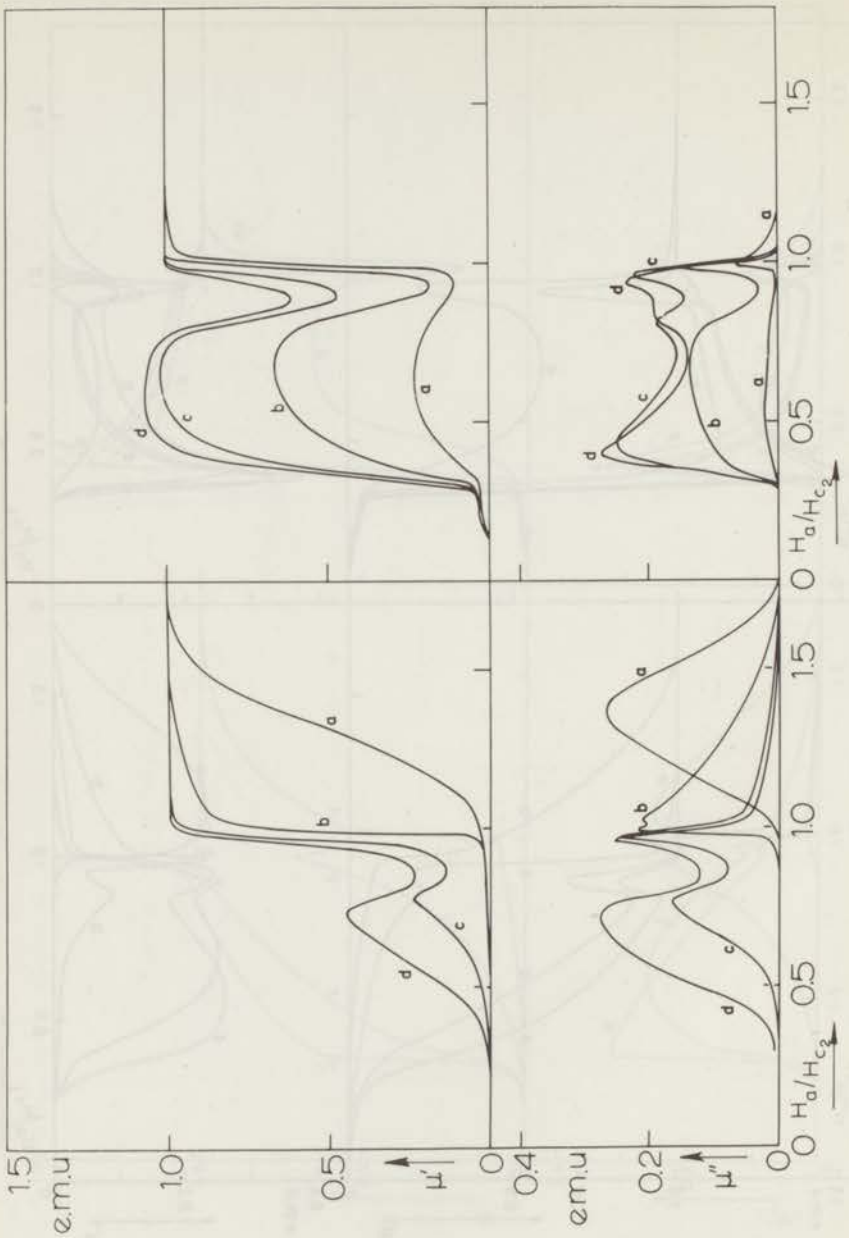

Fig. 6.12 *Plot of μ' (upper half of the figure) and μ" (lower half) versus the applied stationary field H_a, divided by H_{c_2}; experimental results. Left: sample N-320; right: sample NO-320. a: amplitude H_0 = 1.01 Oe, b: H_0 = 10.1 Oe, c: H_0 = 50.2 Oe, d: H_0 = 75.3 Oe.*

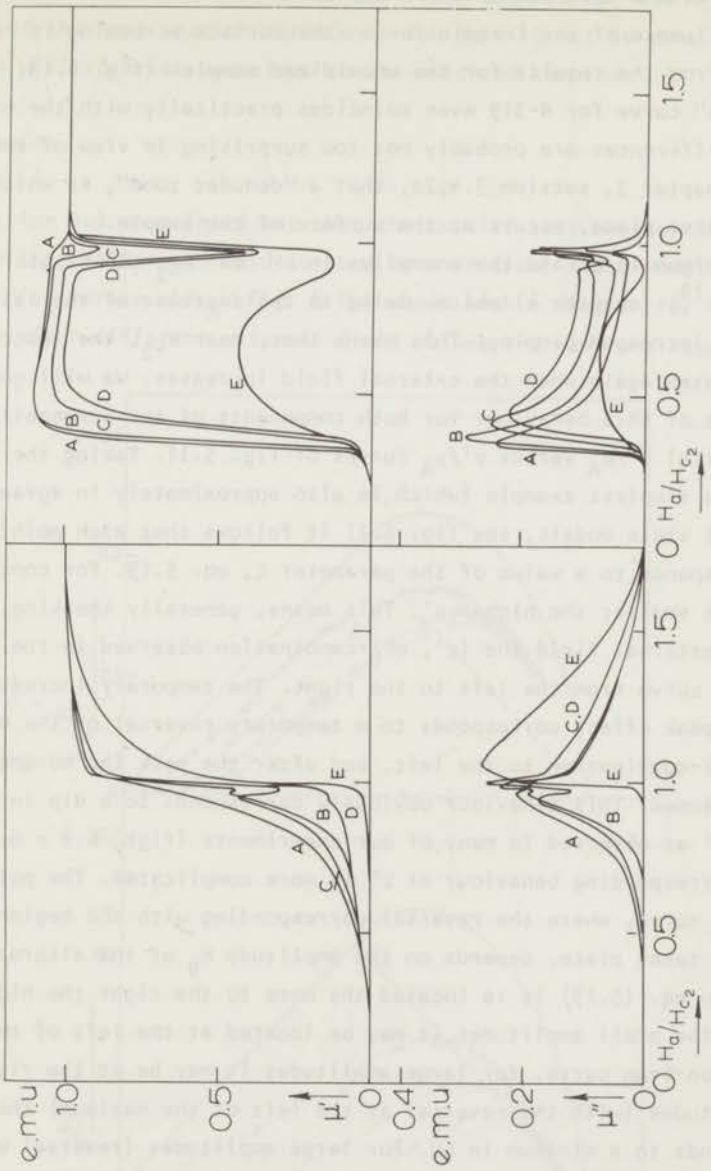

Fig. 6.13 *Plot of μ' (upper half of the figure) and μ" (lower half) versus the applied stationary field (divided by H_{c_2}) for all our samples; experimental results. Amplitude of the alternating field: H_0 = 5 Oe. Left half of the figure: curve A: sample N-0; B: N-317; C: N-318; D: N-319; E: N-320. Right half of the figure: curve A: sample NO-0, B: NO-317; C: NO-318; D: NO-319; E: NO-320.*

irradiation with a dose above 10^{20} n·cm^{-2}.

The influence of the irradiation on the surface screening is rather small, as follows from the results for the unoxidized samples (fig. 6.13, left-hand side). The μ'' curve for N-319 even coincides practically with the one for N-318. The small differences are probably not too surprising in view of the fact, discussed in chapter 3, section 3.4.2a, that a "denuded zone", in which no cluster formation takes place, occurs at the surface of the sample.

The minimum in μ' and the anomalies in μ'' near H_{c_2} can be ascribed to the peak effect [10]) (chapter 4) which, owing to the decrease of the lattice rigidity, leads to an increased pinning. This means that, near H_{c_2}, the induction gradient $\partial B/\partial x$ increases again when the external field increases. We will consider the consequences of this behaviour for both components of the permeability, using the theoretical μ''/μ_A versus μ'/μ_A curves of fig. 5.11. Taking the London-Bean curve as the simplest example (which is also approximately in agreement with our critical state models, see fig. 6.2) it follows that each point of this curve corresponds to a value of the parameter ζ, eq. 5.19. For constant H_0, $\partial B/\partial x$ is the smaller the higher μ'. This means, generally speaking, that for increasing external field the (μ', μ'')-combination observed in the experiment follows the curve from the left to the right. The temporary increase of $\partial B/\partial x$ due to the peak effect corresponds to a temporary reversal of the movement of the (μ', μ'')-combination to the left, and after the peak the movement to the right is resumed. This behaviour obviously corresponds to a dip in the measured values of μ' as observed in many of our experiments (figs. 6.8 - 6.12).

The corresponding behaviour of μ'' is more complicated. The point on the London-Bean curve, where the reversal corresponding with the beginning of the peak effect takes place, depends on the amplitude H_0 of the alternating field. According to eq. (5.19) it is located the more to the right the higher H_0. This means that for small amplitudes it may be located at the left of the maximum of the London-Bean curve, for large amplitudes it may be at the right. So for small amplitudes (with the reversal at the left of the maximum) the minimum in μ' corresponds to a minimum in μ''. For large amplitudes (reversal well at the right of the maximum) it corresponds to a maximum in μ''. For intermediate amplitudes the situation may occur that the reversal takes place just somewhat to the right of the maximum and then the $\mu''(H_a)$ curve may show a minimum between two maxima. In conclusion, there are three possibilities for the behaviour of μ'' at the peak effect and all three have been observed, at least qualitatively, in our experiments, see figs. 6.9 - 6.12.

In chapters 2 and 5 a satisfactory explanation was reached for the

permeability behaviour due to the surface layer between H_{c_2} and H_{c_3}. In the discussion of the next section surface screening will not be considered any more and we will restrict ourselves to the oxidized samples.

§6.5 *Discussion*

In section 6.2 we pointed out that the crucial test whether the experimental permeability values can be described by a critical state model or not is a plot of μ''/μ_A versus μ'/μ_A. Fig. 6.14a shows such a diagram for sample NO-320 at 5.5 K for four different external field values and many amplitudes, varying

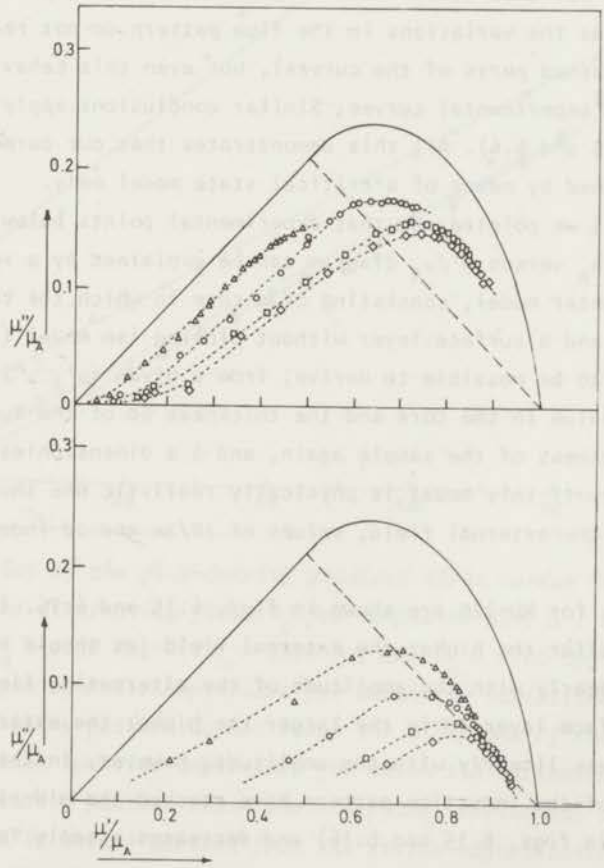

Fig. 6.14 *Plot of* μ''/μ_A *versus* μ'/μ_A *as a function of the amplitude of the alternating field. Experimental data for sample NO-320 (upper half) and NO-0 (lower half).* △ *: applied field* H_a *= 1100 Oe,* ○ H_a *= 1300 Oe,* □ H_a *= 1700 Oe,* ◇ H_a *= 2000 Oe.*

from 0.5 to 100 Oe. The full line is the London-Bean curve of fig. 6.2 with which our four critical state models of section 6.2 practically coincide. It follows that the experimental data do not coincide with this curve, and that it is not even approached for small amplitudes (which are at the left side of the diagram). The data for sample NO-0 (fig. 6.14b) show even larger deviations.

In figures 6.3 and 6.4 we plotted μ' and μ'' for NO-320 as obtained from our four critical state models, both versus the external field H_a (divided by H_{c_2}) and versus the amplitude H_0 of the alternating field. In both figures the fully drawn curves show the experimental results and they demonstrate again that there is no agreement, neither for μ', nor for μ''. It follows from fig. 6.4 that for all our theoretical models both μ' and μ'' are practically linear with H_0 as long as the variations in the flux pattern do not reach the mid-plane of the sample (dashed parts of the curves), but even this behaviour is not sustained by the experimental curves. Similar conclusions apply for sample NO-0 (figures 6.5 and 6.6). All this demonstrates that our permeability results cannot be explained by means of a critical state model only.

In chapter 5 we pointed out that experimental points below the London-Bean curve of the μ''/μ_A versus μ'/μ_A diagram can be explained by a somewhat artificial two-parameter model, consisting of a core in which the London-Bean model is valid, and a surface layer without pinning (so model (4) of section 6.2). It proved to be possible to derive, from a given (μ', μ'')-combination, both the $\partial B/\partial x$-value in the core and the thickness δd of the surface layer (d the half-thickness of the sample again, and δ a dimensionless parameter between 0 and 1). If this model is physically realistic one should expect, for given values of the external field, values of $\partial B/\partial x$ and δd independent of the amplitude.

The results for NO-320 are shown in figs. 6.15 and 6.16. It turns out that $\partial B/\partial x$ is the smaller the higher the external field (as should be expected) but it increases linearly with the amplitude of the alternating field. The thickness of the surface layer δd is the larger the higher the external field. It rises more or less linearly with the amplitude, however, in the region where the variations of the induction pattern have reached the mid-plane of the sample (black symbols in figs. 6.15 and 6.16) and decreases steeply for small amplitudes [†]).

[†]) In chapter 5 we used amplitudes only up to 10 Oe and a much smaller experimental accuracy. Here the measured variations in both $\partial B/\partial x$ and δd were of the order of a factor 2, which is not contradictory to the present results.

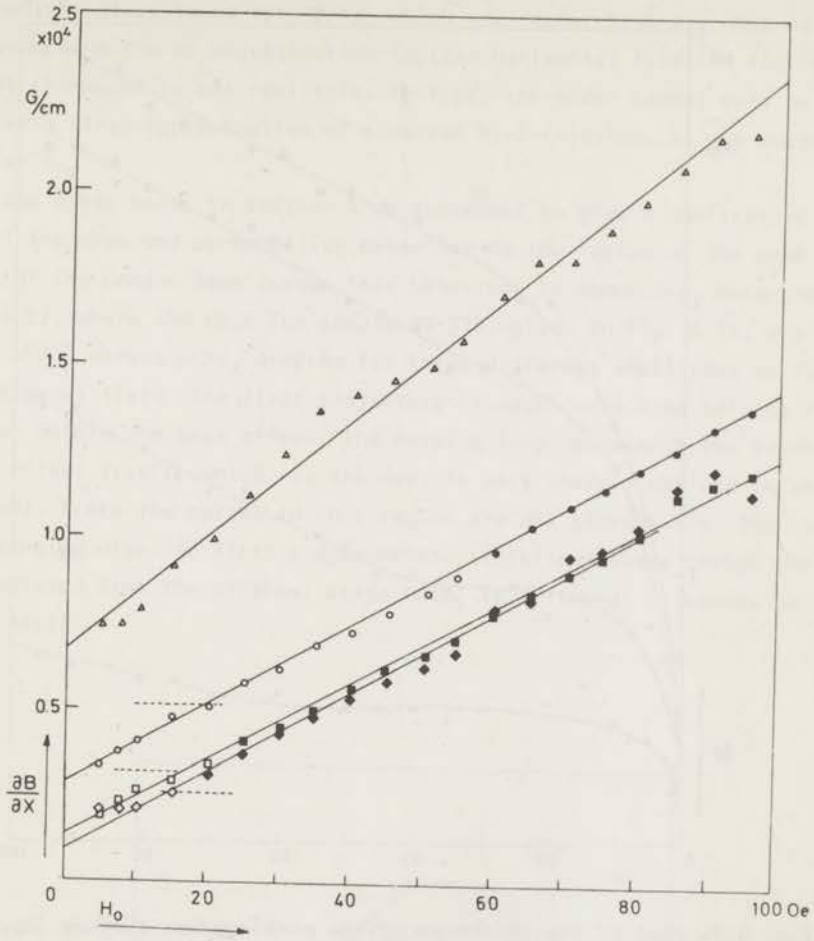

Fig. 6.15 *Plot of the flux-density gradient ∂B/∂x versus the amplitude of the alternating field H_0 for sample NO-320. △ : applied field H_a = 1100 Oe, ○ : H_a = 1300 Oe, □ : H_a = 1700 Oe, ◇ : H_a = 2000 Oe. Open symbols: amplitudes for which the variations in the flux-density pattern do not reach the mid-plane of the sample. Black symbols: amplitudes for which the variations in the flux-density pattern reach the mid-plane. Horizontal dotted lines: ∂B/∂x values derived from the static magnetization curve (the value for H_a = 1100 Oe is not given, since here eq. 6.6b cannot be applied any more).*

The steep variation of both ∂B/∂x and δd with the amplitude H_0 seems to indicate already that the model of a London-Bean core with a surface layer

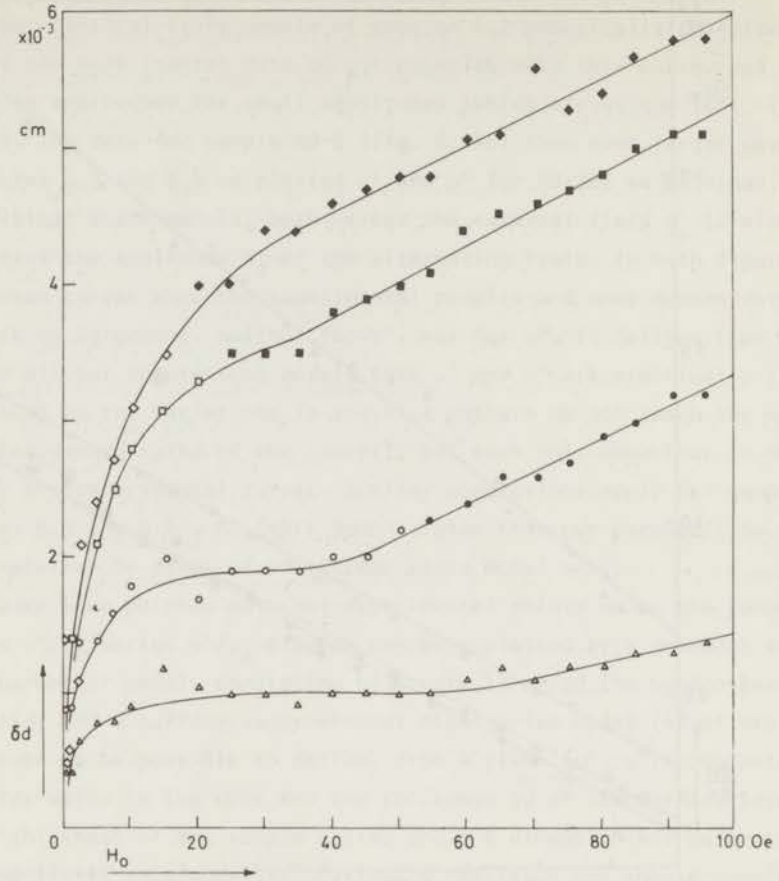

Fig. 6.16 *Plot of the thickness of the pinning-free surface layer δd versus the amplitude of the alternating field H_0 for sample NO-320. △ : applied field H_a = 1100 Oe, ○ : H_a = 1300 Oe, □ : H_a = 1700 Oe, ◇ : H_a = 2000 Oe. Open symbols: amplitudes for which the variations in the flux-density pattern do not reach the mid-plane of the sample. Black symbols: amplitudes for which the variations in the flux-density pattern reach the mid-plane.*

without any pinning as such should not be considered as realistic, but an even more convincing proof for this conclusion is the surprisingly high value of δd. The half-thickness of our sample was 109 microns, so that at H_a = 2000 Oe and H_0 = 100 Oe more than half the sample was without pinning. Even more extreme values were found for the sample NO-0 where, under these conditions, the pinning-free region proved to be almost ninety per cent of the sample. Also the

corresponding values found for $\partial B/\partial x$, which are rather high as compared to those found from the dc magnetization (dotted horizontal lines in fig. 6.15) show that the model is not realistic. In fact, the model cannot even be considered as a first approximation of a curved B(x)-relation, as was suggested in chapter 5.

On the other hand, in section 4 we succeeded to give a qualitative explanation of the observed permeability behaviour in the region of the peak effect in terms of the London-Bean curve. This behaviour is shown even more clearly in fig. 6.17, where the data for sample NO-320, given in fig. 6.12, are replotted in a μ''/μ_A versus μ'/μ_A diagram for three different amplitudes as function of the external field. The first trajectory of each curve from left to right is the region before the peak effect, the ensuing loop represents the region of the peak effect itself (which, by the way, is very sharply defined in this kind of diagram). Since the curves in this region are not closed, i.e. the loops do not coincide with the first trajectories, it follows that, though the general trend predicted from the critical state model is followed, it cannot be valid in every detail.

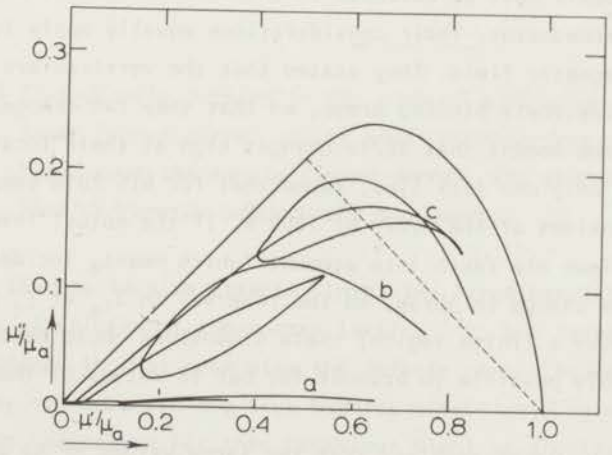

Fig. 6.17 *Plot of μ''/μ_A versus μ'/μ_A as a function of the applied field. Experimental data for sample NO-320. a: amplitude H_0 = 5 Oe; b: H_0 = 10 Oe; c: H_0 = 50 Oe.*

In view of these arguments it seems necessary, in order to give a comprehensive description of the ac and dc behaviour of type II superconductors, to consider δd and $\partial B/\partial x$ (as determined from our two-parameter model) as effective quantities which are not unambiguously determined by the applied stationary field only. If such a "quasi-critical state" actually corresponds with pinning-free regions they may arise in two different ways.

In the first place they may be directly related to the defect structure of the sample. The existence of these regions would have no consequence for the description of the dc magnetization curves in view of the adaptable pinning parameter γ (eqs. 6.7). However, from the amplitude dependence found for δd we have to realize that then the effectiveness of these pinning-free regions must depend still in some way on the actual flux distribution.

In the second place pinning-free regions may arise due to local de-pinning of the vortices by the ac field [11]). For instance, one might think of small normal regions, created by excessive local heating due to the flux motion, although this possibility is unlikely since no frequency dependence was observed. The absence of frequency dependence seems to indicate that even a reversal of the sign of $\partial H/\partial t$ in general should be sufficient to cause such a de-pinning. Gittleman and Rosenblum [12]) and also Campbell [13]) pointed out already that critical state models must be extended in the case of an alternating current through the superconductor. Their considerations equally apply to a sample in an alternating magnetic field. They stated that the vortices are more or less free to move inside their pinning areas, so that they can change their position freely once, at the moment that $\partial B/\partial x$ changes sign at their locations. Lowell [14]), considering only one flux line, found that for his PbIn sample these areas should have dimensions of the order of 1000 Å. If the mutual interactions between the flux lines are taken into account (which means, incidentally, that the discontinuous change in $\partial B/\partial x$, so the reversal in J_{c_s} at ξ_t in fig. 6.1 is smeared out over a finite region) these dimensions could become much larger, but it seems hardly possible to account for our δd values of the order of 50 microns.

In fact it should be realized that the large values of δd as found from our experiments can never be explained by considering them as the linear addition of a large number (n) of isolated small regions in which the vortices can move freely. It is obvious from fig. 6.18 that for large n this pattern approaches the London-Bean distribution again with a smaller value of $\partial B/\partial x$, and that such regions contribute the less effectively to the variations of the induction pattern the larger their distance to the surface. So in order to

attain a certain effective value of δd the sum of the diameters of the pinning-free regions should exceed this δd the more, the larger n. Therefore we do not believe that it will be possible to explain our δd values in terms of the behaviour of independent flux lines.

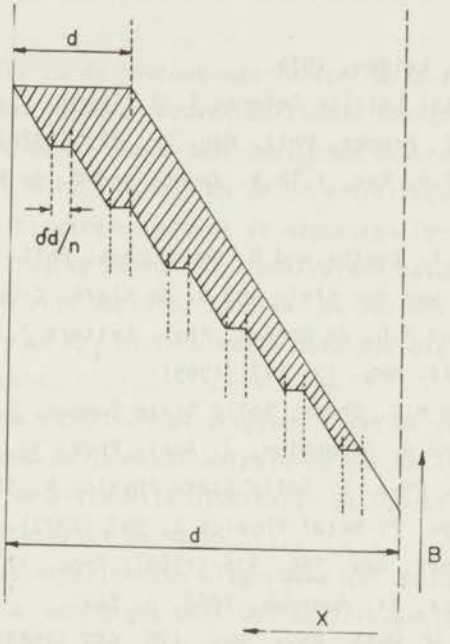

Fig. 6.18 *Flux-density pattern in the case of a pinning-free surface layer (upper curve) and of small pinning-free regions distributed over the sample (lower curve). The shaded area shows the flux difference between the two cases.*

We think that collective effects, involving large bundles of flux lines, coupled by the elasticity of the vortex lattice [15]), are responsible for the observed phenomena. In that case also the defects cannot be considered as independent. They can only pin the flux bundles effectively by collective actions [16]). An indication for this behaviour might be provided by the fact that for the sample with the lowest pinning (NO-0) δd is appreciably larger than for NO-320.

References

1. P.H. Kes, C.A.M. van der Klein and D. de Klerk, Journ. Low Temp. Phys. 10, 754 (1973).
2. J. Friedel, P.G. de Gennes and J. Matricon, Appl. Phys. Letters 2, 119 (1963).
3. P.H. Kes, thesis, Leiden, 1974.
4. R. Labusch, Crystal Lattice Defects 1, 1 (1969).
5. J.A. Good and E.J. Kramer, Phil. Mag. 22, 329 (1970).
6. S.H. Goedemoed, P.H. Kes, F.Th.A. Jacobs and D. de Klerk, Physica 35, 273 (1967).
7. A.M. Campbell, J.E. Evetts,and D. Dew-Hughes, Phil. Mag. 18, 319 (1968).
8. P.H. Kes, C.A.M. van der Klein and D. de Klerk, Cryogenics 14, 168 (1974).
9. D. Saint James and P.G. de Gennes, Phys. Letters 7, 306 (1963).
10. A.B. Pippard, Phil. Mag. 19, 217 (1969).
11. W.C.H. Joiner and M.C. Ohmer, Solid State Commun. 8, 1569 (1970).
12. J.I. Gittleman and B. Rosenblum, J. Appl. Phys. 39, 2617 (1968).
13. A.M. Campbell, J. Phys. C: Solid State Physics 4, 3186 (1971).
14. J. Lowell, J. Phys. F: Metal Physics 2, 547 (1972).
15. G.J. van Gurp, Phys. Rev. 166, 436 (1968); Proc. 11th Int. Conf. Low Temp. Physics, St. Andrews, 1968, p. 862.
16. W.A. Fietz and W.W. Webb, Phys. Rev. 178, 657 (1969).

SAMENVATTING

In dit proefschrift is de invloed van rooster defecten veroorzaakt door walsen en vervolgens door gloeien by verschillende temperaturen (tot maximaal 1600°C) en van defecten veroorzaakt door neutronen bestraling met verschillende doses (tot maximaal $1,5 \times 10^{20}$ n/cm^2) op de irreversibele eigenschappen van supergeleidend niobium beschreven. Zowel de magnetisatie-kromme in stationaire velden als de permeabiliteits kurven in wisselvelden gesuperponeerd op het stationaire magneetveld zijn bepaald. Speciaal de verschijnselen bij magneetveld waarden tussen H_{c_1} en H_{c_2} en in mindere mate ook die voor waarden tussen H_{c_2} en H_{c_3} zijn onderzocht.

Uit de magnetisatie experimenten uitgevoerd aan de gewalste preparaten kunnen we concluderen dat de onomkeerbaarheid en dus de inductiegradient toeneemt bij toenemen van de dislocatie dichtheid. De inductiegradient is evenredig met de dislocatie dichtheid tot de macht 2/3.

Uit de magnetisatie experimenten uitgevoerd aan de bestraalde preparaten kunnen we concluderen dat een groot deel van de irreversibiliteit een gevolg is van oppervlakte verankering. De oppervlakte barrière kan door het aanbrengen van een zeer dunne oxyde laag verwijderd worden. Daarna zijn nog drie effecten ten gevolge van de stralingsschade te onderscheiden:

a. een toename van de onomkeerbaarheid,

b. een maximum in de magnetisatiekromme in de buurt van H_{c_2} (piek-effect),

c. een toename van H_{c_2}.

De eerste twee effecten zijn, behalve voor het preparaat dat met de hoogste dosis bestraald is, tamelijk klein. Dit is in overeenstemming met de resultaten van de electronen microscoop-onderzoekingen, waaruit blijkt dat alleen voor het preparaat dat met de hoogste dosis bestraald is, de gemiddelde afmeting van de defecten (in dit geval zogenaamde „rafts") groter is dan de coherentielengte ξ, zodat inderdaad alleen voor dit preparaat een aanzienlijke toename van de pinkracht verwacht mag worden. De toename van H_{c_2} hangt niet samen met de toename van de verankeringskracht, maar is een gevolg van grote aantallen kleine, met de electronen microscoop niet waarneembare, puntdefecten, die tengevolge van de afname van de electronen-vrije weglengte, ook een toename van de restweerstand veroorzaken. Het piekeffect is een gevolg van het feit dat in de buurt van H_{c_2}

de glijdingsmodulus C_{66} van het fluxlijnen rooster sneller afneemt dan de locale verankeringskracht. Indien we aannemen dat de roosterdefecten zich gedragen als lijndefecten, hetgeen goed geargumenteerd kan worden, vinden we een uitstekende overeenstemming tussen theorie en experimenten. De onomkeerbare magnetisatiekromme kan in de buurt van H_{c_1} beschreven worden met de op puntdefecten gebaseerde theorie van Labusch en met de op lijndefecten gebaseerde theorie van Good en Kramer. Dit betekent dat we in dit gebied een combinatie hebben van verankering ten gevolge van puntfouten en van lijnfouten. In de buurt van H_{c_2} wordt de magnetisatiekromme het best beschreven met de theorie van Good en Kramer, hetgeen in overeenstemming is met de verklaring van het piek-effect.

Concluderend kunnen we zeggen, dat tengevolge van hun onderlinge spatiëring, de stralingsdefecten zich kunnen gedragen als puntfouten, lijnfouten of als een combinatie van beide.

Bij de experimenten met wisselvelden (bij de gewalste preparaten met amplituden tussen 0,7 en 10 Oe; bij de bestraalde preparaten tussen 0,1 en 100 Oe) zijn beide componenten van de permeabiliteit (μ' en μ'') gemeten.

Het permeabiliteitsgedrag tussen H_{c_2} en H_{c_3} laat zich uitstekend beschrijven met een hysterese model dat gebaseerd is op een oppervlakte barrière.

Het is mogelijk, uitgaande van de magnetisatie gegevens, het gedrag van μ' en μ'' tussen H_{c_1} en H_{c_2} voor de verschillende verankeringsmodellen te berekenen onder de aanname dat de supergeleider zich op elk moment in de kritische toestand bevindt. Voor de verschillende modellen vinden we dan verschillende kurven als we μ' of μ'' uitzetten tegen het uitwendig veld of tegen de amplitude van het wisselveld; μ'' uitgezet tegen μ' geeft voor alle modellen echter dezelfde kromme! De experimentele resultaten liggen daarentegen niet op deze universele kromme, zodat we moeten concluderen dat, bij aanwezigheid van een wisselveld, de supergeleider zich niet te allen tijde in de kritische toestand bevindt.

Een quantitatieve verklaring voor dit afwijkend permeabiliteitsgedrag kunnen we nog niet geven. Een mogelijkheid is dat collectieve effecten, waarbij een groot aantal fluxlijnen betrokken is, onderling gekoppeld door de elasticiteit van het fluxlijnen rooster, verantwoordelijk zijn voor het waargenomen permeabiliteitsgedrag. In dat geval moeten we ook de defecten in het kristalrooster als onderling afhankelijk beschouwen.

ZUSAMMENFASSUNG

In dieser Dissertation wird der Einfluss von Versetzungen im Kristallgitter, verursacht durch ein Walzen und anschliessend durch ein Glühen bei verschiedenen Temperaturen (bis maximal 1600°C) und von Versetzungen, verursacht durch Neutronenbestrahlung mit verschiedenen Dosen (bis maximal $1,5 \times 10^{20} n/cm^2$) auf die irreversiblen Eigenschaften von supraleitendem Niobium beschrieben.

Sowohl die Magnetisierungskurve in stationären Feldern als auch die Permeabilitätskurven in stationär Felder überlagerten Wechselstromfeldern sind bestimmt. Insbesondere die Phänomene bei Magnetfeldwerten zwischen H_{c_1} und H_{c_2} und in geringerem Masse auch die für Werte zwischen H_{c_2} und H_{c_3} sind untersucht worden.

Aus den Magnetisierungs-Experimenten, durchgeführt an den gewalzten Präparaten, können wir schliessen dass bei zunehmender Versetzungsdichte die Irreversibilität und damit der Induktionsgradient grösser wird. Der Induktionsgradient is proportional zur 2/3 Potenz der Versetzungsdichte.

Aus den Magnetisierungs-Experimenten durchgeführt an den bestrahlten Präparaten können wir schliessen dass ein grosser Teil der Irreversibilität die Folge einer Oberflächenverankerung ist.

Die Oberflächeneffekte können durch das Anbringen einer sehr dünnen Oxydschicht entfernt werden. Danach sind noch drei Effekte infolge des Strahlungsschadens zu unterscheiden:

A. eine Zunahme der Irreversibilität,

B. ein Maximum in der Magnetisierungskurve in der Nähe vom H_{c_2} („Peakeffect"),

C. eine Zunahme des H_{c_2}.

Die erste zwei Effekte sind, ausser für das Präparat das mit der höchsten Dosis bestrahlt worden ist, ziemlich klein. Dies steht im Einklang mit den Resultaten der Elektronenmikroskop-Untersuchungen aus denen hervorgeht, dass nur für das Präparat das mit der höchsten Dosis bestrahlt worden ist, die mittlere Abmessung der Versetzungen (in diesem Falle sogenannte „Rafts") grösser ist als die Kohärenzlänge, sodass tatsächlich nur für dieses Präparat eine beträchtliche Zunahme der Haftkraft erwartet werden dürfte.

Die Zunahme des H_{c_2} hängt nicht zusammen mit der Zunahme der Verankerungskraft, sondern ist die Folge einer grossen Anzahl von kleinen, mit dem Elektronenmikroskop nicht wahrnehmbaren Punktversetzungen, die wegen der Abnahme der

freien Weglänge der Elektronen auch eine Zunahme des Restwiderstandes verursachen.

Der „Peakeffect" ist eine Folge der Tatsache dass in der Nähe des H_{c_2} der Schermodul C_{66} des Flussfadengitters schneller abnimmt als die lokale Verankerungskraft.

Wenn wir annehmen dass sich die Versetzungen im Kristallgitter wie Linien-Versetzungen betragen, welches sehr wohl angenommen werden kann, finden wir eine hervorragende Übereinstimmung zwischen Theorie und Experimenten. Die irreversible Magnetisierungskurve kann in der Nähe des H_{c_1} mit der auf Punktversetzungen basierten Theorie von Labusch und mit der auf Linienversetzungen basierten Theorie von Good und Kramer beschrieben werden.
Dies bedeutet, dass wir in diesem Gebiet mit einer Kombination von Verankerung infolge Punkt- und Linienversetzungen rechnen müssen.

In der Nähe des H_{c_2} wird die Magnetisierungskurve am besten beschrieben mit der Theorie von Good und Kramer, welches mit der Erklärung des „Peakeffectes" übereinstimmt.

Hieraus können wir folgern, dass die Strahlungsversetzungen sich infolge ihrer gegenseitigen Abstanden wie Punktversetzungen, Linienversetzungen oder wie eine Kombination der beiden verhalten können.

Bei den Experimenten mit Wechselstromfeldern (bei den gewalzten Präparaten mit einer Amplitude zwischen 0,7 und 10 Oe; bei den bestrahlten Präparaten zwischen 0,1 und 100 Oe) sind beide Komponenten der Permeabilität (μ' und μ'') gemessen worden.

Das Permeabilitätsverhalten zwischen H_{c_2} und H_{c_3} lässt sich ausgezeichnet mit einem Hysterese-Modell beschreiben, das auf einer Oberflächenbarriere basiert ist. Es ist möglich, ausgehend von den Magnetisierungsdaten, das Verhalten von μ' und μ'' zwischen H_{c_1} und H_{c_2} für die verschiedenen Verankerungsmodelle zu berechnen, wenn mann annimmt dass der Supraleiter sich zu jedem Moment im kritischen Zustand befindet. Für die verschiedenen Modelle finden wir dann verschiedene Kurven, wenn wir μ' oder μ'' aufzeichnen als Funktion vom äusseren Feld order als Funktion von der Amplitude des Wechselstromfeldes; dagegen gibt μ'', aufgezeichnet als Funktion von μ', für alle Modelle die gleiche Kurve! Die experimentellen Resultate liegen hingegen nicht auf dieser universellen Kurve, sodass wir daraus schliessen müssen dass bei Anwesenheit eines Wechselstromfeldes der Supraleiter sich nicht während der ganzen Zeit im kritischen Zustand befindet.

Eine Quantitative Erklärung für dieses abweichende Permeabilitätsverhalten können wir noch nicht geben.

Eine Möglichkeit wäre, dass kollektive Effekte, an denen eine grosse Anzahl

Flussfäden beteiligt ist, untereinander verbunden durch die Elastizität des Flussfädengitters, für das wahrgenommene Permeabilitätsverhalten verantwortlich sind. In diesem Falle müssen wir auch die Versetzungen im Kristallgitter als untereinander abhängig betrachten.

STUDIEOVERZICHT

Na het behalen van het eindexamen HBS-B aan het Sint-Franciscuscollege te Rotterdam, waar mijn eerste belangstelling voor de natuurkunde tijdens de boeiende lessen van Dr. J. Schweers gewekt werd, ving ik in 1963 mijn studie aan de Rijksuniversiteit van Leiden aan. In juni 1967 legde ik het kandidaatsexamen d' (natuur- en wiskunde met bijvak scheikunde) af, waarna ik in augustus mijn eerste werkzaamheden op het Kamerlingh Onnes Laboratorium verrrichtte en wel in de werkgroep „sterke magneetvelden en supergeleiding" die onder leiding staat van Dr. D. de Klerk. Aanvankelijk assisteerde ik Dr. P.H. Kes bij zijn onderzoek naar de warmtegeleiding in supergeleidend niobium en Drs. F.Th.A. Jacobs bij het onderzoek naar de magnetische eigenschappen. Na het vertrek van Drs. Jacobs in juli 1968 nam ik zijn onderzoek over. Na het behalen van het doctoraal examen experimentele natuurkunde in april 1970, werkte ik een dag per week als gastmedewerker op het Reactor Centrum Nederland (RCN) te Petten. Daar werden de preparaten vervaardigd, de gloeiingen en neutronen bestralingen uitgevoerd en het metallurgisch karakter van de rooster defecten m.b.v. licht- en electronen microscoop bestudeerd.

Op 1 januari 1974 verliet ik het Kamerlingh Onnes Laboratorium om, in dienst van het RCN, bij het Max Planck Institut für Plasmaphysik te Garching (West Duitsland) te gaan werken.

Mijn onderwijstaak vervulde ik van september 1969 tot januari 1974 als assistent op het eerste- en tweedejaars practicum voor hoofdvakstudenten.

Het tot stand komen van dit proefschrift is mogelijk geworden dankzij de bijdragen van velen. Drs. R. Wolf en de heer G.P. van der Mey hebben mij geassisteerd bij de experimenten en het uitwerken van de meetresultaten. De direktie van het RCN en vooral de staf van de afdeling Materiaalkunde ben ik erkentelijk voor de genoten gastvrijheid en voor het verlenen van de bestralingsfaciliteiten. Bij het RCN werden de preparaten vervaardigd door de heren J.M. Jacobs en D.S. d'Hulst, de metallografische onderzoekingen werden verricht door de heren A. Mastenbroek en G. Hamburg. De samenwerking en discussies met Drs. J.D. Elen van de afdeling Materiaalkunde van het RCN, die in 1968 reeds voorstelde het effect van stralingsschade op de supergeleidende eigenschappen van niobium te onderzoeken, heb ik bijzonder op prijs gesteld.

De nauwe en plezierige samenwerking met Dr. P.H. Kes is voor mij altijd een grote stimulans geweest. De vele discussies met hem, met mijn promotor en

met Dr. H. van Beelen zijn bepalend geweest voor een groot deel van de inhoud van dit proefschrift.

Een van de belangrijkste technische handelingen bij mijn onderzoek was het zorgvuldig insmelten van de preparaten. De heren C.J. van Klink en L. van As, die ook het overige glaswerk verzorgden, hebben dat iedere keer weer met grote bereidwilligheid gedaan. Een aantal elektronische apparaten, zoals de temperatuurstabilisator, werden door de heer J. van der Zeeuw vervaardigd. De heer T.P.M. van der Burg zorgde voor het technische gedeelte van de opstelling. De dames mevr. S. Kranenburg-Ginjaar en mej. R. Beyk hebben de manuscripten van de verschillende artikelen getypt, terwijl het typewerk voor dit proefschrift verzorgd is door mevr. E. de Haas-Walraven. De heren W.F. Tegelaar, W.J. Brokaar en L. Gijsman vervaardigden de tekeningen. De samenvatting is in het duits vertaald door mevr. E. van Kessel.